

Tool Life Prediction of Cemented Carbide Tools During Milling of Compacted Graphite Iron

Berk Saatçi

2024



LUNDS
UNIVERSITET

LTH

**LUNDS TEKNISKA
HÖGSKOLA**

Supervisor: Jan-Eric Ståhl
Co Supervisor: Juan Manuel Bello Bermejo
Examiner: Christina Windmark

Author: Berk Saatçi
Lund, Sweden 2024

Avdelningen för Industriell Produktion
Lunds Tekniska Högskola
Lunds universitet
Box 118
221 00 Lund
Sverige

Division of Production and Materials Engineering
LTH, School of Engineering
Lund University
Box 118
SE-221 00 Lund
Sweden

Printed in Sweden
Media-Tryck
Lund University

Foreword

This thesis was completed as the last step of the Master's program in Production and Materials Engineering, which has for me been an incredible journey of discovery, of challenges, and of learning, and it would not have been possible without the generous support and guidance of many. I would therefore like to thank everyone who supported me in these past months, and years.

First and foremost, I would like to extend my deepest gratitude to my two supervisors. To Jan-Eric Ståhl, thank you for sharing all that knowledge that inspired me in manufacturing and metal cutting, both during this thesis, and before, and especially for having me leave every meeting with just as many new interesting questions to pursue, as I came with. To Juan Manuel Bello Bermejo, thank you for being there at every step, not only during this thesis, but since the very first day of this program, and for spending those countless hours, debating, guessing, and sometimes just joking, but especially also for your incredible help and your feedback during these last months.

I would like to thank everyone at the Production and Materials division, both for all the knowledge you provided me with throughout this Master's program, but also for all the support during this thesis, helping me out when measurements were just not working out, when the equipment didn't co-operate, and sometimes just when ideas ran out. Your support over the last years made these last few months possible in the first place.

I would also like to thank all the people at Seco Tools for supporting this research, and especially Daniel Johansson, and Sören Hägglund, for helping me with your ideas, and your knowledge. Your guidance has been invaluable for this research.

Last but certainly not least, I owe a debt of gratitude to my family. Without your unwavering support, even when we were far away from one another, this would never have been possible, and I could never thank you enough for it.

Abstract

In the field of mechanical engineering, the optimization of machining processes, such as milling, is a critical factor for industrial efficiency and product quality. To this end, accurate tool life models allow for the identification of machining parameters that minimize wear and extend tool life, leading to significant improvements in process efficiency, which can lead to lowered costs, higher product quality, and more sustainable manufacturing processes. Additionally, the use of newer materials, such as compacted graphite iron (CGI), a cast iron with superior mechanical properties, opens new possibilities for the manufacturing industry.

This thesis therefore investigates the possibility of using the Colding tool model as a tool in predicting the tool life of cemented carbide cutting tools during the milling of compacted graphite iron (CGI). The methodology involves a series of controlled milling experiments, observing tool wear over time and the application of the Colding model to predict tool life under these conditions.

The results of the study confirm that the Colding model of tool life prediction can be successfully adapted to the unique geometries found in milling, and that it can be used to predict tool life during the machining of compacted graphite iron. The findings of this research also provide valuable insights into the behaviour of cemented carbide tools in the milling of compacted graphite iron, highlighting the importance of understanding the specific cutting process, and selecting appropriate machining parameters and tool materials.

Keywords:

Milling

Tool life

Compacted Graphite Iron

Cast Iron

Cemented Carbide

Colding Tool Life Model

Machining

Table of Contents

Foreword.....	4
Abstract.....	5
Table of Contents.....	6
List of Abbreviations	9
1 Introduction.....	10
1.1 Background.....	10
1.2 Previous Research.....	11
1.3 Aim	11
2 Theoretical Framework.....	12
2.1 Cast Irons	12
2.1.1 Iron-Carbon System	12
2.1.2 Phases in Cast Iron.....	13
2.1.3 Alloying Elements.....	13
2.1.4 Graphite Morphology.....	14
2.1.5 Classification of Cast Irons	15
2.1.6 Lamellar, Compacted, and Spheroidal Graphite Iron	16
2.2 Milling.....	17
2.2.1 Types of Milling Operations	17
2.2.2 Milling Equipment	18
2.2.3 Parameters and Cutting Geometry in Milling	18
2.2.4 Up and Down Milling	18
2.3 Cutting Tool Materials.....	19
2.3.1 Cemented Carbide Tools.....	20
2.3.2 Ceramic Tools	20
2.3.3 CBN Tools / Polycrystalline Cubic Boron Nitride	20
2.4 Tool Wear and Tool Life	21
2.4.1 Flank Wear.....	21
2.4.2 Crater Wear	21
2.4.3 Tool Life	22
2.5 Machinability	22
2.6 Economic Modelling in Manufacturing.....	23
2.6.1 Tool Life in Cost Models.....	24
2.6.2 Material Removal Rate	24
2.7 Tool Life Models	24
2.7.1 Colding Tool Life Model.....	25
2.7.2 The Five Model Constants, K, H, M, N0, and L.....	25

2.7.3	Singularity.....	26
2.7.4	Use of the Colding Model in General and in Milling	26
3	Methodology.....	27
3.1	Overview of Experimental Process.....	27
3.2	Cutting Tool.....	27
3.2.1	Insert	27
3.2.2	Milling Cutter.....	28
3.2.3	Combined Milling Tool	28
3.3	Workpiece.....	29
3.4	Skin Effect Analysis and Nanoindentation Tests.....	30
3.4.1	Nanoindentation Results	31
3.5	Skin Removal.....	32
3.6	Machinability of CGI.....	33
3.7	Milling Tests	33
3.8	Microscopy for Tool Wear.....	36
3.8.1	Measurement Intervals.....	36
3.8.2	Effect of Insert Curvature during Flank Wear Measurement.....	37
3.9	Methods and Equations for the Colding model.....	37
3.9.1	Adapting the Colding Model to Milling.....	38
4	Experimental Data	41
4.1	Tool Wear Measurements	41
5	Data Analysis and Discussion.....	44
5.1	Microscopy / Wear Development	44
5.1.1	Problem 1: Establishing a measurement baseline	44
5.1.2	Problem 2: Identifying the correct area.....	44
5.1.3	Problem 3: Identifying wear	45
5.2	Evaluation of Machining Efficiency	46
5.3	Colding Model	47
5.3.1	Non-real solutions	47
5.3.2	Solution of the Colding Equation.....	48
5.3.3	Subset Models.....	49
5.4	Colding Model Evaluation.....	50
5.5	Possible Causes of Error	51
5.5.1	Changing workpiece geometry	51
5.5.2	Changing machining environment.....	51
5.5.3	Differences between passes	51
5.5.4	Milling Insert number	51

6	Conclusion	52
7	Future Research	53
8	References.....	54
	Appendix A: Nanoindentation Data.....	57
	A.1 Gray Cast Iron / Lamellar Graphite Iron (LGI).....	57
	A.2 Compacted Graphite Iron (CGI450)*	57
	A.3 Compacted Graphite Iron (CGI350/SSF).....	58
	Appendix B: Microscopy.....	59
	B.1 Images for Test 1:.....	59
	B.2 Images for Test 2.....	66
	B.3 Images for Test 3.....	72
	B.4 Images for Test 4.....	79
	B.5 Images for Test 5.....	82
	B.6 Images for Test 6.....	90
	B.7 Images for Test 7.....	94
	B.8 Images for Test 8.....	97
	Appendix C: Subset Colding Graphs	101
	C.1 Inner Subset.....	101
	C.2 Outer Subset	101

List of Abbreviations

Symbol/ Abbreviation	Designation/definition (unit)
a_e	Radial depth of cut (mm)
a_p	Axial depth of cut (mm)
n	Spindle speed (rpm)
f_z	Feed per tooth (mm)
DC_x	Maximum cutting diameter (mm)
DC	Minimum cutting diameter (mm)
DC_w	Working (Effective) cutting diameter (mm)
T	Tool life (s)
l_{pass}	Pass length (mm)
l_{arc}	Arc length (mm)
v_c	Cutting speed (m/min)
v_f	Table feed / Feed Speed (mm/min)
z	Number of effective teeth (pcs)
h_e	Equivalent chip thickness (μm)
MRR	Metal removal rate (mm^3/min)
VB	Flank wear (μm)
KT	Crater wear
CGI	Compacted Graphite Iron
LGI	Lamellar Graphite Iron
SGI	Spheroidal Graphite Iron
EV	Electric Vehicle
BCC	Body-centered cubic
CNC	Computer numerical control
RPM	Revolutions per minute
HSS	High-speed steel
CBN	Cubic boron nitride

1 Introduction

This chapter provides an introduction of the overall context of this thesis, and delineates the aim of the research.

1.1 Background

The Cambridge dictionary defines machining as “the activity of cutting or shaping metal on a machine”[1]. While with the increased prevalence of additive manufacturing, the term subtractive manufacturing has been gaining popularity in recent years as a synonym for machining [2], that better contrasts it from the additive counterpart, in terms of scale, machining remains the dominant production method for many applications. This is due to a number of properties of machining operations, such as producing higher surface quality, and being able to create more complex structures more easily, compared to additive methods. Therefore, a better understanding of, and improvements to machining operations can directly lead to more efficient, and thereby also more sustainable production processes. One example of parts whose production strongly relies on the possibilities of machining operations, are engine blocks. Requiring accurate tolerancing, excellent surface quality, and with complex form factors, their production is dependent on machining.

The cost of manufacturing internal combustion engines furthermore remains, in spite of the prevalence of greener methods of transportation relevant: While the light duty vehicle market has seen an exponential growth of new electric vehicles (EV) [3], more than 95% of commercial heavy duty vehicles globally are relying on diesel engines for propulsion [4]. And while the EV market for trucks itself has in recent years also been steadily increasing [5], with 2024 being the first time that an EV truck has won the “International Truck of the Year” award, having been awarded to the Volvo’s FH Electric [6], it is nevertheless to be expected that diesel engines will remain common in the heavy duty vehicle market in the foreseeable future.

Hence, the development of better solutions for engines has also been continuing: Gray Cast Iron, has traditionally been the material of choice for these engines, owing to its high durability, low cost, and overall good material properties. However, in recent years, manufacturers have been looking into improved material options for use in their engines, and while not being a new material Compacted Graphite Iron (CGI), a cast iron with superior mechanical properties, has only recently been finding increased use [7]. While CGI is now used in the production of approximately 500.000 diesel engines per year [8], challenges remain surrounding its use, due to its lower machinability, which owes to its particular material properties compared to other types of cast iron. As however the demand for improved efficiency, less weight and lowered production cost, remains high when it comes to diesel engines, especially with increasing demands related to emissions, and increasing competition from EV options, there is a demand for gaining a better understanding of the machining of CGI products.

As CGI behaves differently than traditional cast irons, which are generally known for their high machinability and predictable behaviour, further need arises for the development of predictive models of machining operations of CGI, and for an understanding of the economics of using various tool materials and cutting parameters to optimise its use. In machining processes, a deciding factor is often tool life, as it connects both machine, and operator time, to the often-high costs of the cutting tools itself. One such model is the Colding model of tool life. While the Colding model has been tested and verified in turning operations, and is used in the industry as a reliable model of tool life in turning, its validity in milling has only begun to be studied, with only initial studies in the field, leaving room for further research, which could open up the possibility of optimising machining in terms of environmental sustainability and economic efficiency. In this regard, the Colding model has not been tested before for milling operations in cast iron, which leads to the aim of this research.

1.2 Previous Research

With the economical importance of optimizing machining operations of Compacted Graphite Iron, research has been conducted towards improving and validating existing models that aim to predict tool life. Citing the increased prevalence of CGI over LCI in the production of engines past research has investigated the milling compacted graphite, comparing cemented carbide and ceramics tools in terms of tool life [9]. Nevertheless, previous research on tool life that utilised tool life models has mostly been focused on turning or used older models such as Taylor, with limited attention given to the possibility of using the Colding model in milling operations, studying the milling of C 45E, a medium carbon steel [10]. This leaves the possibility of applying the Colding model for milling operations of CGI, an increasingly important material, untested, which puts it into the focus of this research.

1.3 Aim

The aim of this project is to study the relationship of cutting conditions and tool life, when machining CGI with Cemented Carbide milling tools, and based on the gathered empirical data form a Colding equation for each of the tool-workpiece combinations. This will be based on empirical data based on milling operations.

This thesis research is also designed as a first step of a larger research comparing the performance of different tool materials when cutting cast irons with different grades including CGI content and microstructure and researching the possibility of using Colding models for those.

In this context, the questions this thesis aims to answer are:

- Q1: To what extent is the Colding Model applicable in milling operations?
- Q2: What are the factors affecting outcomes when milling CGI?
- Q3: How do cemented carbide inserts behave when milling CGI?

2 Theoretical Framework

This section describes the theory behind this research. This includes aspects of material science and metallurgy concerning the workpiece materials, metal cutting processes and associated equations, and finally models of predicting tool life together with their use in industrial economy.

2.1 Cast Irons

Cast irons are a class of iron-carbon ferrous alloys, generally characterised and differentiated from steels by their higher carbon content, higher than 2%, and a silicon content of 1%-4% [11]. Together with other alloying elements, and process control during solidification, cast iron can be given a broad variety of properties, making it a versatile material [12]. While cast irons are usually of lower strength compared to steels, their lower melting point makes their production cheaper, and together with their excellent fluidity in liquid form [12], lends itself to their better formability, which makes them the material of choice in many applications.

2.1.1 Iron-Carbon System

The amount of carbon in a ferrous alloy, and its structure and distribution within it, both have a large impact on the properties of the alloy. The Iron-Carbon system, a section of which ranging up to 5% carbon by weight, hence covering both steels and cast irons is shown in the phase diagram in Figure 1 below. While the stable forms of carbon within an iron-carbon alloy are as graphite, and as carbon dissolved within the iron matrix of ferrite, several other meta-stable phases exist. While some of these occur during normal cooling processes, most commonly cementite, and pearlite which itself is a compound of alternating layers of cementite and ferrite, some are created through controlled cooling or quenching processes, or stabilized through heat treatments, or additions of other alloys, including martensite and austenite [11].

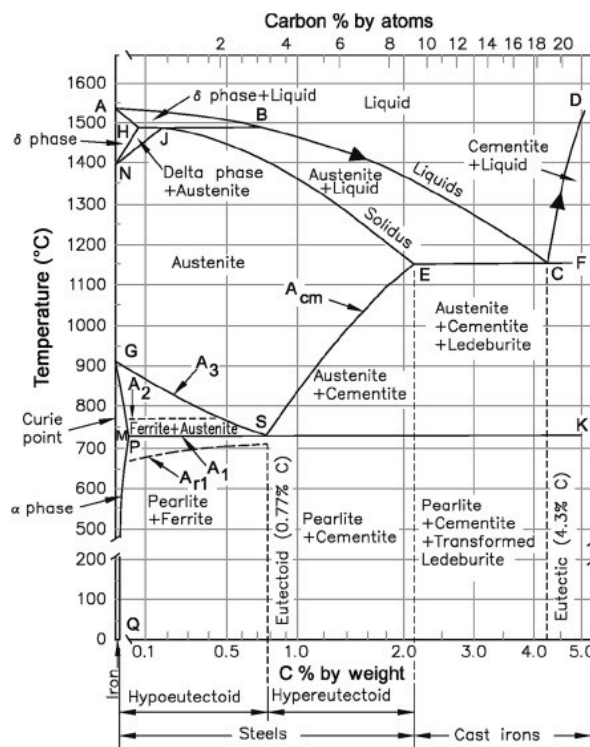


Fig 1. Iron-Carbon Phase diagram [13].

Due to their high carbon content, which cannot be dissolved in a singular iron-carbon phase, cast irons are by their nature heterogeneous alloys [11]. Due to the many meta-stable phases which can occur in the iron-carbon system, the cooling rate of cast irons during solidification has a significant impact on the resulting microstructures and their distribution, and the cooling process itself can lead to different properties at the skin and core of the material [14]. Cast irons are also therefore separated into their five main groups, based on the form and distribution of this excess carbon within them; namely white iron, malleable iron, gray iron, compacted graphite iron, and ductile iron [11], which will be discussed later in this section.

2.1.2 Phases in Cast Iron

2.1.2.1 Graphite

Graphite is the stable allotrope of carbon at normal conditions. As carbon is the main alloying element in cast iron, graphite is almost universally present in cast irons, and influences both the mechanical properties and appearance of the material, which gives cast irons their recognizable dark colour, with one exception being white cast iron, in which carbon is bound in other forms [11].

Graphite is made up of stacked layers of carbon atoms, arranged in a repeating hexagonal pattern. As the attraction forces between these layers is weak, the layers can slide over each other. These layered sheets can act as lubricant in alloys, which is both relevant in some use cases, but also affects the machinability of such alloys as it can also act as a lubricant in those processes [11]. Due to their low hardness, the shape of graphite structures affects the mechanical properties of the surrounding iron matrix, which is why importance has been given to what is called graphite morphology.

2.1.2.2 Ferrite, Cementite, and Pearlite

Ferrite, or alpha iron (α -Fe), is a relatively soft, ductile, and magnetic phase of iron. As its body-centered cubic (BCC) crystal structure is unable to dissolve larger amounts of carbon, most of it forms other structures within ferrous alloys. While graphite is the stable form of carbon, usually during solidification, most carbon is unable to form graphite, and instead is fully bound in carbides, forming a metastable structure of Fe_3C [15]. As cementite is 6.67wt% Carbon, in ferrous alloys with less carbon than that, cementite is usually found together with ferrite, which together can form a special layered structure called pearlite, named after its appearance, as shown in Figure 2 below. Pearlite is also an important element in CGI, as it increases both hardness and tensile strength [16].

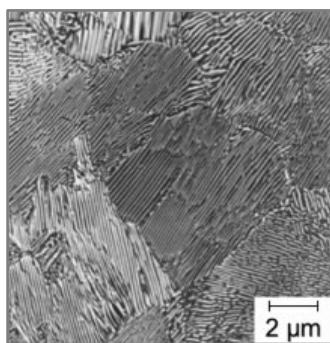


Fig 2. Pearlite structure in a steel [15].

2.1.3 Alloying Elements

2.1.3.1 Silicon

Alongside carbon, in cast irons, silicon (Si) plays a second important role, mostly due to its effect on the phases formed by the carbon. Silicon replaces the dissolved carbon in ferrite phases, causing it to form iron carbide instead, and thereby stabilizing cementite phases. This occurs by lowering the solubility of carbon in austenite, which during cooling transforms into ferrite, silicon acts as a strong

graphitizer or graphite stabilizer in cast irons, and promotes ferrite formation [11]. Silicon hence moves the eutectic composition to a lower carbon content, which lowers the melting point, easing casting.

2.1.3.2 Magnesium, Sulphur, and Manganese

Magnesium is another important element in cast irons, as its presence has a large impact on the graphite morphology. Small amounts of magnesium can cause graphite to form spheroidal graphite such as in ductile iron, or compacted graphite, such as in compacted graphite iron (CGI) [9].

In the production of ferrous alloys, sulphur is often found unintentionally due to its presence in fuels, and raw materials, in addition to sometimes intentionally being added. The role of sulphur depends on the type of iron alloy being produced, as for instance, in the production of ductile iron, a very low sulphur content is essential due to sulphur reacting with magnesium, reducing its availability for spheroidization, while conversely, in the manufacture of grey cast irons, a higher sulphur content aids in graphite nucleation [11].

Because to the strong effect of sulphur on ferrous alloys, manganese is often used as a regulator due to the interactions between sulphur and manganese: While in the absence of manganese, sulphur forms iron sulphide (FeS), when sufficient manganese is present, manganese sulphide (MnS) is formed instead. Whereas iron sulphide diffuses into grain boundaries, and intercellular areas, manganese sulphide is uniformly distributed, due to the complete solid solubility of iron and manganese [11].

As sulphur inhibits the formation of the desired vermicular graphite structures, in the production of compacted graphite iron, magnesium (Mg) is added due to it being a strong sulphide former. A side effect of this is that the formation of magnesium sulphide (MgS) being preferential over manganese sulphide (MnS), inhibits the formation of manganese sulphide in CGI, which can lead to lower machinability: During the machining of grey cast iron, manganese sulphide (MnS) has been found to play a role in forming a protective layer on the cutting edge, which has been associated with increased tool life, an effect which has not been observed in the machining of CGI, which has been attributed to the lowered tool life [17].

2.1.3.3 Pearlite stabilizers

Another important class of alloying elements in cast irons are pearlite stabilizers. This includes copper, which is the most commonly used one, in addition to other options, such as tin, nickel, manganese, and antimony. Their selection often depends on balancing their other effects on the structure and material properties, and while many of them can act as pearlite stabilizers, they can be unwanted due to other reasons, for example antimony [18].

2.1.4 Graphite Morphology

As the physical shape and structure of graphite phases has a major effect on the material properties of cast irons, methods of classification and identification have been made for a standardised system of categorization, with the ASTM A247 standard, which establishes a test method to differentiate between seven main structure types [19]. These seven types are shown in Figure 3 below.



Fig 3. Different graphite morphologies according to ASTM A 247 [18]

These seven types of which type I, type IV, and type VII, will be discussed in more detail below are:

- | | | | |
|------|-------------------------------|------|-------------------|
| I. | Spheroidal graphite | V. | Crab graphite |
| II. | Imperfect spheroidal graphite | VI. | Exploded graphite |
| III. | Temper graphite | VII. | Flake graphite |
| IV. | Compacted graphite | | |

2.1.4.1 Type I: Spheroidal Graphite

Spheroidal graphite, commonly found in ductile iron, features graphite particles in a spherical form, a structure that provides high strength and ductility. This morphology is achieved through the addition of magnesium or cerium, which causes the carbon to solidify in a nodular shape rather than the flaky or compacted forms seen in other types. In ductile iron, this shape minimizes the stress concentration points within the iron matrix, which is key its unique properties [18].

2.1.4.2 Type IV: Compacted Graphite

Compacted graphite, also known as vermicular, and characteristic of Compacted Graphite Iron, these more rounded particles significantly improve the toughness and ductility of the cast iron, and occur in the presence of low magnesium [11]. This morphology is highly desirable for applications requiring a good balance of strength and ductility. As it also has higher thermal conductivity than ductile iron, this morphology makes CGI suited for applications such as engine parts [18].

2.1.4.3 Type VII: Flake Graphite

Also known as lamellar graphite, this morphology is found in gray cast irons, and consists of graphite particles in a flake-like shape. While the flake-like shape of the graphite creates points of weakness in the cast iron, leading to reduced tensile strength and ductility compared to spheroidal or compacted graphite irons, it also leads to better machinability due to better chipping behaviour. Additionally, the presence of flake graphite provides excellent damping properties and thermal conductivity [18].

2.1.5 Classification of Cast Irons

Cast irons are some of the oldest and most commonly used metallic materials, both due to their easier machining, but also due to their castability, and versatility [11]. Due to the nomenclature having arisen through time and use, terms surrounding types of cast iron are often overlapping, and some definitions might vary, additionally, because their alloying element ranges can overlap cast irons cannot be defined by them, in comparison to steels [11]. While different terms and abbreviations exist, such as according to EN1560, which uses the Swedish term for cast iron “gjutjärn” in its abbreviations [20], in this research, nomenclature based on graphite morphology is used.

As the morphology of graphite structures has significant effects on the physical properties of cast irons, it is also used to classify cast irons into three main groups: Lamellar graphite iron (LGI), compacted graphite iron (CGI), and spheroidal graphite iron (SGI) [21], with their structure defining their general properties, as shown in Table 1 below. It should be noted that white, and malleable cast iron are separate categories not part of these three types which differ based on graphite morphology.

Table 1. Classification of LGI, CGI, and SGI.

	Lamellar Graphite Iron (Grey Cast Iron)	Compacted Graphite Iron	Spheroidal Graphite Iron
Abbreviation based on graphite structure	LGI (GCI)	CGI	SGI
EN1560 abbreviation	EN-GJL	EN-GJV	EN-GJS
Graphite Morphology 3D	Lamellas	Coral-like structure	Spheroidal
Graphite Morphology 2D	Type VII: Flake	Type IV: Compacted	Spheroidal

2.1.6 Lamellar, Compacted, and Spheroidal Graphite Iron

LGI, CGI, and SGI, while similar chemically, vary substantially in their physical properties, which can mostly be attributed to their microstructures, as can be seen in Figure 4 and Figure 5 below. While their properties align with their aforementioned morphologies, they will be summarised here.

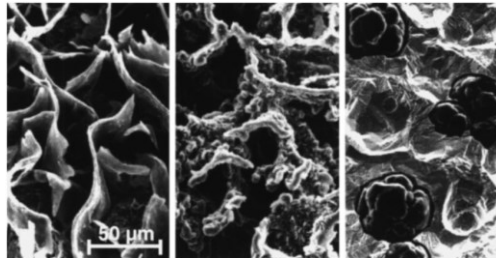


Fig 4. 3D Cast iron graphite morphology after etching (Left to right: LGI, CGI, SGI) [17].

The graphite structure of LGI in form of randomly oriented flakes with sharp edges, while allowing the induction of cracks, also improves the chipping behaviour of LGI, making it easier to machine. The more rounded of ends of the compacted structure of graphite in CGI, which is often also called vermicular, or worm-like reduces these effects CGI, both inhibiting crack growth, and due to the irregular surface causing a stronger adhesion between the graphite and iron phases [22], in turn making machining considerably more difficult while in turn improving strength and ductility. Previous studies [23] found that when milled, CGI produced longer chips than gray cast iron, which was attributed to the vermicular structure of graphite in CGI, inhibited the crack forming characteristic of the flake graphite in gray cast iron. The resulting longer contact between chip and tool was hypothesised to result in higher temperatures in the contact zone, and therefore cause the increased wear which was found in the tools used to machine CGI, compared to the ones used with gray cast iron [23]. SGI, with its spheroidal graphite, has in turn the highest ductility of the three [18].

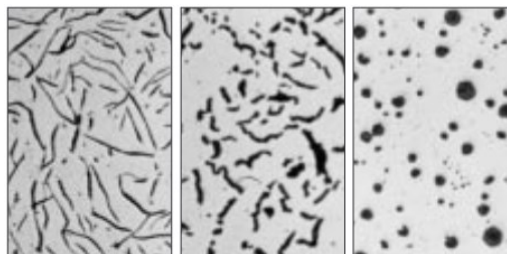


Fig 5. 2D Cast iron graphite morphology after etching (Left to right: LGI, CGI, SGI) [16].

The use of CGI, in addition to its worse machinability is made difficult due to its production: As CGI is an intermediate between LGI, and SGI, with compacted graphite requiring a fine balance between nodular and flake graphite, precise process control is important in the production process. This is exacerbated by the significant effect of small changes in alloying composition affecting the resultant graphite morphology [21], which is partly due to the narrow range in which CGI forms [16], [21].

In fact, CGI was initially developed as a side product of SGI or ductile iron development, as SGI being about twice as strong as CGI and with a five times larger stable production range made it the option of choice [16]. While initially disregarded due to the difficulties surrounding its machining, CGI has been finding increasing use in diesel engines of trucks, due to its favourable properties of high strength and stiffness [8]. Another factor making the use of CGI more difficult is that due to recycling, current CGI often contains traces of alloying metals used in the past, for example while in the past, Titanium (Ti) was added to CGI to extent this range, this is now avoided due to the detrimental effects on machinability [16].

2.2 Milling

Milling is a versatile cutting operation which compared to turning, where a rotating workpiece is machined by a stationary tool, utilises a rotating cutter working on a generally stationary workpiece. While this results in the cutting operation being intermittent and causes varying chip thickness [24], it also allows for the creation of a wide variety of features.

2.2.1 Types of Milling Operations

As the term milling covers a broad spectrum of processes, the exact details of millings operations vary based on the desired feature, with some types shown below in Figure 6, which are described here [25]:

- **Face milling** uses a cutter with cutting edges on the periphery and face to remove material primarily from the surface of the workpiece to produce a flat surface.
- **Slot milling** involves the creation of slots or grooves in the workpiece, with the cutter moving along the workpiece to cut the desired slot width and depth.
- **Shoulder milling** is used to produce a vertical surface on the periphery of the workpiece adjacent and requires cutters with side cutting edges.
- **Plunge milling** removes material by plunging the cutter in the workpiece, similar to drilling.
- **Ramp milling** involves moving the cutter into the workpiece at an angle or along a slope.
- **Ball end milling** uses a cutter with a hemispherical end to produce contoured surfaces.

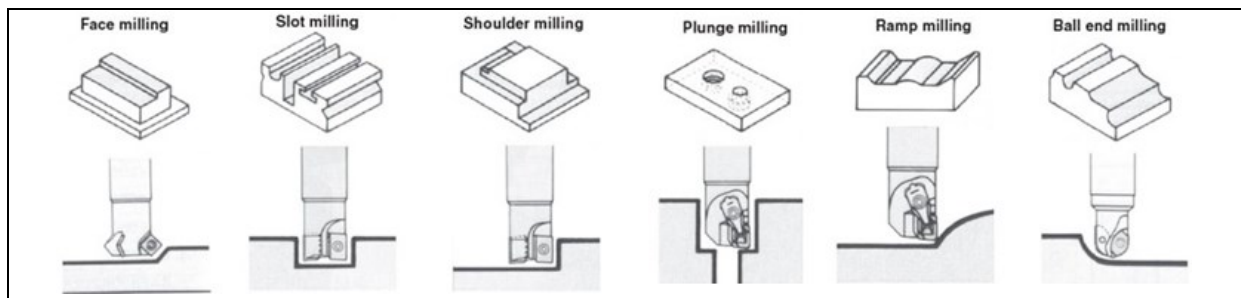


Fig 6. Various milling operations after [24].

Specialised milling cutters can also be used for more complicated features, without the need for more complicated operations, for example by using a T-slot cutter as shown in Figure 7 in T-slot milling. Other specialised milling operations include operations such as turn milling, in which the workpiece is rotated instead of feeding the milling cutter, and thread milling, to produce threading [26]. Finally, while some milling cutters are single, solid tools, milling cutters also include options with indexable, and replaceable inserts, allowing them to be used for longer without replacing the complete tool [27]. While generally tools are used with the maximum number of inserts, as this maximises the efficacy of the process, it has been found that a lower number of inserts can lead to longer tool life in face milling, when comparing equivalent conditions of feed per tooth [28].



Fig 7. A Specialised milling cutter with indexable inserts used for T-slots. Source: Seco Tools.

2.2.2 Milling Equipment

Similar to the broad range of process, and tool options, the range of equipment available for milling is very broad, ranging from basic stations, to multi-axis CNC machining centres, such as shown in Figure 8 below. Being a complex operation, due to presence of at least two concurrent movements, its outcome is highly dependent on the quality, and condition of equipment used [25]. A milling operation includes, in addition to the tool, workpiece, and machine, other factors that can affect the quality of the outcome, such as fixturing equipment, which can have an impact on the stability or the damping of the operation [29].



Fig 8. A Bridgeport XR 1270 CNC Milling Center equivalent to the one used in this research [30]

2.2.3 Parameters and Cutting Geometry in Milling

The cutting geometry in milling is defined by the main cutting parameters, which are cutting speed v_c , feed per tooth f_z , axial depth of cut a_p and radial width of cut a_e [26]. While a_p and a_e can be independently chosen, cutting speed in m/min is calculated as shown in Eq. 2.1, where D is the total tool diameter in mm, and n rotational speed of the tool in RPM [25]:

$$v_c = \frac{\pi \cdot D \cdot n}{1000} \quad \text{Eq. 2.1}$$

Feed per tooth, f_z on the other hand, describes the distance of linear translation of the tool corresponding to a single cutting edge, which can be derived from table or feed speed v_f in m/min, number of cutting edges z , and the rotational speed n in RPM [25], as shown in Eq. 2.2:

$$f_z = \frac{v_f}{z \cdot n} \quad \text{Eq. 2.2}$$

2.2.4 Up and Down Milling

Up milling and down milling are two common methods used in milling operations, differing in the direction of the cutter rotation relative to the feed direction of the workpiece. While down milling is

generally preferred wherever possible, each method has its own advantages and disadvantages, and the choice between them depends on various factors including the workpiece, tool configuration, and the desired surface finish [25].

2.2.4.1 Up Milling (Conventional Milling)

In up milling, as shown in Figure 9 below, also known as conventional milling, the direction of the cutter rotation is opposite to the feed direction of the workpiece. As the milling cutter rotates, the cutting action begins with zero thickness and gradually increases to the maximum thickness of the cut. This means that the cutting force starts at zero and increases to its maximum. It also can cause the cutting tool to rub the surface of the workpiece, and leads to forces that can lift the workpiece off the table, which needs to be considered during fixturing [29].

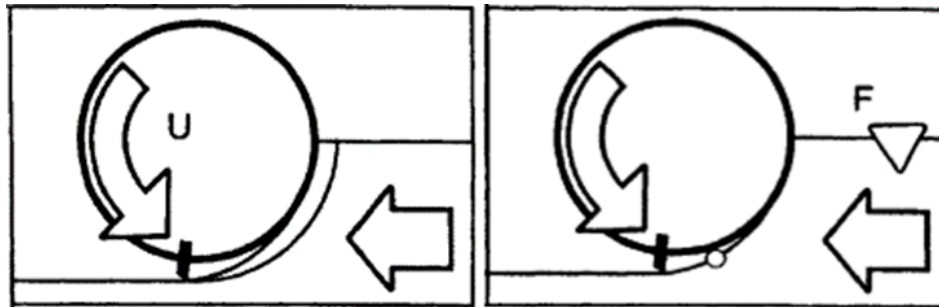


Fig 9. Up Milling after [29].

2.2.4.2 Down Milling (Climb Milling)

In down milling, as shown in Figure 10 below, also known as climb milling, the cutter rotation direction is the same as the feed direction of the workpiece. The cutting action initiates with the maximum chip thickness and ends at zero thickness. This approach tends to pull the workpiece into the cutter, which can result in a more stable operation with certain setups [29].

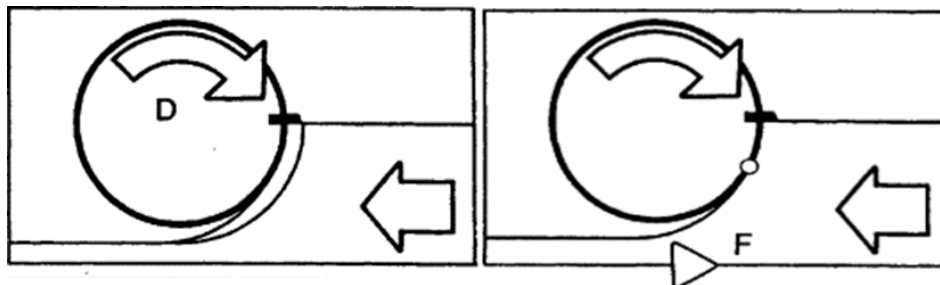


Fig 10. Down milling after [29].

2.3 Cutting Tool Materials

Cutting tools for machining operations are made from a variety of different tool materials, which span not only the realm of metals and their alloys, but also include options such as cemented carbides and ceramics, but also more advanced materials such as Cermets, which are composites of ceramics and metals, polycrystalline diamond, and cBN [31].

For example, the common tool material known as High Speed Steel, HSS, named in the early 20th century for its then superior properties when it came to machining ferrous materials, compared to the then common carbon steel tools. The superior properties of HSS mostly stemmed from its ability to maintain a stable cutting edge at higher temperatures without a major reduction in hardness, hence the

naming. HSS has however widely been replaced in industrial applications by newer materials, which in turn excel through being able to be used at even higher speeds [31].

During modern machining processes, due to the forces and subsequently, temperatures present, the cutting process not only depends on physical properties and geometry, but also chemical interactions and stability. The choice of appropriate tools is therefore not only dependent on factors such as hardness, and cost, but also chemical composition, and if present the coating used [31].

But in addition to newer materials requiring more advanced tools, better tool materials can also aid in improving efficiency in machining more traditional workpiece materials, by requiring fewer tool changes, and maintaining good surface finish quality for longer. One example of such an application is cast iron, which has historically been machined using HSS tools, but which is now being replaced by cemented carbide, ceramic, and cBN tools.

2.3.1 Cemented Carbide Tools

As a tool material, cemented carbide refers to a class of materials made up of carbide particles held by together by a phase of a metal binder material. Produced through powder metallurgy, their constituent carbides consists of mainly tungsten carbide (WC), while often including combinations of other carbides, nitrides, or carbonitrides, with the binder usually being Cobalt (Co) or Nickel (Ni) [31].

Their production involves two phases steps, the powder preparation, and the processing of the tool itself: First, the desired mixture of carbides is prepared and mixed with binder material, which is then pressed, and sintered into a rough shape, after which the roughly shaped pieces are grinded into their final shape, in addition to their cutting edges being prepared, followed by a coating process [31].

While generally known for their combined hardness, and toughness, as a result of their matrix structure, as they are produced from a powder mixture, and coated, their specific properties can be adjusted to any various specific application, which makes them a highly versatile tool material [31].

2.3.2 Ceramic Tools

Ceramic tools have high hardness and are resistant to elevated temperatures. They are however comparatively brittle, which limits the range of possible cutting speeds they can be used at. They are most commonly made of Al_2O_3 (Alumina) or Si_3N_4 (Silicon Nitride), both of which have some advantages and disadvantages [31].

Al_2O_3 , while being very is also very brittle, which is why it is often found reinforced with SiC (Silicon carbide) whiskers. This structural reinforcement highly increases the toughness of the brittle Al_2O_3 matrix, which in this combination is used for the machining of Nickel-based alloys. Si_3N_4 cutting tools on the other hand, which have less brittle are often used for the machining of cast irons, where the higher toughness of the material is beneficial [31].

2.3.3 cBN Tools / Polycrystalline cubic Boron Nitride

cBN refers to cutting tools made out of polycrystalline cubic Boron Nitride (PCBN), which is an extremely hard material, being second only to diamond. However, in its use as a cutting tool material, it excels in comparison to diamond due to both its inertness to iron, and its ability to maintain hardness at high temperatures [31]. As it is purely human-made and not present in nature [31], it has to be specifically manufactured for its use in cutting tools.

This is done by subjecting powdered hexagonal boron nitride (hBN) to high pressures and temperatures, under which it forms particles of cubic boron nitride (cBN) [31], assuming a crystal structure analogous

to that of diamond [32]. This cBN is then further processed by being mixed with a binding material, and afterwards again being subjected to the high pressure and temperature environment, to form PCBN [31]. The resultant structural similarity of cBN to diamond, which results in comparable physical properties [32], while being inert to ferrous alloys and resistant to higher temperatures, makes PCBN a relevant tool material, which has been finding use in machining, among other materials, cast irons [31].

2.4 Tool Wear and Tool Life

Tool wear refers to the collection of physical or chemical change that affect the performance of a cutting tool during machining. This is a result of the physical contact and impacts between the surface of the tool and of the workpiece. Tool wear can encompass various types, the most commonly considered ones being rake wear, and flank wear, referring to the two sides of the tool engaged in the cutting process. Other types of tool wear include notching, chipping, adhesive wear, thermal cracking, and plastic deformation [31]. These types also differ in their growth or development patterns, with some kinds of tool wear being more progressive and consistent, and other being stochastic.

While tool wear as a term encompasses different types of wear which are mostly categorized by the topology their formation, there are different mechanisms of wear formation, or load factors, which can act individually or in unison to cause tool wear. The main mechanisms of tool wear formation include mechanical loads, abrasive loads, thermal loads, and chemical loads [25].

2.4.1 Flank Wear

Flank wear, which appears on the flank side, which supports the tool on the workpiece generally follows a pattern of three distinct phases: In the first phase, the tool wear VB experiences an initial spike, as the sharp edge of the tool is worn off, before stabilizing. This is followed by the second phase which exhibits a more linear wear development. In the third region wear increases rapidly as VB approaches a critical limit, an example of which is shown in Figure 11 below [24].

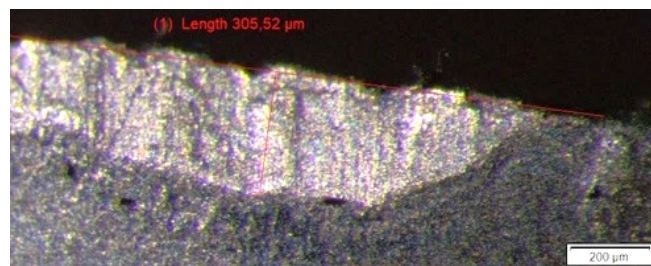


Fig 11. Image showing flank wear on a cemented carbide insert.

Flank wear causes the clearance angle to be worn down, increasing the contact length on the flank of the tool and thus the mechanical load and cutting resistance [31]. Therefore the cutting forces experienced by the cutting tool also increase with increased VB [31].

2.4.2 Crater Wear

Crater wear refers to a specific type of wear mainly observed on the rake side of tools used in machining operations and is characterized by the formation of a depression or "crater" on the surface of the cutting tool, as shown in Figure 12 below. Its extent is generally measured is based on crater depth, KT . Crater wear occurs due to the intense heat and pressure generated during the cutting process, which together with chemical effects, and repeated material adhesion and removal can lead to material being removed from the tool itself. This effect usually begins close to but not at the cutting edge, although the crater can reach the cutting edge, particularly in short chipping material [31].

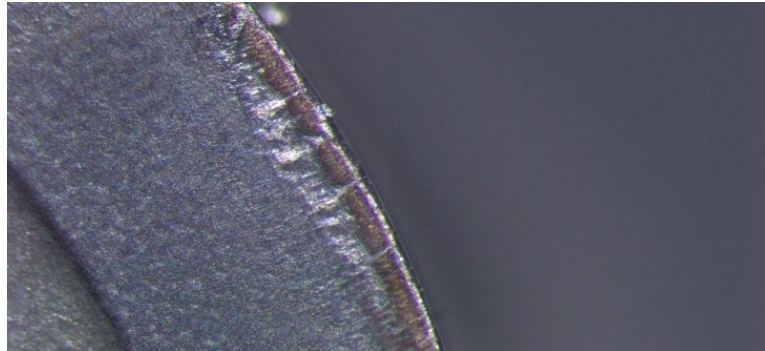


Fig 12. Image showing crater wear on a cemented carbide insert.

Crater wear is a critical element in machining as it can weaken the cutting edge by reducing the wedge angle. Hence it directly affects the tool life and the quality of the machined surface. As this effect also increases the rake angle, crater wear can lead to a small reduction of cutting forces [31].

2.4.3 Tool Life

Tool wear is an important consideration as its type and degree affect the cutting process a given tool is used in. This effect can be in form of increased vibration, lower surface quality, increased workpiece temperature due to worse chipping behaviour, or higher energy use [31]. The period of time that is considered productive time for a given tool is hence called the tool life [25].

Tool life therefore refers to the time a given tool maintains its function within a certain operation, i.e. before tool failure. This is to be differentiated from the wear criterion, which is the accepted limit of tool wear until which a tool is used before replacing, with a margin of safety considering the risk of tool failure [31]. In the case of flank wear, this limit is based on the distance of the wear line to the cutting edge, VB , and in case of cratering, it is based on crater depth, KT . In the case of tools with an edge radius, the contact length on the flank face can be represented by the sum of the edge radius r_β and the flank wear VB [31].

As the wear criterion is a choice made for a given application, it therefore also depends on the purpose of the operation, for example differing between roughing and finishing operations, i.e.: a milling tool can likely be used for longer in a roughing operation, compared to a finishing cut, due to the lower demands on surface quality. Therefore, the wear criterion in roughing is often closer to tool life [31].

Tool wear measurement can be conducted using methods that analyse the propagation of wear and by establishing relationships between it and the tool material and cutting conditions. This is based on regular measurements of tool wear development, and covers method such as using the Taylor equation, or the Colding model, which is used in this research. A second method instead relies on sensor measurements during a cutting operation, by observing patterns and changes in things such as vibration, cutting forces, or acoustic emissions [33].

2.5 Machinability

The concept of machinability describes how easy or difficult it is to shape or cut a certain material, in this context mostly referring to metals, in an intended manner. As several factors and material properties determine this ease or difficulty of machining different materials, all with their own challenges, machinability is generally not seen as a single variable, but rather a multidimensional property, covering aspects such as hardness, or thermal properties [34].

One model covering machinability is the polar diagram by Ståhl and Andersson [34], with an example given in Figure 13 below. This model uses the effects of abrasiveness, adhesion or ductility, strain

hardening, thermal conductivity, and hardness, as five factors representing machining difficulty. These are represented as five points on a pentagonal polar diagram, which shows their level, relative to the low alloy steel SS2244, which is used as reference material, with its values being set at 5. In general, therefore, a material that is easier to machine will have a smaller overall distribution than a material that is more difficult to machine. It should be noted that in case of thermal conductivity, a higher value, represents lower thermal conductivity, as heat buildup reduces machinability.

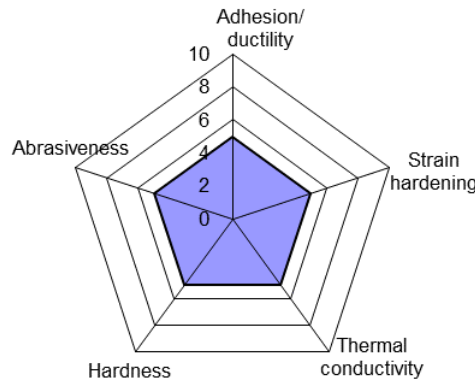


Fig 13. Polar diagram showing the potential machinability of SS 2244, the reference material used in Ståhl's and Andersson's model [34].

Due to its multidimensional breakdown of machinability, the model allows differentiation between materials which are difficult to machine due to a single property, and materials which instead are difficult to machine to a combination of factors. Hence a highly adhesive material as shown in the example in Figure 14 below, will have a graph tending towards that particular side [34].

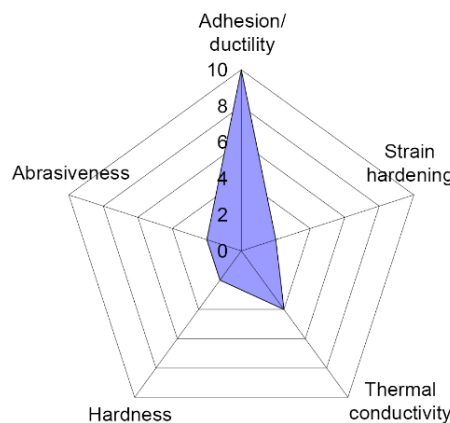


Fig 14. "Illustration of a polar machinability diagram for a highly adhesive material" [34].

By visualising machinability this way, the polar diagram model intends to connect machinability parameters to tool selection, in terms of both the cutting tool material, and also tool geometry, in addition to allowing to better evaluate the effects of different cutting conditions [34].

2.6 Economic Modelling in Manufacturing

The ability to predict manufacturing costs of a given part accurately ahead of production is invaluable to companies. However, due to the large number of variable factors, many of which are hard or impossible to predict, such as unscheduled downtimes, quality issues, or tool failures, it has generally been easier to accurately calculate part cost retroactively, compared to advance prediction [35].

2.6.1 Tool Life in Cost Models

Models such as Ståhl's cost model for metal cutting [35] therefore aim to approximate part costs based on statistical approximations of variable costs, together with known costs, such as material, wages, or machine costs, and due to its importance in machining, also aim to use tool life as a factor in their model. This both adds another set of uncertainty, due to difficulties around predicting tool life, in addition to more choices that are needed, in regards the choice of a wear criterion, as for example a higher wear criterion might trade increased tool life, for lower surface quality.

With the need to balance time-based costs such as operator and machine time, with costs such as tooling time, and tool replacement cost itself, tool wear is therefore both useful as a criterion, in order to find the most economical cutting conditions for a given process, but also as a variable within the cutting conditions itself, as with increased tool wear, a cutting process might continuously deteriorate [35]. To fully model costs and to calculate the most economical production conditions therefore, it is essential to also be able to model tool life.

2.6.2 Material Removal Rate

Another tool that is used for aid in evaluating and comparing cutting and process data in machining operations from an economic perspective is material removal rate (MRR). MRR is a measure which refers to the amount of material removed from a workpiece over a certain amount of time, which in case of machining is equivalent to chip flow, and can be calculated as shown in Eq. 2.3 [31]:

$$MRR = \frac{\text{Volume Removed}}{\text{Time}} = \frac{dV}{dt} \sim a_p \cdot f \cdot v_c \quad \text{Eq. 2.3}$$

The importance of MRR lies, in addition to comparing cutting conditions, in its use when calculating part costs, as a high MRR will generally lead to shorter tool life, and hence more tool changes and tooling time, while a low MRR will lead to worse utilization of operator and machine time, with the optimal cutting conditions laying in between, as shown in Figure 15 below.

As it is not dependent on the tool itself, MRR has therefore also been used to compare different cutting tool materials from a production cost perspective in combination with tool life prediction models such as Colding [36].

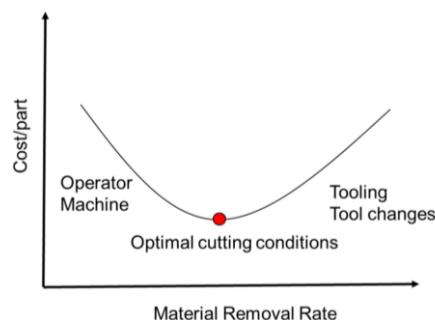


Fig 15. Material removal rate used as a method to balance part cost factors [37].

2.7 Tool Life Models

Since the industrialisation of manufacturing, there has been economic value in optimising manufacturing operations. This was already recognized by F.W. Taylor, known for his influential work on scientific management, a management theory that analyses and synthesizes workflows to improve economic efficiency, who as early as 1906 published what is now known as the Taylor tool life equation

[38], which connected cutting speed v_c , tool life T , and two model constants, n , and C , as shown in Eq. 2.4 below:

$$v_c \cdot T^n = C \quad \text{Eq. 2.4}$$

2.7.1 Colding Tool Life Model

A later, more advanced model was proposed by Colding [39], whose tool life prediction formula is a function of cutting speed v_c , equivalent chip thickness h_e , and tool life T , in addition to five fitting constants, K , H , M , N_0 , and L . The resultant Colding equation takes the form shown in Eq. 2.5 [37]:

$$v_c = \exp \left[K - \frac{(\ln(h_e) - H)^2}{4 \cdot M} - (N_0 - L \cdot \ln(h_e)) \cdot \ln(T) \right] \quad \text{Eq. 2.5}$$

As shown in Figure 16 below, the Colding model connects tool life, to process data, and the wear criterion as a limit, by using the five model constants.

While allowing for more accurate modelling than Taylor's equation, due to using five modelling constants, at least five test results are required to calculate the model constants. The Colding model is, alike Taylor's equation only valid in a certain range of cutting conditions, where the relation of $\log T$ and $\log v_c$ is linear. It is not intended to work at very low speeds or feeds, where built up edges (BUE) will be the prevalent wear development, nor at very high ones, where extreme temperature could cause deformation to the tool [37].

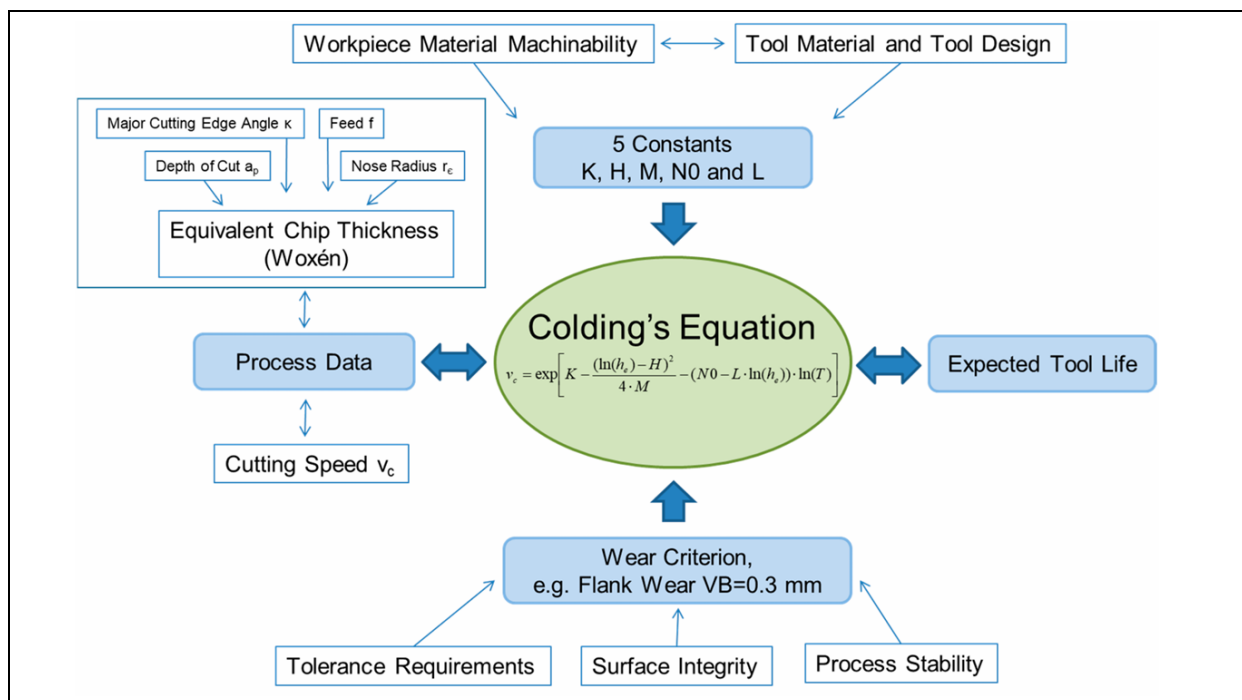


Fig 16. Schema showing the Colding model and the connections between its elements [37].

2.7.2 The Five Model Constants, K , H , M , N_0 , and L

The Colding model uses five model constants, K , H , M , N_0 , and L , to connect the real-world variables of the equation. While the five model constants have not been connected to any physical aspect of the cutting process, there is an established connection between the constants and the geometry of the Colding curves [37].

2.7.2.1 Model Constant K

An increased K constant is associated with an increase in the recommended cutting speed, lifting the Colding curves upwards, i.e. a higher K constant implies better machinability as the tool can run at higher speeds, for a given tool life [37].

2.7.2.2 Model Constant H

A changing H constant moves the Colding curves horizontally, with a larger H shifting the curves to the right [37]. Hence, a larger H means that the maximum cutting speed for a given tool life can be sustained at a higher equivalent chip thickness, implying higher MRR.

2.7.2.3 Model Constant M

The M constant is related to the curvature of the Colding curves, with a negative M value giving a downwards hanging curve, with a lower M meaning that the model is more sensitive to equivalent chip thickness h_e in regards to tool life, and with $M=0$ leading to flat horizontal lines [37], which would theoretically imply that a change in chip thickness does not affect tool life.

2.7.2.4 Model Constant N_0

The N_0 constant affects the vertical distance between the curves, with a small N_0 leading to more closely packed lines, which would imply a higher sensitivity to changes in cutting speed in regards to tool life [37].

2.7.2.5 Model Constant L

The L constant appears to affect the relative angle or parallelity of the Colding curves, with $L=0$ leading to parallel curves, and situations with $L \neq 0$ leading to the occurrence of a Colding singularity at the point of intersection [37].

2.7.3 Singularity

The singularity that occurs when $L \neq 0$ refers to a point in the Colding plane where the different lines representing tool life meet. As this implies that physically, at that point of v_c and h_e , all tool life possibilities converge, which is impossible, the existence of this point causes difficulty when intending to use the Colding model in that region [37].

2.7.4 Use of the Colding Model in General and in Milling

The Colding tool life model overall finds less common use than the older Taylor model of tool life, with a Scopus keyword search with the parameters “tool”, “life”, and “Taylor” giving 2071 search results, whereas “tool”, “life”, and “Colding” yielded 14 results. While part of this difference might be attributed to other factors, including unintended results, it nevertheless confirms that the Taylor model remains more prevalent, even though research has shown the Colding model to provide better approximations [40]. While the adaptation of the specific geometry of milling to the Colding model has been previously studied [41], the use of the Colding furthermore mostly remains limited to turning, with its applicability in milling having only been researched to a limited extent so far by Kantojärvi et al. [10], who achieved a model error of 7.96 %, which therefore remains the only benchmark for the Colding model in milling.

3 Methodology

This section describes the procedures and conditions under which the experiments were implemented, and the numerical methods used to evaluate the data, including adaptations to the original Colding model to use it in milling. It covers an in-depth description of the process, the equipment and instruments used, the cutting tools, and the workpieces utilized, and the methods used for preparing samples for microscopic examination. As this thesis was conceived as first part of a larger study which replicates the experiments with different tool and workpiece materials, some decisions regarding the methodology such as tools, or cutting data, were chosen with enabling comparable experiments in mind. This section also presents the results of the nanoindentation, as these were precursor to other steps of this research.

3.1 Overview of Experimental Process

With the goal being to form a suitable Colding equation, the main experimental aspect of this study consisted of observing the flank wear evolution of cemented carbide inserts used during the CNC-milling operation of CGI workpieces. In addition to this main part, other tests were conducted to support the research, namely the microscopic analysis of LGI, CGI, and SGI cast iron samples to study skin effects, and hardness analysis of these samples through nanoindentation.

3.2 Cutting Tool

For this research, an indexable cemented carbide face mill by SECO Tools was used, which was provided by the manufacturer.

3.2.1 Insert

The insert used for this research, the RPKW1204M0T-6-MD10 MK2050 (Product number 02923731) by Seco Tools is a single sided indexable insert made of coated cemented carbide, with six cutting edges, as shown in Figure 17 below. The insert diameter is 12mm, and the insert has a 11.0 degree clearance angle, and a 0.0 degree insert rake angle. The insert is coated with a proprietary grade designated MK2050 by Seco Tools, which is applied through physical vapor deposition (PVD) [42]. The MK2050 grade is designated by Seco Tools to be for material strength classes ISO K (cast irons), ISO P (steels except for austenitic stainless steels), and ISO H (hardened steels and cast irons) [43], [44]. It is given the highest rating (5 stars out of 5) for abrasive wear resistance by Seco Tools, among their 12 grades of coating for milling [44].

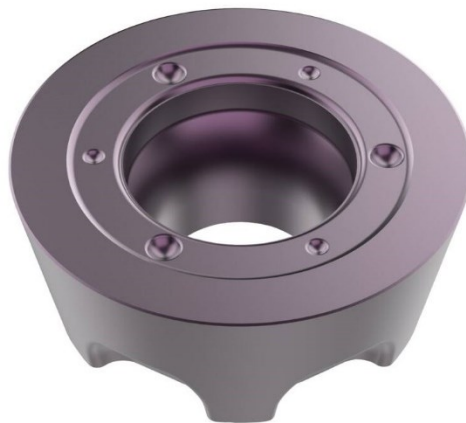


Fig 17. Image of RPKW1204M0T-6-MD10 MK2050 insert, as used in this research [42].

3.2.2 Milling Cutter

The milling cutter used for this research, the R220.29I-0080-06.6A (Product number 02949625) by Seco Tools, is an 80mm (DCx), 68mm (DC) diameter facemill for cemented carbide inserts, as shown in Figure 18 below. It has a -3.0 degree radial, and a 4.0 degree axial rake angle [45].



Fig 18. Image of R220.29I-0080-06.6A milling cutter, as used in this research [45].

3.2.3 Combined Milling Tool

For this research, the aforementioned R220.29I-0080-06.6A milling cutter was mounted on a standard DIN40 tool holder. For any given test, one single RPKW1204M0T-6-MD10 MK2050 insert was mounted on the milling cutter. While the insert used has six cutting edges, only three were used from any insert, leaving intermittent ones unused, to prevent damage to other neighbouring cutting edges during other machining operations, which could affect measurements. The combined tool had a 7.0 degree clearance, -3.0 degree radial rake, and 4.0 degree axial rake angle. The combined tool together with a mounted insert is shown in Figure 19 below.



Fig 19. Image of combined tool and tool holder with a single insert attached.

3.3 Workpiece

The material used in the machining processes of this thesis were highly pearlitic CGI450 workpieces supplied by Volvo Trucks, which were made using process control by SinterCast, examples of which are shown in Figure 20 below. While the exact size varied between pieces, their dimensions were generally around 260·260·90 in mm.



Fig 20. As cast CGI450 workpieces equivalent to ones used in this research.

With the material having been supplied in different batches, while the possibility for some variability between individual workpieces could not be fully neglected, it was considered that the impact itself of such a variation would be negligible. Similarly, effects from aging and storage, were assumed to be negligible.

However, skin effects, which can arise during the cooling after casting of the workpieces, which can have a major effect on the microstructure of the material's outer surface areas, and in turn on the material properties of these regions, were investigated.

While due to time limitations, milling tests were only conducted on CGI450, three different cast irons were studied in the hardness tests during this research. Table 2 below shows the chemical composition of alloying elements in the workpieces used in this research, with the information having been provided by Volvo Trucks. Here it can be seen that the CGI450 samples have a low titanium (Ti) content of 0.0035%, with titanium being an alloying material that was previously used to increase the production range of CGI, which is now avoided due to its effects on machinability [16].

Table 2. Chemical Composition of materials used in wt%, and Carbon Equivalent .

	C	Si	Mn	S	Cr	Cu	Mg	Sn	Ti	CE
Gray Cast	3.29	3.18	0.73	0.085	0.21	0.52	<0.0004	0.0055	0.0045	3.77
CGI350 (SSF)	3.45	3.18	0.141	0.066	0.0029	0.051	0.032	0.0079	0.011	4.25
CGI450	3.65	2.29	0.135	0.006	0.031	0.92	0.007	0.086	0.0035	4.23

3.4 Skin Effect Analysis and Nanoindentation Tests

As the exact casting process of the workpieces was unknown, it was unknown whether the CGI's material properties propagated homogeneously throughout the bulk, and some skin effects were expected. In order to study whether or not the skin layer of the workpieces used had different microstructures compared to the core, hardness tests based on nanoindentation were conducted.

To study this, samples of LGI, pearlitic CGI450, and ferritic CGI350, which had been cut from different edges of workpieces equivalent to the ones used in this study were used. These samples been previously cut and encased in bachelite, and were repolished to remove oxidation. To analyze their microstructure, they were scanned using an Alicona microscope of the Production and Materials department at LTH, as shown in Figure 21 below.

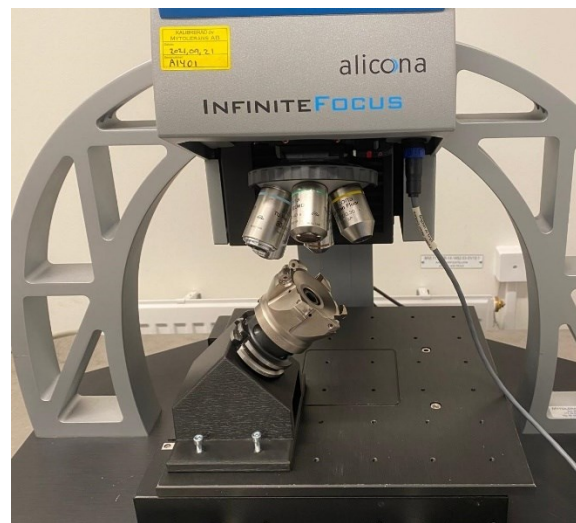


Fig 21. Alicona Infinite Focus Microscope, used for the microstructure analysis of material samples, here shown with a custom toolholder and the milling cutter used in this research.

For each material, nine sample were studied, covering different location of the original workpieces, in order to be able to select the sample with the most consistent surface, as some samples had major inclusions the surface which would have made a direct comparison more difficult.

After scanning the microstructure microscopically, covering at least an area of 15x10 images, where one image covered about 400·600 μm , the images were stitched together and analysed, with one example shown in Figure 22 below.



Fig 22. Stitched image of CGI surface layer (cropped).

Based on the stitched images, one sample was selected for each material. This selection was made based on a visual review only, as the only requirement was a consistent structure in the skin area. For each of the selected samples, hardness tests based on nanoindentation were then conducted.

The nanoindenter used was a Micro Materials NanoTest Vantage of the Production and Materials department at LTH, as shown in figure 23 below, using a Berkovich tip.

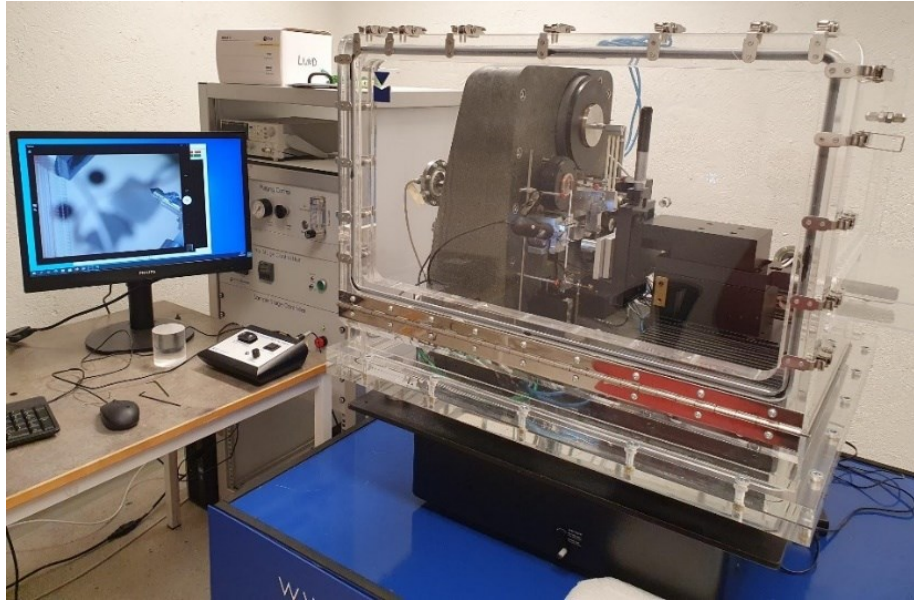


Fig 23. NanoTest Vantage nanoindenter used for this research [46].

The nanoindentation tests were conducted on the three selected samples, in a rectangular area of a 10x20 testing points of 50mN maximum load, based on a 10 μ m square pattern, starting orthogonally at one of the original mould edges. As the aim was to measure the transition in direction orthogonal from the edge, this would yield 20 layers with 10 data points each, which would reduce errors stemming from the heterogeneous nature of the material. This approach was designed to capture the gradation in hardness as it transitions from the surface towards the bulk of each material.

3.4.1 Nanoindentation Results

Based on the nanoindentation tests, hardness measurements for the three selected samples were collected. Due to existing limitations in the equipment used, the hardness values found during the tests, cannot be seen as absolute, and will only be used for relative comparison. As the goal was only to establish whether or not a gradient existed, this was found acceptable. Table 3 below shows the average relative hardness results for the three samples tested.

Table 3. Average values per layer of relative hardness (Complete Data in Appendix A).

Layer:	<u>1</u>	<u>2</u>	<u>3</u>	<u>4</u>	<u>5</u>	<u>6</u>	<u>7</u>	<u>8</u>	<u>9</u>	<u>10</u>	<u>11</u>	<u>12</u>	<u>13</u>	<u>14</u>	<u>15</u>	<u>16</u>	<u>17</u>	<u>18</u>	<u>19</u>	<u>20</u>
CGI	4.46	4.31	4.24	4.19	3.54	4.25	3.26	3.82	3.73	3.51	2.75	3.29	2.93	3.78	3.84	4.49	4.26	3.92	3.38	2.86
SSF	3.85	4.14	3.77	4.32	4.19	3.75	2.50	2.22	1.97	2.55	2.65	2.78	3.52	3.58	3.30	3.23	4.18	3.49	3.78	4.27
Gray	4.87	4.80	4.49	5.16	4.60	5.01	4.07	3.50	2.46	3.12	2.39	2.16	2.10	0.92	0.97	0.75	0.67	0.70	0.67	0.54

Using the data from Table 3, the following graphs in Figures 24, 25, and 26 visualize the hardness gradient measured from the surface for the three materials.

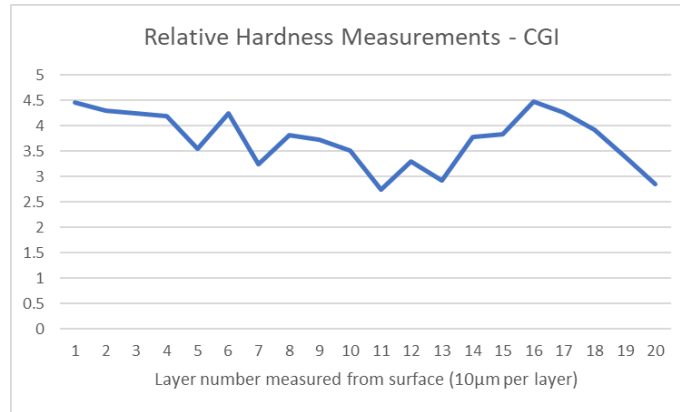


Fig 24. Gradient of relative hardness for CGI450 sample.

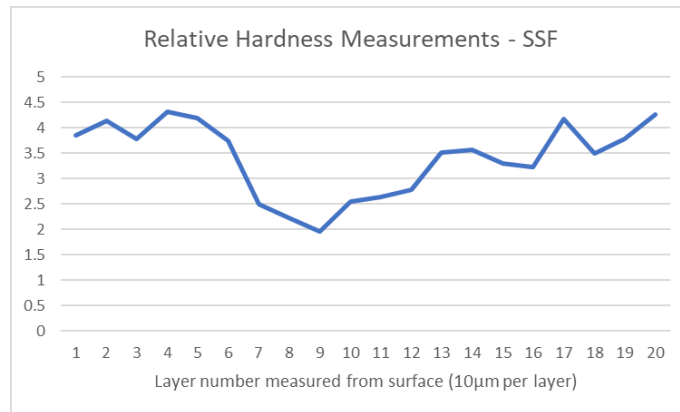


Fig 25. Gradient of relative hardness for CGI350 sample.

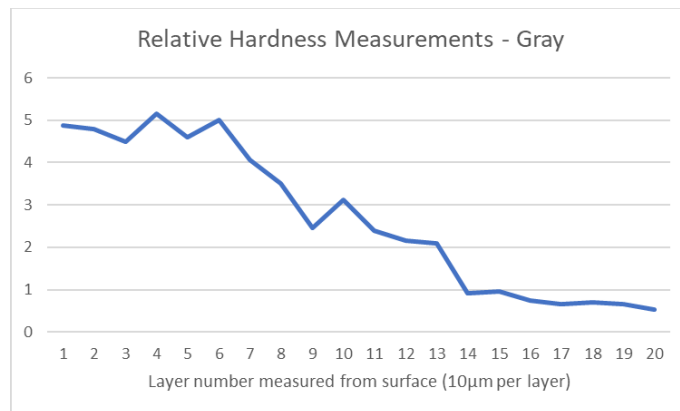


Fig 26. Gradient of relative hardness for Gray Cast Iron (LGI) sample.

While the data is limited by the fact that the absolute values are unclear, what can be observed is that in all materials, hardness is irregular at the surface level. As the measurements are averages of ten tests per layer, it can be assumed that this is not only due to heterogenous phases, such as graphite, which would have lower hardness. Hence, while the exact effects to the microstructure cannot be determined, it can be established that the material properties at the skin level might be different from the bulk, and that therefore, pre-machining for skin removal is required for accurate tool life testing.

3.5 Skin Removal

While it would be preferable from an economic standpoint, to be able to remove the skin layer in the same operation as the rest of the machining, with the goal in this research of developing a Colding equation cutting data from a homogeneous material is required. While the nanoindentation tests were

not able to measure the absolute properties of the skin layer, they established that all three materials, including CGI450, which is the main subject of this research, experienced skin effects, with hardness values varying at the outermost layer, which implied different microstructures compared to the bulk material. Therefore, the workpieces were pre-machined on all sides, to a final size of 250mm*250mm in depth and width, while height varied slightly for each workpiece, with an example operation shown in Figure 27 below.



Fig 27. Image of an interrupted pre-machining process, of a workpiece equivalent to the ones used in this research.

3.6 Machinability of CGI

In Figure 28 below, the polar machinability diagram for different grades of compacted graphite iron is shown, highlighting the most relevant considerations of machining CGI. As can be seen, one of the major problems related to CGI is its low thermal conductivity, hence it can be expected that high thermal loads will be encountered during the machining tests.

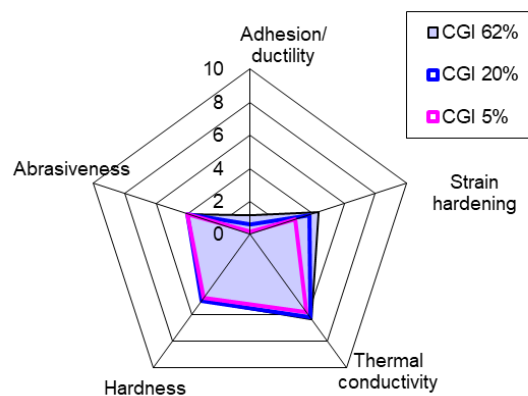


Fig 28. Polar diagram showing the potential machinability for three types of CGI with different percentages of compacted graphite structures.

3.7 Milling Tests

All machining tests were conducted using a Bridgeport XR 1270 Vertical Machining Center of the Production and Materials division at LTH. For all tests, 50% engagement width, i.e. $a_e = 40mm$, and a cutting depth of $a_p = 1mm$, was kept constant. The machining was done using down-milling.

The milling tests were done in equivalent straight passes over the workpiece. As the workpiece width after pre-machining was 250mm , and with $a_e = 40\text{mm}$, it was possible to conduct six passes per layer, with the remaining 10mm being removed by a second tool during an intermediary clean-cut operation. For each pass, pass length was calculated as beginning with tool entry, and ending when 50% of the tool had disengaged, at which point the cutting process stopped, the calculation being shown in Eq. 3.1 below:

$$l_{pass} = l_{workpiece} + \frac{D}{2} = 250\text{mm} + 40\text{mm} = 290\text{mm} \quad \text{Eq. 3.1}$$

For cutting speed v_c , and feed per tooth f_z , eight cutting conditions were chosen as test points. While theoretically, five points are sufficient to solve the system of equations of the Colding model, increased tests can improve the accuracy of the model's predictions [37]. Additionally, having extra points allows for an analysis of different subsets, to control in the case of suspected outliers.

The selection of the parameters was based on the cutting data provided by the tool manufacturer Seco Tools, through Seco's cutting data tool: The points were chosen based on the tool manufacturer's recommended range as a starting reference, and cutting parameters were therefore also based on these. However, as milling toolholders such as the ones used in this thesis are conventionally designed for operations with multiple inserts, six in this case, when conducting single-insert machining, the changed cutting geometry must be taken into account, and the cutting parameters had to be adapted. As the number of cutting edges, z , is part of the equation for feed per tooth f_z , as shown in Eq. 3.2 below, in order to find the relevant f_z , feed speed v_f given by Seco's cutting data must be divided by six, while the other parameters remain the same, as they are independent of z .

$$f_z = \frac{v_f}{z \cdot n} \quad \text{Eq. 3.2}$$

As other cutting parameters, such as RPM were dependent on the established cutting data, the four cutting parameters can be established as shown in Table 4 below, with Figure 29 on the following page showing the distribution of v_c and f_z .

Table 4. Cutting data for 8 test points.

Test point	Cutting speed at DCw v_c (m/min)	Feed per tooth f_z (mm/tooth)	a_e (mm)	a_p (mm)
1	250	0.400	40	1
2	154	0.554	40	1
3	431	0.277	40	1
4	185	0.277	40	1
5	359	0.554	40	1
6	250	0.554	40	1
7	393	0.4	40	1
8	316	0.477	40	1

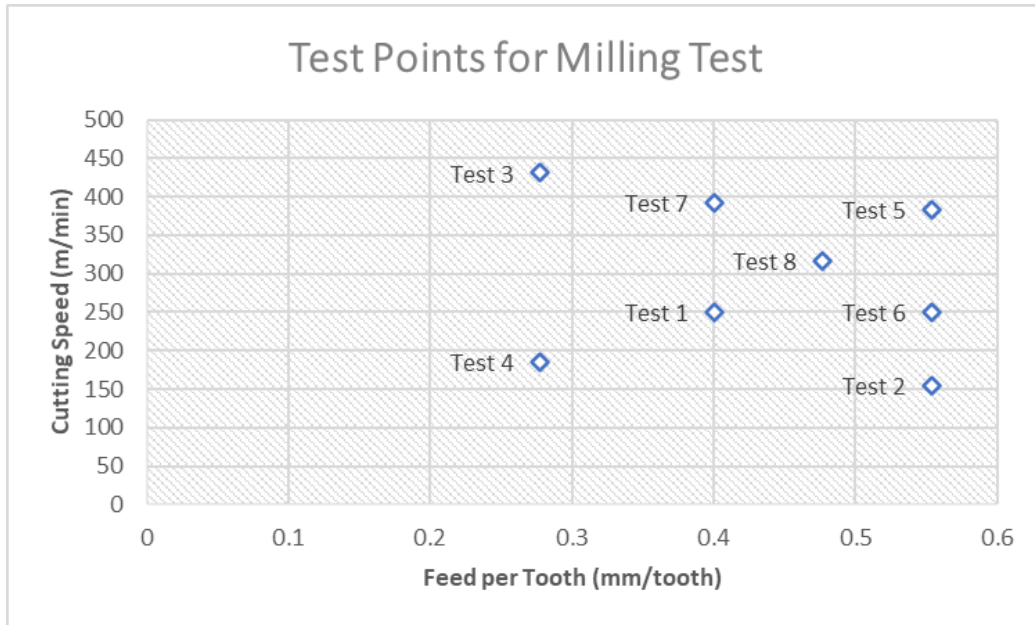


Fig 29. Cutting speed and feed per tooth data for the eight tests.

Due to the added importance of stability required for accurate tool wear observations, importance was also put on a stable clamping setup. The workpieces were held in place by four edge clamps, with a low side profile, which also allowed for more utilization of the material, as more layers were accessible, which is shown in Figure 30 below.



Fig 30. Clamping setup used during this thesis. Coolant leftover from a intermediate clean-cut can be seen on the workpiece.

3.8 Microscopy for Tool Wear

The tool wear measurements were conducted using an Olympus SZX7 optical microscope, as shown in Figure 31 below, together with Olympus Stream Basic Imaging Software. For these measurements, the cutting tools were mounted variably at a 45-60 percent angle, with the insert placed at the highest possible location. The goal was to observe the flank side at an angle that was as close as possible to orthogonal at the point of tool wear. Due to the curvature and short focal depth, it was not possible to observe the flank wear along the whole affected area, and therefore the most relevant area was chosen. Due to the high reflectivity, especially in adhesion regions, both the amount, but also the direction of the light was important to correctly observe tool wear.



Fig 31. Olympus SZX7 optical microscope used in this research, with adjustable toolholder visible.

3.8.1 Measurement Intervals

The measurements for building a Colding model can be based on different methods, with one being regular measurements between intervals of machining, as is done in this research, with a second option being based on measuring cutting forces until they reach the level of expected tool wear [7]. Both methods have advantages and disadvantages, nevertheless both have the possibility of overshooting the targeted wear and requiring extrapolation [31]. The cutting data method does not require regular measurements, however does also not provide information on wear development and requires a good understanding of the cutting process. The interval-method on the other hand takes more time and requires more manual measurements, but has a lower risk of overshooting by a larger amount. In this research, to further mitigate the uncertainty of wear development, more tests were done at the beginning and expected end phases of machining tests, until wear development was better understood. Measurements were taken at intervals that were appropriate based on the expected tool life and speed

of tool wear, to best use machine time, with most measurements being taken at ends of layers, i.e. after six passes, while in earlier tests, more regular measurements were conducted, as the wear development was not yet observed. Figure 32 below shows one of the inserts that were used in these measurements.

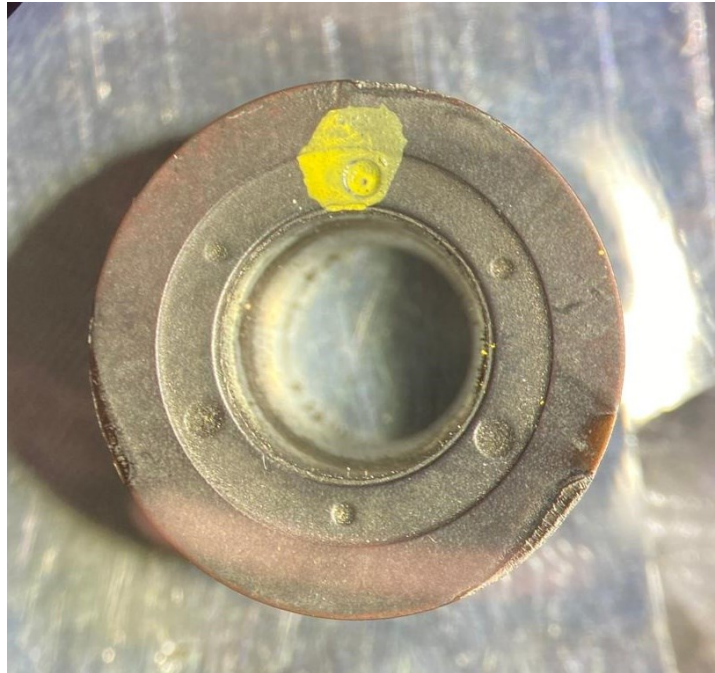


Fig 32. Image showing insert after three milling operations, a dot was painted on inserts to mark the order of tests.

3.8.2 Effect of Insert Curvature during Flank Wear Measurement

The curvature of the round inserts had two negative effects on microscopy, which had to be accounted for. While these are discussed in more detail later on, they will be shortly brought up here: Firstly, the combination of the curvature of the inserts and the holder fixture implied that during flank wear measurement, only one position, namely the highest one, along the flank of the insert could be perpendicular to the microscope camera. Therefore, during measurements at other points, there would be a slight deviation in flank wear measurement. However, due to the small area observed this effect can be considered negligible. Secondly, due to the curvature, and limited focal depth, it was not possible to view the complete cutting edge, which caused difficulties when the wear development became more prominent in another region, which required adjustment of the area in focus. Due to such adjustments, images of subsequent measurements were not always completely overlapping in the regions of maximum wear, which in these situations made it difficult to ascertain wear development more precisely. This should however also not have an impact on determining the point of maximum tool wear, i.e. the wear criterion.

3.9 Methods and Equations for the Colding model

As the Colding model was designed for use in turning, adaptations to the original model were required, which in this research were based on the methods proposed by Sören Hägglund [41], the application of which were first tested by Kantojärvi et al. [10], which confirmed their use.

It should be noted that while Hägglund proposes multiple versions of these equation based on insert shape and tool engagement, only the equations for round inserts and 50% engagement are presented, and some equations are therefore simplified or adapted from their general versions presented by Hägglund [41].

The known variables which are used for calculating the Colding model are shown in Table 5 below.

Table 5. Summary of variables of milling operation.

Test	v_{cDCw} (m/min)	f_z (mm)	DCx (mm)	DCw (mm)	a_e (mm)	a_p (mm)	l_{pass} (mm)
1	250	0.400	80	68	40	1	290
2	154	0.554	80	68	40	1	290
3	431	0.277	80	68	40	1	290
4	185	0.277	80	68	40	1	290
5	359	0.554	80	68	40	1	290
6	250	0.554	80	68	40	1	290
7	393	0.4	80	68	40	1	290
8	316	0.477	80	68	40	1	290

3.9.1 Adapting the Colding Model to Milling

Due to the intermittent nature of milling, two changes need to be made to the Colding model as both chip thickness varies during cutting, and the engagement time does not equal cutting time. The adaptations required will be explained below.

3.9.1.1 Step 1: Equivalent Chip Thickness

The first step for adapting the Colding equation, which is again shown here below in Eq. 3.3, is to adapt equivalent chip thickness h_e .

$$v_c = \exp \left[K - \frac{(\ln(h_e) - H)^2}{4 \cdot M} - (N0 - L \cdot \ln(h_e)) \cdot \ln(T) \right] \quad \text{Eq. 3.3}$$

The formula for equivalent chip thickness used in this research is based on an adaptation made by Hägglund [41] for milling with rounded inserts, to the Woxén model of equivalent chip thickness for turning [47], as shown in Eq. 3.4 below:

$$h_e \sim \frac{a_p \cdot f_{ze}}{\frac{d}{2} \arccos \left(\frac{\frac{d}{2} - a_p}{\frac{d}{2}} \right) + \frac{f_{ze}}{2}} \quad \text{Eq. 3.4}$$

This model requires the calculation of the effective feed per tooth, f_{ze} [41], as shown in Eq. 3.5 below.

$$f_{ze} = \frac{A_{CS_{he}}}{l_{arc_{he}}} \quad \text{Eq. 3.5}$$

The definition of this adapted feed per tooth is based on A_{CS} , the crescent shaped area covered by a single cutting edge, during a pass, and therefore requires its own definition first;

$$A_{CS_{he}} = a_e \cdot f_z - A'_{cs_{he}} \quad \text{Eq. 3.6}$$

Where $A'_{cs_{he}}$ is defined as;

$$A'_{cs_{he}} = \frac{DC_{w_{he}} \cdot f_z}{2} - \frac{DC_{w_{he}} \cdot f_z}{4} * \sqrt{1 - \left(\frac{f_z}{D_{w_{he}}} \right)^2} - \frac{D_{w_{he}}^2}{4} \cdot \arcsin \left(\frac{f_z}{D_{w_{he}}} \right) \quad \text{Eq. 3.7}$$

Where;

$$DC_{whe} = D_c + 2 \sqrt{a_{phe} \cdot (d - a_{phe})} \quad \text{Eq. 3.8}$$

Hägglund further proposes the use of a modified depth of cut for equivalent chip thickness, a_{phe} , as the weighted midpoint of the cone area of the chip, which he estimated at about 67% of the total cutting depth, which is calculated as shown in Eq. 3.9 below.

$$a_{phe} = \frac{67}{100} \cdot a_p \quad \text{Eq. 3.9}$$

Which can be plugged back into DC_{whe} ;

$$DC_{whe} = D_c + 2 \sqrt{\frac{67}{100} \cdot a_p \cdot (d - \frac{67}{100} \cdot a_p)} \quad \text{Eq. 3.10}$$

And

$$l_{arc_{he}} = \frac{DC_{whe}}{2} \cdot \left(\omega + \arcsin \frac{f_z}{D_{whe}} \right) \quad \text{Eq. 3.11}$$

Where ω is defined as:

$$\omega = \arccos \left(\frac{2 \cdot \delta - a_e}{DC_{whe}} \right) - \arccos \left(\frac{2 \cdot \delta + a_e}{DC_{whe}} \right) \quad \text{Eq. 3.12}$$

In which δ is defined based on milling type, which for down milling is defined as:

$$\delta = \frac{DC_{whe} - a_e}{2} \quad \text{Eq. 3.13}$$

Which lets us simplify ω as:

$$\omega = \arccos \left(\frac{DC_{whe} - 2 \cdot a_e}{DC_{whe}} \right) \quad \text{Eq. 3.14}$$

Giving:

$$l_{arc_{he}} = \frac{DC_{whe}}{2} \cdot \left(\arccos \left(\frac{DC_{whe} - 2 \cdot a_e}{DC_{whe}} \right) + \arcsin \frac{f_z}{D_{whe}} \right) \quad \text{Eq. 3.15}$$

3.9.1.2 Step 2: Cutting Time, Tool Life, and T_{ratio}

As to create a Colding equation, in addition to equivalent chip thickness, and cutting speed, the tool life is required as well, it is necessary to calculate it based on empirical tests. This is done based on the following equation, where NP represents number of passes until the wear criterion was reached;

$$T_{test} = t_{pass} \cdot NP \quad \text{Eq. 3.16}$$

The time per pass, t_{pass} in turn is derived by the feed speed v_f , and the pass length l_{pass} ;

$$t_{pass} = \frac{l_{pass}}{v_f} \quad \text{Eq. 3.17}$$

As mentioned before, due to the intermittent nature of milling compared to operations such as turning, the tool is only engaged for a fraction of the overall machining time, which has to be taken into account when calculating tool life.

For this, T_{ratio} , which represents the share of time during which the tool is engaged, $T_{engagement}$, in the cutting process out of the total cutting time, T_{Total} , as shown in Eq 3.18 below;

$$T_{ratio} = \frac{T_{engagement}}{T_{Total}} \quad \text{Eq. 3.18}$$

As engagement time is not known, T_{ratio} can also be calculated based on the process geometry, which for face milling depends on the engagement width, as shown in Eq 3.19 below:

$$T_{ratio} = \frac{a_e}{DW_x} \cdot \frac{1}{2} \quad \text{Eq. 3.19}$$

While for example during a turning operation, T_{ratio} would hypothetically be 100%, during slot milling it is 50%, and during side or shoulder milling operations, the T_{ratio} is further lowered by the engagement percentage, i.e., when for example shoulder milling at 68 % engagement, T_{ratio} would be 34 %. As all machining operations in this thesis are conducted at 50 % engagement to ensure maximum chip thickness at entry, T_{ratio} would therefore equal 25 %, or 0.25.

3.9.1.3 Step 3: Solving the Colding Model

Once the aforementioned changes to the variables used in the Colding model to adapt it to milling, are conducted, the system of equations can be solved using the implementation of the Levenberg-Marquardt [48], [49] least square data fitting method found in PTC Mathcad 15.

This requires the selection of initial values for the model constants. As there is no physical counterpart to the model constants, this requires iterative fitting.

4 Experimental Data

In this section, experimental results from machining tests are presented.

4.1 Tool Wear Measurements

In this section the measured flank wear (VB) after respective passes will be given for each test in conjunction with the calculated volume of removed material, which will be used in later comparison during the discussion of the data. As VB was measured until the criterion of $300\mu\text{m}$ was reached or overshoot, in some cases, the exact pass at which VB was reached was found by linear interpolation. While in this section the pass during which VB was expected to have reached the wear criterion is shown, when calculating tool life later in this study, the exact interpolation was used.

In addition to the tabular view, a graphical overview showing wear over passes, i.e. volume removed in Figure 33, and Figure 34 below, with the latter excluding Tests 2, and 4, for better visibility.

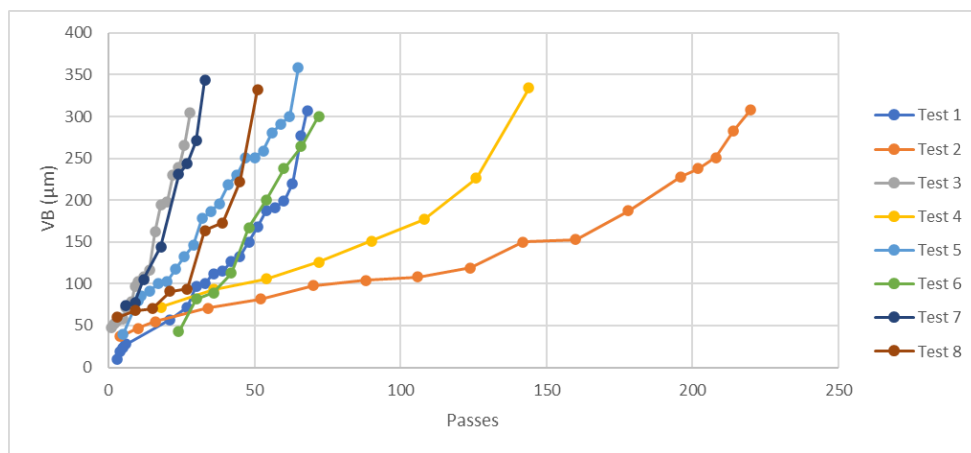


Fig 33. Chart showing wear development over time for eight test points.

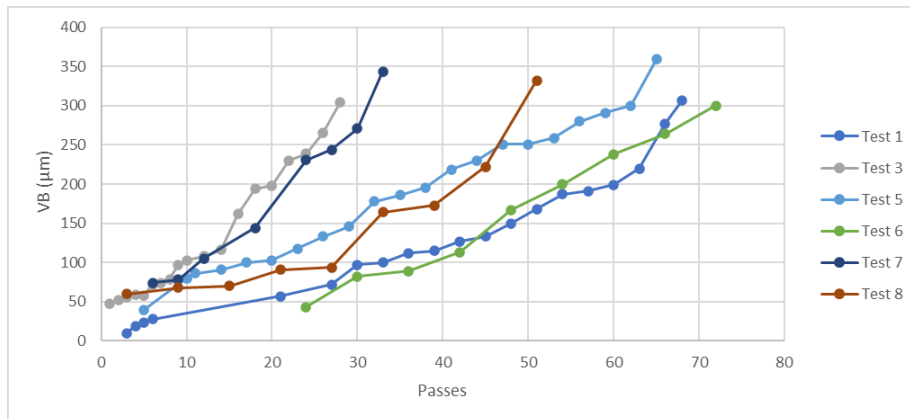


Fig 34. Chart showing wear development over time for points 1, 3, 5, 6, 7, and 8.

Test 1: VB=300 μm reached at pass 68 $f_z = 0.4 \text{ mm/rev}$ $v_c = 250 \text{ m/min}$			Test 2: VB=300 μm reached at pass 218 $f_z = 0.554 \text{ mm/rev}$ $v_c = 154 \text{ m/min}$		
Passes	VB (μm)	Volume (mm^3)	Passes	VB (μm)	Volume (mm^3)
3	10	30000	4	37	40000
4	19	40000	10	47	100000
5	23	50000	16	55	160000
6	28	60000	34	71	340000
21	57	210000	52	82	520000
27	72	270000	70	98	700000
30	97	300000	88	104	880000
33	100	330000	106	108	1060000
36	112	360000	124	119	1240000
39	115	390000	142	150	1420000
42	127	420000	160	153	1600000
45	133	450000	178	187	1780000
48	150	480000	196	228	1960000
51	168	510000	202	238	2020000
54	187	540000	208	251	2080000
57	191	570000	214	283	2140000
60	199	600000	220	308	2200000
63	220	630000			
66	277	660000			
68	307	680000			

Test 3: VB=300 μm reached at pass 28 $f_z = 0.277 \text{ mm/rev}$ $v_c = 431 \text{ m/min}$			Test 4: VB=300 μm reached at pass 138 $f_z = 0.277 \text{ mm/rev}$ $v_c = 185 \text{ m/min}$		
Passes	VB (μm)	Volume (mm^3)	Passes	VB (μm)	Volume (mm^3)
1	48	10000	18	72	180000
2	52	20000	36	93	360000
3	56	30000	54	106	540000
4	59	40000	72	126	720000
5	58	50000	90	151	900000
6	72	60000	108	177	1080000
7	74	70000	126	226	1260000
8	79	80000	144	334	1440000
9	97	90000			
10	103	100000			
12	108	120000			
14	116	140000			
16	162	160000			
18	194	180000			
20	198	200000			
22	230	220000			
24	239	240000			
26	266	260000			
28	305	280000			

Test 5: VB=300 μm reached at pass 62 $f_z = 0.554 \text{ mm/rev}$ $v_c = 359 \text{ m/min}$			Test 6: VB=300 μm reached at pass 72 $f_z = 0.554 \text{ mm/rev}$ $v_c = 250 \text{ m/min}$		
Passes	VB (μm)	Volume (mm^3)	Passes	VB (μm)	Volume (mm^3)
5	40	50000	24	43	240000
10	80	100000	30	82	300000
11	86	110000	36	89	360000
14	91	140000	42	113	420000
17	100	170000	48	167	480000
20	103	200000	54	200	540000
23	118	230000	60	238	600000
26	133	260000	66	264	660000
29	146	290000	72	300	720000
32	178	320000			
35	186	350000			
38	196	380000			
41	219	410000			
44	230	440000			
47	251	470000			
50	251	500000			
53	259	530000			
56	280	560000			
59	291	590000			
62	300	620000			
65	359	650000			

Test 7: VB=300 μm reached during pass 32 $f_z = 0.4 \text{ mm/rev}$ $v_c = 393 \text{ m/min}$			Test 8: VB=300 μm reached during pass 48 $f_z = 0.477 \text{ mm/rev}$ $v_c = 317 \text{ m/min}$		
Passes	VB (μm)	Volume (mm^3)	Passes	VB (μm)	Volume (mm^3)
6	74	60000	3	60	30000
9	78	90000	9	68	90000
12	105	120000	15	70	150000
18	144	180000	21	91	210000
24	231	240000	27	94	270000
27	244	270000	33	164	330000
30	271	300000	39	173	390000
33	344	330000	45	223	450000
			51	332	510000

5 Data Analysis and Discussion

In this section the experiments will be discussed and the resultant experimental data will be analysed.

5.1 Microscopy / Wear Development

The first test provides an example of some of the difficulties associated with measuring tool wear accurately, especially in the early phases, which will be briefly discussed here.

5.1.1 Problem 1: Establishing a measurement baseline

One of the most recurrent problems throughout this research was related to the establishment of a measurement baseline. In addition to the aforementioned complication due to edge radius needing to be measured together with VB [31], the recurrent adhesion and wear patterns made establishing a consistent baseline difficult. While this was mitigated mostly by including an area outside the area of maximum wear, as shown in Figure 35 below, it caused some uncertainty.

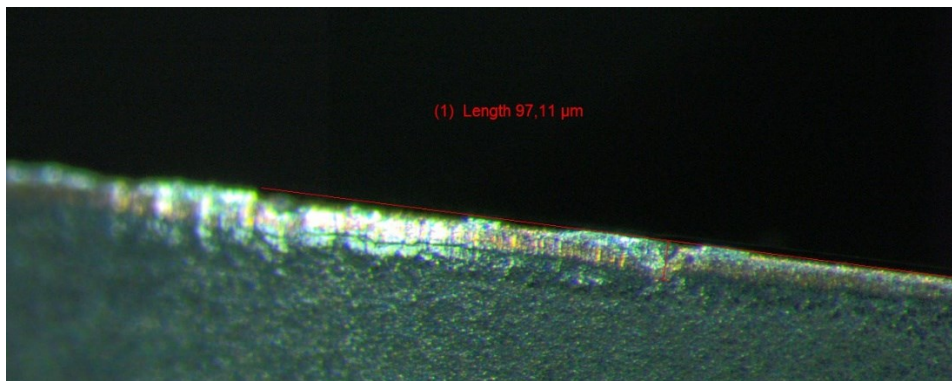


Fig 35. *Example image showing the selection of the baseline for wear measurement, Test 1 Pass 30 (cropped).*

5.1.2 Problem 2: Identifying the correct area

As wear was measured during this research between machining operations, the goal was to find the area of maximum tool wear to ascertain wear development. This was made difficult by the extremely short focal depth of the microscope, which together with the curvature of the insert made it only possible to observe a small section of the overall engagement area. This was especially a problem in early passes when the wear region was still stabilising. As it was unclear which area would end up with the most wear at the end, in some cases, consecutive images recorded different areas, with an example shown in Figure 36 below:

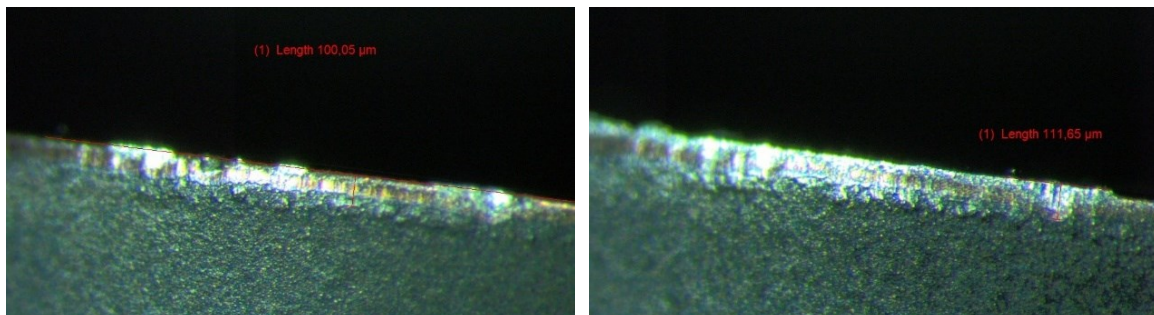


Fig 36. *Cropped images of pass 33 and 36 showing measurements in inconsistent areas.*

One possible way of dealing with this problem would be recording a larger area of the cutting edge, by either taking multiple images, or by using methods such as extended focus imaging (EFI), which creates a composite image of a larger focal depth. This way, it would be possible to adjust past measurements retroactively, which is not possible if the area of interest is out of focus. However, due to both time and equipment limitations, these methods were not possible to be used in this research.

5.1.3 Problem 3: Identifying wear

The third major problem encountered during microscopy was deciding whether a given optical change on the cutting edge was wear in the sense of the wear criterion. Especially with the inserts being multilayer-coated, the presence of several areas of different appearance made it difficult to determine at which exact point to measure wear. This being exacerbated by the adhesion layer making determining measurements difficult is a common problem [7].

While this was usually a smaller problem towards the wear criterion, in terms of determining the area of maximum wear, when stable regions of wear had formed, it nevertheless added uncertainty to measurements, as can be seen in Figure 37 below. If only the silvery region of adhered material is considered to be wear, the wear criterion is reached at or shortly before pass 68. If, however, the darker region below the adhered material is considered too, the wear criterion of $300\mu\text{m}$ is already reached in pass 66. As no solution to this problem was evident, it remained as a possible cause of error regarding VB measurements.

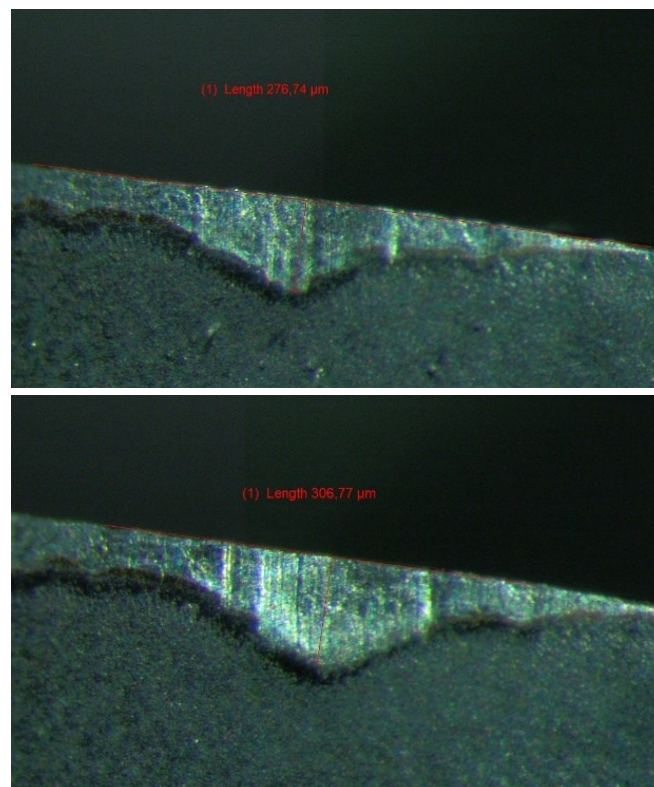


Fig 37. Passes 66 and 68 of Test 1 (cropped image), with a clear wear development, but an unclear length of maximum wear.

5.2 Evaluation of Machining Efficiency

As the economic effectiveness is one of the most central elements regarding decision making in machining, it is important to also compare the different cutting conditions in economic terms. The two fundamental elements in this case are material removal rate, MRR, and total volume removed, which are shown in Table 6 below.

Table 6. MRR and Total Volume Removed for the eight machining tests.

Test	MRR (mm ³ /min)	Total Volume Removed (mm ³)
Test 1	15915	675300
Test 2	13578	2180790
Test 3	19001	277400
Test 4	8156	1383000
Test 5	31654	620000
Test 6	22043	720000
Test 7	25019	320000
Test 8	24066	480000

For any given economic situation, MRR and total volume removed might be weighed differently, and a decision would be made based on what is preferred, which might either tend towards one of the two parameters, or to a balance. This can be showcased with a graph, as shown in Figure 38 below, which makes selection of the preferred cutting parameters easier.

Based on the diagram, some points, from an economic perspective, stand out as more or less efficient. In this case, Test 2, Test 6, and Test 5 are possible best cases. If MRR is prioritized, Test 5 might be chosen, conversely, if the total volume being removed is prioritized, Test 2 might be chosen instead, or alternatively Test 6 might be seen as a good balance. While other points might be chosen for reasons such as surface quality, they are from a purely economic perspective less effective, as for all five of them, there is an alternative cutting condition, at which both MRR and total volume removed is higher, for example Test 4 has both worse MRR, and total volume removed compared to Test 2.

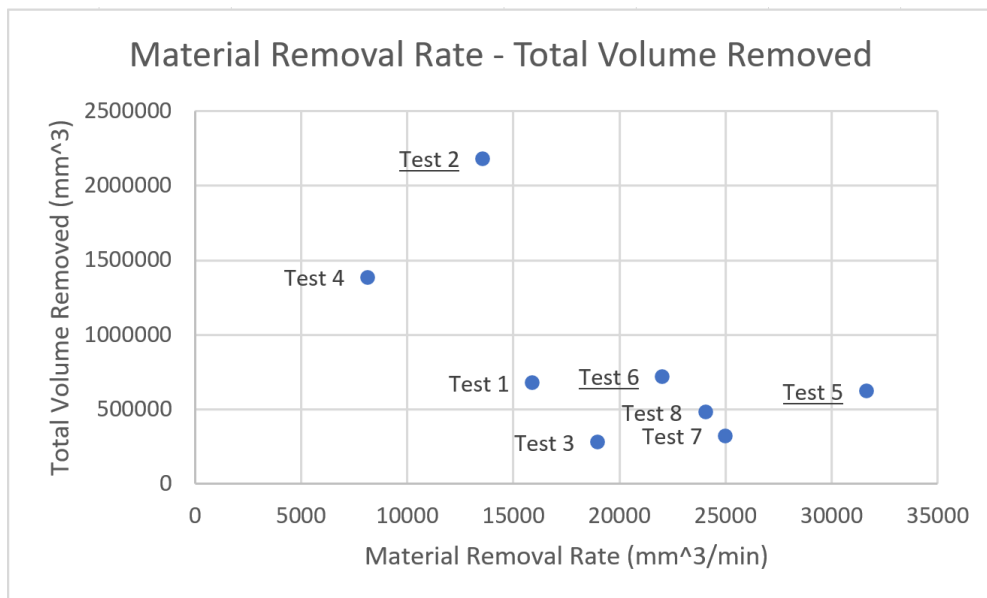


Fig 38. Diagram showing the eight machining tests, with ideal points underlined.

5.3 Colding Model

The central part of this research was to analyze the possibility of using a Colding model to predict tool life when milling cast iron with cemented carbide tools. This section will discuss the solution of the model based on the aforementioned methodology,

5.3.1 Non-real solutions

One problem that was encountered with the calculation of the Colding model was the finding of solutions that worked from a mathematical point of view, while not making physical sense. This will be shown here with such an example solution:

The numerical solution of the Colding model requires initial values to be given for a solution to be calculated. While these are arbitrary, and the method of finding good initial values that yielded a solution with low error was through iteration, it was often observed that replacing initial values with the final calculated value would lead to a better solution. Here it was however important to check if the values did lead to a real solution. In Figure 39 below, an example is shown of a solution with a low error, at 3.63%, where it can however be seen when plotting the Colding plane, that the solution is not real, in terms of the expected outcome of the model, the initial and final model constants of which are shown in Table 8 below. While the actual predictability of such a model is unclear, due to the implication of a combination of higher chip thickness and cutting speed improving tool life in a material where this has not been observed based on the experiments in this study, it can therefore be discarded as a purely mathematical, rather than physical solution of the Colding model. This kind of solution shows one of the underlying problems of the prediction model being based on statistical or mathematical approximation, which makes a clear understanding of the physical processes essential.

Table 7. Example values for Colding model without real solution.

	K	H	M	N0	L
Initial value (seeding)	7	-4	40	0.33	0.11
Final value (calculated)	6.3642	-2.1599	-0.7407	0.3235	0.0125

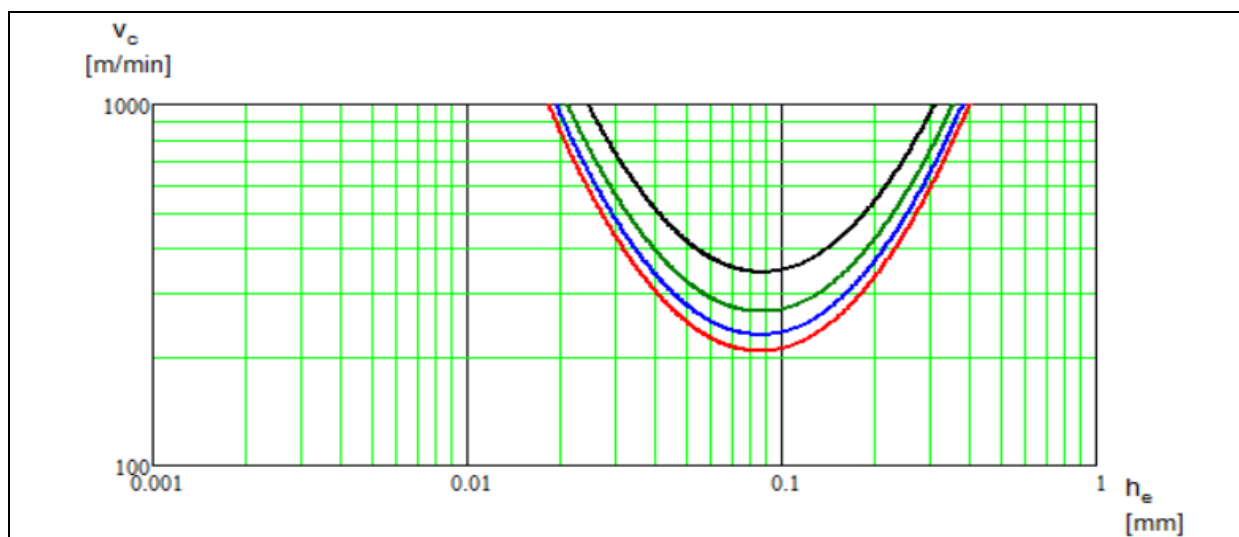


Fig 39. Colding planes for above-shown non-real solution where $a_p=1$, and $T= 5$ (black), 10 (green), 15 (blue), and 20 minutes (red) respectively.

5.3.2 Solution of the Colding Equation

When this problem associated with unrealistic resultant models was avoided, the following model constants were found as shown in Table 9 below. Using these constants, a model error of 4.49% was achieved.

Table 8. Colding Model Constants.

	K	H	M	N0	L
Initial value (seeding)	6.99	-2.8	3.9	0.4	0.01
Final value (calculated)	6.9362	-5.9326	5.5287	0.3184	0.0101

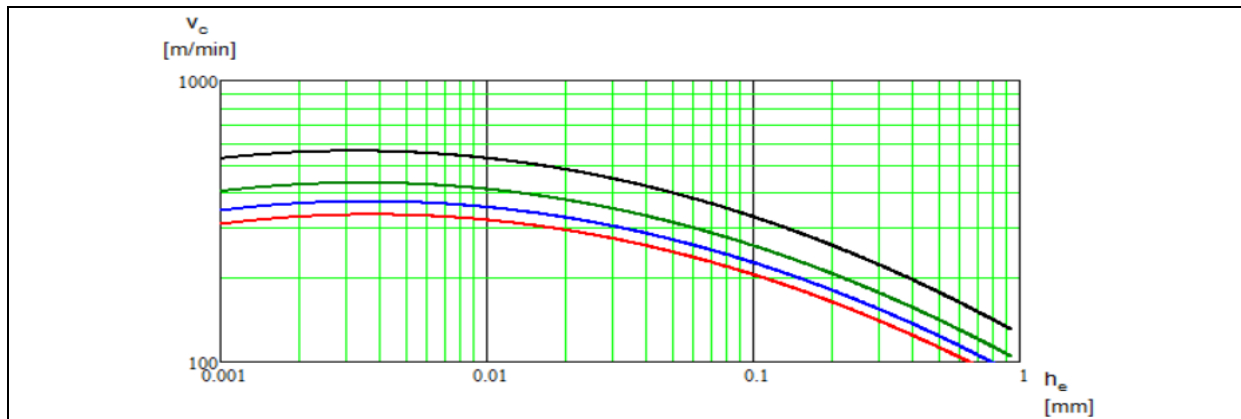


Fig 40. Colding planes for above solution where $a_p=1$, and $T= 5$ (black), 10 (green), 15 (blue), and 20 minutes (red) respectively.

When testing against the original data, by using tool life to calculate the corresponding cutting speed, the following individual errors, shown in Table 9 were found:

Table 9. Table showing model error for individual test points

Test	Test Point Error (%)
1	-6.28
2	-0.00597
3	2.06
4	2.93
5	11.9
6	-6.20
7	-3.06
8	-2.66

5.3.3 Subset Models

As a method of verification, and testing of the model, the tool life tests were planned such that they would allow the creation of Colding models using subsets of the data. As the Colding model is usually created from tests covering a parallelogram shape, as can be seen in Figure 41 below, by reusing Test 5 and Test 8, two smaller Colding models can be created, the results of which will be discussed here. The graphs showing the Colding planes for the subset tests are available in Appendix C.

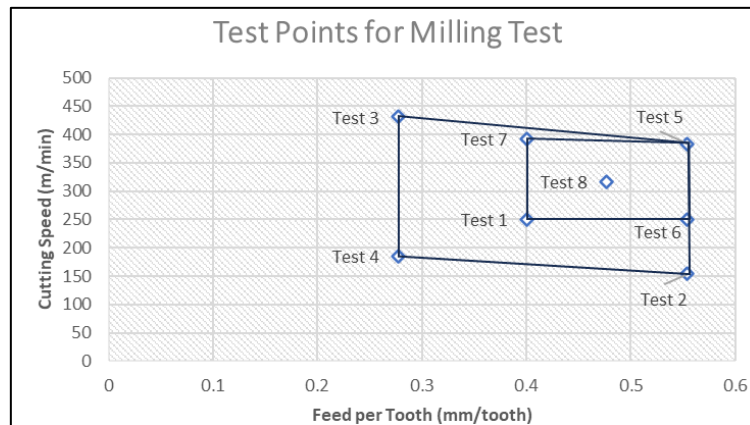


Fig 41. Distribution of the eight test points, with subsets of tests highlighted.

5.3.3.1 Subset 1: Inner Model

For the first test, the inner five points, i.e. Test 1, 6, 5, 7, and 8 were used to create a Colding equation based on which the outer points were tested. Reusing the previous method, the following, as shown in Table 10 was found:

Table 10. Colding Model Constants.

	K	H	M	N0	L
Initial value (seeding)	6	-2.8	3.9	0.4	0.01
Final value (calculated)	6.5691	-1.491	5.8644	0.5601	-0.0574

Using these constants, a model error of 4.41% was achieved. The created Colding model was then used to predict tool life for the three unused points:

Test point	Cutting speed at DCw v_c (m/min)	Feed per tooth f_z (mm/tooth)	Tool Life, actual (s)	Tool Life, modelled (s)	Error (%)
2	154	0.554	10444	7653	26.7
3	431	0.277	950	647	31.9
4	185	0.277	11021	5705	48.2

When testing against the test points, the following individual errors, shown in Table 11 were found:

Table 11. Table showing model error for individual test points.

Test	Test Point Error (%)
1	2.91
5	7.74
6	-6.45
7	-1.78
8	-2.94

5.3.3.2 Subset 2: Outer Model

For the first test, the outer five points, i.e. Test 2, 3, 4, 5, and 8 were used to create a Colding equation based on which the in points were tested. Reusing the previous method, the following was found, as shown in Table 12 below:

Table 12. Colding Model Constants.

	K	H	M	N0	L
Initial value (seeding)	6	-2.8	3.9	0.4	0.01
Final value (calculated)	6.5873	-4.4265	9.3798	0.4952	-0.0524

Using these constants, a model error of 3.18% was achieved. The created Colding model was then used to predict tool life for the three unused points:

Test point	Cutting speed at DCw v_c (m/min)	Feed per tooth f_z (mm/tooth)	Tool Life, actual (s)	Tool Life, modelled (s)	Error (%)
1	250	0.400	2754	3522	-27.9
6	250	0.554	2123	2862	-34.8
7	393	0.4	812	993	-22.3

When testing against the test points, the following individual errors, shown in Table 13 were found:

Table 13. Table showing model error for individual test points

Test	Test Point Error (%)
2	-0.11
3	1.9
4	0.3
5	5.7
8	-8.1

5.4 Colding Model Evaluation

In this study, the applicability of the Colding model, which is traditionally utilised for turning processes, within the realm of milling applications was investigated, specifically in regards to the machining of cast iron with cemented carbide inserts. Based on the empirical evidence, and the subsequent analysis of this data, the finding that a solution to the Colding model exists for milling, and that based on the model error of 4.49%, which can be compared to the mean error of 7.96% found by Kantojärvi et al. [10], it can be said that the Colding model is indeed adaptable for milling.

The occurrence of predictable wear patterns during the milling operations, mainly in form of abrasion of the flank edge with subsequent adhesion, made it possible to develop a model that predicts tool life within an acceptable margin of error, validating the models use case. This in turn means that machining operations with less predictable and more stochastic types of wear, such as chipping, might not follow the same patterns, and therefore require further analysis.

It should be noted however, that while the model error was found to be 4.5 %, the two subset tests, which had lower model errors, at 4.4 % and 3.2 % respectively, had, when tested against the remaining test points, higher errors, ranging between 22 % and 48 % percent were encountered, with the inner subset model underestimating tool life, and the outer subset model overestimating tool life. As it is

difficult to directly compare the two models, as they cover very different areas of the cutting speed and feed per tooth domains, this discrepancy cannot be attributed to any specific source.

5.5 Possible Causes of Error

In this section, possible causes of error will be discussed, which might have affected the outcomes of the machining tests during this research. Especially since the Colding model relies on standardised tests, in order to attribute changes in tool life to cutting speed and feed rates, the fact that some variable factors remained, which could not be eliminated from the experimental setup, might have had an unintended effect on the cutting conditions.

5.5.1 Changing workpiece geometry

The biggest such consideration was related to the changing geometry and size of the workpieces. As machining was done on standard blocks, which were used until the remaining thickness was too small for the clamping setup, some experiments required changing of the workpiece during a test, and tests did not always start with a complete block. This meant that if workpiece size influenced machining conditions, this effect would not be constant between operations.

Such effects might have been in form of vibrational, and thermal behaviour, i.e., as the machining caused considerable heat development, workpieces got hotter over time, which might have been amplified by smaller workpieces. Conversely, it is also possible that smaller workpieces which had a higher surface-to-volume ratio cooled down faster between passes. Furthermore, as machining was done with irregular times in between operations, in some operations, the workpiece might have been able to cool down, while in others it remained at an elevated temperature.

5.5.2 Changing machining environment

While machining was conducted under dry conditions, liquid chip collection was conducted at regular intervals during the machining, to prevent chip buildup. During this chip collection, unintentional misting and spraying of coolant was observable. In addition to this, especially during tests with higher MRR there might have been additional effects on the atmosphere within the machine, due to the evaporation caused by high temperature chips, and due to more regular chip collection.

5.5.3 Differences between passes

While the experiments were designed to have consistent passes as base units, some variance was nonetheless unavoidable. This came both in form of the first pass of each layer cutting a slightly different geometry, with the subsequent ones cutting into the area shaped by the tool radius, but also due to changes in material properties, which might have been both inherent to the workpiece from the casting process, but which also might have been caused by thermal and mechanical loads exerted onto the surface layer during previous layers.

5.5.4 Milling Insert number

The tests in this research were based on single insert machining, while using a tool made for six inserts tools. As studies have found that using fewer inserts can lead to longer tool life [28], and as the cutting data and expectations were based on numbers provided by Seco's cutting data based on 6-insert milling, the applicability of these numbers was not certain.

6 Conclusion

This thesis aimed to answer the following three main research questions:

Q1: To what extent is the Colding Model applicable in milling operations?

Q2: What are the factors affecting outcomes when milling CGI?

Q3: How do cemented carbide inserts behave when milling CGI?

Based on these, the underlying overall task was to gain a better understanding the applicability of the Colding model to predict tool life during the milling of compacted graphite iron.

In this regard, the research presented in this thesis has successfully demonstrated the applicability of the Colding tool model in predicting the tool life of cemented carbide cutting tools during the milling of compacted graphite iron (CGI). Through a series of milling experiments, this study has confirmed the effectiveness of the Colding model for tool life prediction in the unique context of milling and shed light on the behaviour of cemented carbide tools when machining CGI, finding for example that in this specific case, a high feed-rate may yield preferable results. The findings confirmed that with accurate tool life modelling, it is possible to identify optimal machining parameters that minimize tool wear and extend tool life, which has the potential of significantly enhancing process efficiency in industrial applications, especially by aiding better quality assurance, through a better understanding of tool wear. As a better understanding of processes in milling, also yields benefits in terms of better material utilization, this could be beneficial both in terms of cost reductions, but also in regards to environmental sustainability, as it would support resource efficient production, which further underscores the importance of selecting appropriate machining parameters to optimize tool life.

In conclusion, this research contributes to the body of knowledge in mechanical engineering by providing insights into the performance of cemented carbide cutting tools in milling CGI and highlighting the practical applicability of the Colding model in industrial machining processes, and process efficiency. This thesis not only proves the effectiveness of the Colding tool life model in a new application domain but also opens the door to further innovations in machining optimization, the benefits of which could be both in terms of cost, but also of environmental sustainability.

7 Future Research

The present study has provided insights into the validity of using the Colding model to predict tool life in milling operations. However, as the empirical data was based on outcomes of milling processes using round cemented-carbide inserts on compacted graphite iron (CGI) under dry conditions, several avenues remain to further confirm the validity of the model in other conditions, and with other materials. The following options are proposed to extend this research:

1. **cBN Tools:** Known for their exceptional hardness and suitability for high-speed machining, cBN tools represent a promising area for further investigation of the suitability of the Colding model.
2. **Ceramic Tools:** Similarly, ceramic tools already being employed to machine cast irons, are a promising area for further research of the Colding model.
3. **Other Types of Cast Iron:** Broadening the scope of materials to include different types of cast iron could help determine the Colding model's accuracy across a wider range of contexts.
4. **Other Material Classes:** Investigating the Colding model's effectiveness with materials beyond cast irons could offer a more comprehensive understanding of its applicability.
5. **Other Insert Shapes:** Examining how the Colding model performs with inserts of different shapes could provide insights into its versatility and potential limitations.
6. **Other Conditions:** Expanding the research to include different lubrication conditions, could help in understanding how these variables impact the Colding model's predictive accuracy.
7. **Further research on tool life equations:** Finally, While the Colding model provides an improvement in comparison to previous methods of tool life estimation, as the Colding model is not intended to model all region of cutting conditions and is not meant to model wear mechanisms that behave stochastically, its application might be limited in some use cases. As it was also originally developed for turning operations, even with the adaptations used in this research, the different mechanisms that occur during milling, such as the cutting edge experiencing repeated impacts and intermittent exposure to the air, might not be reflected by it. Therefore, the prospect of more specialised model that can more accurately reflect the wear mechanisms of milling operations should be investigated.

By addressing these areas, future studies can build on existing work to enhance the understanding of tool life prediction models and their applicability to a broader range of machining operations, materials, and conditions. This would not only validate the Colding model further but also contribute to the development of more efficient and cost-effective machining practices.

8 References

- [1] Cambridge University Press, “Definition of machining from the Cambridge Advanced Learner’s Dictionary & Thesaurus.” Mar. 13, 2024. Accessed: Mar. 19, 2024. [Online]. Available: <https://dictionary.cambridge.org/dictionary/english/machining>.
- [2] Google Books Ngram Viewer part of Google Research, “Google Books Ngram Viewer.” Accessed: Mar. 19, 2024. [Online]. Available: https://books.google.com/ngrams/graph?content=subtractive+manufacturing&year_start=1940&year_end=2014&corpus=en-2019&smoothing=0&case_insensitive=true.
- [3] “Electric vehicles,” IEA. Accessed: Jan. 21, 2024. [Online]. Available: <https://www.iea.org/energy-system/transport/electric-vehicles>
- [4] SinterCast AB, “SinterCast AB | Market Development.” Accessed: Jan. 21, 2024. [Online]. Available: <https://www.sintercast.com/market/market-development>.
- [5] D. Scott, “Europe’s electric truck market surges, while electric buses power ahead,” International Council on Clean Transportation. Accessed: Mar. 21, 2024. [Online]. Available: <https://theicct.org/europes-electric-truck-market-surges-aug23>.
- [6] “Volvo FH Electric wins ‘Truck of the Year 2024’ award.” Accessed: Jan. 21, 2024. [Online]. Available: <https://www.volvotrucks.com/en-en/news-stories/press-releases/2023/nov/volvo-fh-electric-wins-truck-of-the-year-2024-award.html>.
- [7] J.-E. Ståhl and P. De Vos, *Metal Cutting - Theories in Practice*. Lund, Fagersta: Seco Tools AB, 2014.
- [8] SinterCast AB, “Compacted Graphite Iron: A new material for highly stressed cylinder blocks and cylinder heads.” Accessed: Mar. 19, 2024. [Online]. Available: <https://www.sintercast.com/media/2287/compacted-graphite-iron-a-new-material-for-highly-stressed-cylinder-blocks-and-cylinder-heads.pdf>.
- [9] J. Niu *et al.*, “Study on surface integrity of compacted graphite iron milled by cemented carbide tools and ceramic tools,” *Int J Adv Manuf Technol*, vol. 103, no. 9, pp. 4123–4134, Aug. 2019, doi: 10.1007/s00170-019-03592-7.
- [10] F. Kantojärvi, E. Vikenadler, D. Johansson, S. Hägglund, and R. M’Saoubi, “Predicting tool life for side milling in C45 E using Colding and Taylor tool life models,” *Advances in Industrial and Manufacturing Engineering*, vol. 7, p. 100126, Nov. 2023, doi: 10.1016/j.aime.2023.100126.
- [11] ASM International, *ASM handbook. 15: Casting*. Materials Park, Ohio: ASM International, 2008.
- [12] R. Singh, “7 - Cast iron and cast steel,” in *Applied Welding Engineering (Third Edition)*, R. Singh, Ed., Butterworth-Heinemann, 2020, pp. 61–76. doi: 10.1016/B978-0-12-821348-3.00020-3.
- [13] R. Singh, “4 - Structure of materials,” in *Applied Welding Engineering (Third Edition)*, R. Singh, Ed., Butterworth-Heinemann, 2020, pp. 25–33. doi: 10.1016/B978-0-12-821348-3.00005-7.
- [14] S. Boonmee and D. M. Stefanescu, “Occurrence and effect of casting skin in compacted graphite iron,” *International Journal of Cast Metals Research*, vol. 29, no. 1–2, pp. 47–54, Mar. 2016, doi: 10.1179/1743133615Y.0000000017.
- [15] H. K. D. H. Bhadeshia and R. W. K. Honeycombe, “3 - Iron-carbon equilibrium and plain carbon steels,” in *Steels (Fifth Edition)*, H. K. D. H. Bhadeshia and R. W. K. Honeycombe, Eds., Butterworth-Heinemann, 2024, pp. 61–101. doi: 10.1016/B978-0-44-318491-8.00009-5.
- [16] D. S. Dawson and T. Schroeder, “Compacted Graphite Iron: A Viable Alternative.” SinterCast AB, 2000.
- [17] A. Sahm, E. Abele, and H. Schulz, “Machining of Compacted Graphite Iron (CGI),” *Materialwissenschaft und Werkstofftechnik*, vol. 33, no. 9, pp. 501–506, 2002, doi: 10.1002/1521-4052(200209)33:9<501::AID-MAWE501>3.0.CO;2-W.
- [18] D. M. Stefanescu *et al.*, “Volume 1A Cast Iron Science and Technology”.

- [19] ASTM International, “Standard Test Method for Evaluating the Microstructure of Graphite in Iron Castings.” Accessed: Jan. 25, 2024. [Online]. Available: <https://www.astm.org/a0247-19.html>
- [20] “Standard - Founding - Designation system for cast iron - Material symbols and material numbers SS-EN 1560:2011 - Swedish Institute for Standards, SIS,” Svenska institutet för standarder, SIS. Accessed: Jan. 25, 2024. [Online]. Available: <https://www.sis.se/en/produkter/metallurgy/ferrous-metals/irons/ssen15602011/>
- [21] M. König, “Literature review of microstructure formation in compacted graphite Iron,” *International Journal of Cast Metals Research*, vol. 23, no. 3, pp. 185–192, Jun. 2010, doi: 10.1179/136404609X12535244328378.
- [22] SinterCast AB, “Compacted Graphite Iron Material Datasheet.” Accessed: Sep. 12, 2023. [Online]. Available: <https://sintercast.com/media/1239/compacted-graphite-iron-material-datasheet.pdf>
- [23] B. Tasdelen, M. Escursell, G. Grenmyr, and L. Nyborg, “Machining of Gray Cast Irons and Compacted Graphite Iron,” 2007.
- [24] Y. Altintas, *Manufacturing Automation: Metal Cutting Mechanics, Machine Tool Vibrations, and CNC Design*. Cambridge University Press, 2012. doi: 10.1017/CBO9780511843723.
- [25] AB Sandvik Coromant, *Modern Metal Cutting: a Practical Handbook*. Sandviken: Sandvik Coromant, 1994.
- [26] L. Norberto López de Lacalle, F. J. Campa, and A. Lamikiz, “3 - Milling,” in *Modern Machining Technology*, J. Paulo Davim, Ed., Woodhead Publishing, 2011, pp. 213–303. doi: 10.1533/9780857094940.213.
- [27] Seco Tools AB, “Milling | Secotools.com.” Accessed: Jan. 24, 2024. [Online]. Available: <https://www.secotools.com/article/67146>.
- [28] A. Richetti, Á. R. Machado, M. B. Da Silva, E. O. Ezugwu, and J. Bonney, “Influence of the number of inserts for tool life evaluation in face milling of steels,” *International Journal of Machine Tools and Manufacture*, vol. 44, no. 7, pp. 695–700, Jun. 2004, doi: 10.1016/j.ijmachtools.2004.02.007.
- [29] S. C. Black, V. Chiles, A. J. Lissaman, and S. J. Martin, “11 - Turning and Milling,” in *Principles of Engineering Manufacture (Third Edition)*, S. C. Black, V. Chiles, A. J. Lissaman, and S. J. Martin, Eds., Oxford: Butterworth-Heinemann, 1996, pp. 316–371. doi: 10.1016/B978-034063195-9/50042-0.
- [30] “Machinepark | Matrijzen & Vormenbouw Haaksbergen.” Accessed: Jan. 24, 2024. [Online]. Available: <https://www.mvhaaksbergen.nl/machinepark/>
- [31] J.-E. Ståhl and Seco Tools AB, *Metal Cutting: Theories and Models*. Division of Production and Materials Engineering, 2012.
- [32] W. Zhang, Y. M. Chong, B. He, I. Bello, and S.-T. Lee, “3.24 - Cubic Boron Nitride Films: Properties and Applications,” in *Comprehensive Hard Materials*, V. K. Sarin, Ed., Oxford: Elsevier, 2014, pp. 607–639. doi: 10.1016/B978-0-08-096527-7.00061-1.
- [33] P. Wang and R. X. Gao, “Stochastic Tool Wear Prediction for Sustainable Manufacturing,” *Procedia CIRP*, vol. 48, pp. 236–241, Jan. 2016, doi: 10.1016/j.procir.2016.03.101.
- [34] J.-E. Ståhl and M. Andersson, “Polar machinability diagrams—a model to predict the machinability of a work material,” in *Sweden production symposium. Göteborg*, 2007. Accessed: Dec. 16, 2023. [Online]. Available: https://portal.research.lu.se/files/61814689/Polar_machinability_diagrams.pdf.
- [35] J.-E. Ståhl, “An Integrated Cost Model for Metal Cutting Operations Based on Engagement Time and a Cost Breakdown Approach,” *International Journal of Manufacturing Research*, vol. 12, no. 4, pp. 379–404, 2017, doi: 10.1504/IJMR.2017.088397.

- [36] D. Johansson *et al.*, “Assessment of Metal Cutting Tools using Cost Performance Ratio and Tool Life Analyses,” *Procedia Manufacturing*, vol. 38, pp. 816–823, Jan. 2019, doi: 10.1016/j.promfg.2020.01.114.
- [37] D. Johansson, “Tool Life and Cutting Data Modelling in Metal Cutting: Testing, Modelling and Cost Performance,” Doctoral Thesis (compilation), Department of Mechanical Engineering, Lund University, 2019.
- [38] F. W. Taylor, *On the art of cutting metals*, vol. 23. American society of mechanical engineers, 1906.
- [39] B. N. Colding, “The Machining Productivity Mountain and Its Wall of Optimum Productivity,” presented at the 9th NAMRAC, 1981, pp. 37–42.
- [40] D. Johansson, S. Hägglund, V. Bushlya, and J.-E. Ståhl, “Assessment of Commonly used Tool Life Models in Metal Cutting,” *Procedia Manufacturing*, vol. 11, pp. 602–609, Jan. 2017, doi: 10.1016/j.promfg.2017.07.154.
- [41] S. Hägglund, “Methods and Models for Cutting Data Optimization,” Chalmers University of Technology, 2013. Accessed: Mar. 22, 2024. [Online]. Available: <https://research.chalmers.se/en/publication/173305>
- [42] Seco Tools AB, “RPKW1204M0T-6-MD10 MK2050 | Secotools.com.” Accessed: Mar. 18, 2024. [Online]. Available: https://www.secotools.com/article/p_02923731
- [43] Seco Tools AB, “Discover the Material groups | Secotools.com.” Accessed: Mar. 18, 2024. [Online]. Available: <https://www.secotools.com/article/118837>
- [44] “A Guide to Milling Grades, Materials and Solutions | Secotools.com.” Accessed: Mar. 18, 2024. [Online]. Available: <https://www.secotools.com/article/123778>
- [45] Seco Tools AB, “R220.29I-0080-06.6A | Secotools.com.” Accessed: Mar. 18, 2024. [Online]. Available: https://www.secotools.com/article/p_02949625
- [46] “Specialised Research Equipment,” Division of Production and Materials Engineering. Accessed: Mar. 22, 2024. [Online]. Available: <https://www.iprod.lth.se/english/infrastructure/specialized-research-equipment/>
- [47] R. Woxén, *A Theory and an Equation for the Life of Lathe Tools*. Central Tryckeriet, 1932.
- [48] K. Levenberg, “A method for the solution of certain non-linear problems in least squares,” *Quart. Appl. Math.*, vol. 2, no. 2, pp. 164–168, 1944, doi: 10.1090/qam/10666.
- [49] D. W. Marquardt, “An Algorithm for Least-Squares Estimation of Nonlinear Parameters,” *Journal of the Society for Industrial and Applied Mathematics*, vol. 11, no. 2, pp. 431–441, Jun. 1963, doi: 10.1137/0111030.

Appendix A: Nanoindentation Data

A.1 Gray Cast Iron / Lamellar Graphite Iron (LGI)

Point Layer	#1	#2	#3	#4	#5	#6	#7	#8	#9	#10	Average
1	4.46	5.14	4.51	4.60	4.14	4.11	3.49	4.94	4.51	4.73	4.46
2	4.24	4.55	5.06	4.17	4.66	4.94	3.68	3.73	4.06	3.99	4.31
3	4.85	4.26	4.18	4.34	4.22	3.89	4.78	3.48	4.74	3.66	4.24
4	3.54	4.33	4.62	3.01	4.16	5.15	4.53	4.81	4.41	3.34	4.19
5	2.97	4.40	3.89	4.11	3.60	3.51	3.02	2.89	4.64	2.41	3.54
6	3.74	4.12	4.54	3.88	4.14	4.34	4.52	3.89	4.39	4.93	4.25
7	4.09	2.97	3.80	3.46	4.57	2.50	2.95	3.12	2.60	2.49	3.26
8	4.57	4.40	3.69	3.48	4.60	2.65	3.92	4.19	3.36	3.38	3.82
9	3.38	4.35	4.90	0.78	4.03	4.48	3.22	5.13	4.40	2.62	3.73
10	2.46	4.82	2.40	4.19	4.98	4.94	4.64	1.86	1.81	3.07	3.51
11	1.82	3.66	2.46	3.59	4.63	0.96	2.62	3.43	1.30	3.08	2.75
12	4.69	0.24	0.10	4.61	3.44	4.52	2.18	4.27	4.85	4.04	3.29
13	4.36	4.49	0.05	1.16	1.99	2.66	3.51	3.82	2.63	4.60	2.93
14	3.29	3.29	2.75	3.91	4.70	4.29	4.41	4.76	3.73	2.70	3.78
15	5.29	4.92	2.32	2.51	4.97	3.12	3.23	4.94	2.70	4.45	3.84
16	5.65	4.12	2.94	4.53	5.15	5.26	4.67	4.96	4.72	2.87	4.49
17	3.96	5.25	1.55	4.83	4.64	4.75	4.83	2.71	5.10	5.01	4.26
18	2.91	2.30	4.66	3.96	4.77	4.32	4.41	4.05	2.74	5.13	3.92
19	4.57	4.06	4.77	4.05	3.87	3.01	3.46	1.65	1.72	2.66	3.38
20	1.18	4.32	4.20	2.83	3.96	2.65	2.13	1.99	3.66	1.66	2.86

A.2 Compacted Graphite Iron (CGI450)*

Point Layer	#1	#2	#3	#4	#5	#6	#7	#8	#9	#10	Average
1	4.40	4.04	3.46	3.17	3.45	4.06	3.57	3.70	4.30	4.31	3.85
2	3.71	6.59	2.70	3.36	4.13	5.72	3.62	4.40	3.59	3.55	4.14
3	3.81	3.21	5.85	0.90	3.84	3.36	3.91	4.71	4.07	4.09	3.77
4	5.59	3.46	5.54	3.83	4.02	3.77	<i>NaN</i>	4.75	3.42	4.49	4.32
5	4.64	5.64	3.53	3.59	2.99	3.16	5.88	5.50	3.62	3.38	4.19
6	3.32	3.90	3.12	4.89	3.99	2.97	3.55	3.98	3.29	4.50	3.75
7	2.34	0.98	3.01	2.05	1.23	2.58	2.76	3.41	3.23	3.43	2.50
8	3.04	3.39	2.63	3.10	1.27	2.83	0.52	1.69	2.34	1.44	2.22
9	3.08	1.54	1.39	1.51	1.69	1.18	3.52	1.41	2.12	2.27	1.97
10	1.62	2.53	3.71	2.13	3.47	1.53	2.62	3.28	2.77	1.86	2.55
11	1.58	2.73	1.55	2.79	1.87	2.50	3.78	1.96	2.90	4.82	2.65
12	3.34	0.99	1.99	1.09	4.44	1.51	1.93	2.67	4.63	5.20	2.78
13	4.53	3.26	4.72	4.44	3.04	4.54	2.72	1.45	1.68	4.83	3.52
14	4.48	3.65	4.36	3.06	4.49	4.64	1.04	2.40	4.11	3.51	3.58
15	2.25	2.91	4.34	4.31	5.72	0.69	1.30	2.02	4.60	4.90	3.30
16	2.69	1.94	4.19	1.97	2.72	3.92	1.51	3.99	4.43	4.98	3.23
17	4.23	3.01	4.95	4.54	3.20	4.05	4.49	4.21	4.59	4.51	4.18
18	2.91	2.68	3.45	2.19	4.31	3.11	3.78	4.37	3.10	5.00	3.49
19	2.35	4.29	4.52	4.55	1.88	3.08	4.14	4.43	4.19	4.38	3.78
20	3.70	4.17	3.87	2.54	4.54	4.37	5.00	4.86	5.03	4.61	4.27

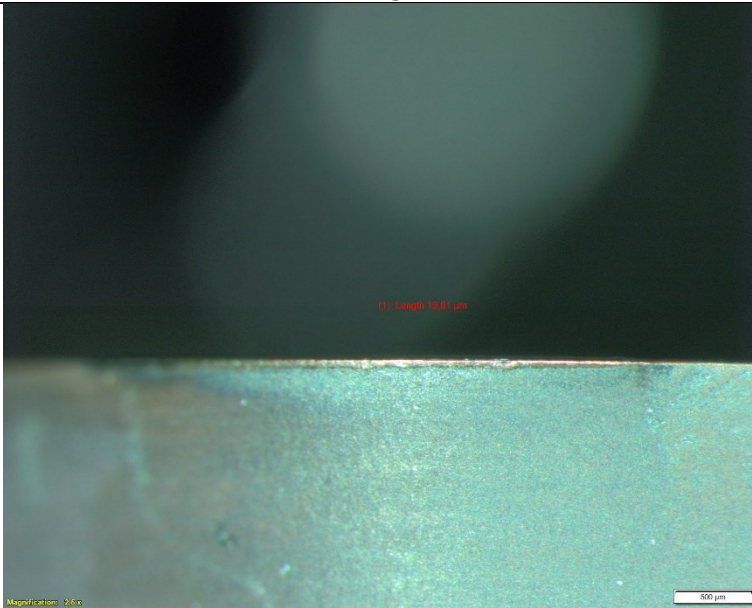
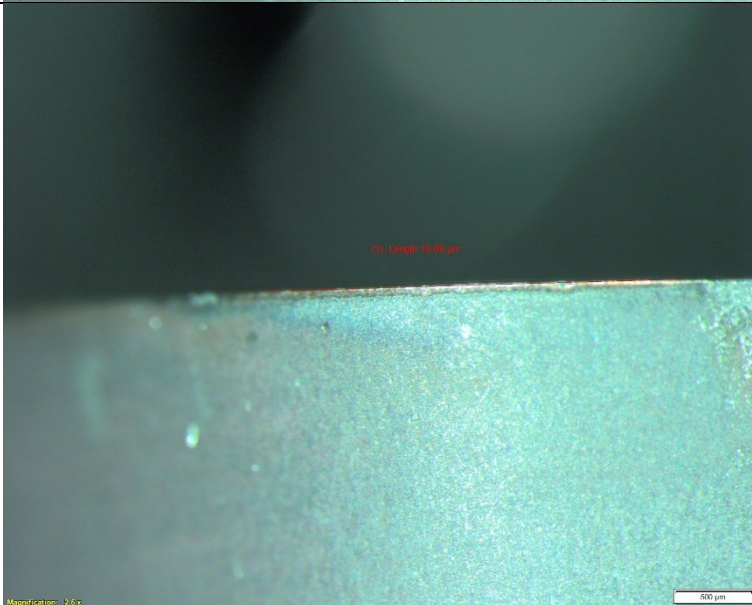
A.3 Compacted Graphite Iron (CGI350/SSF)


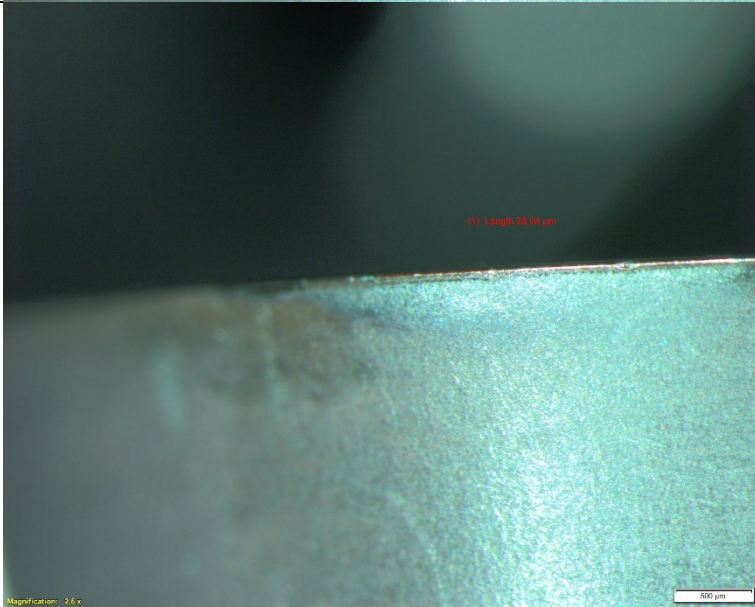
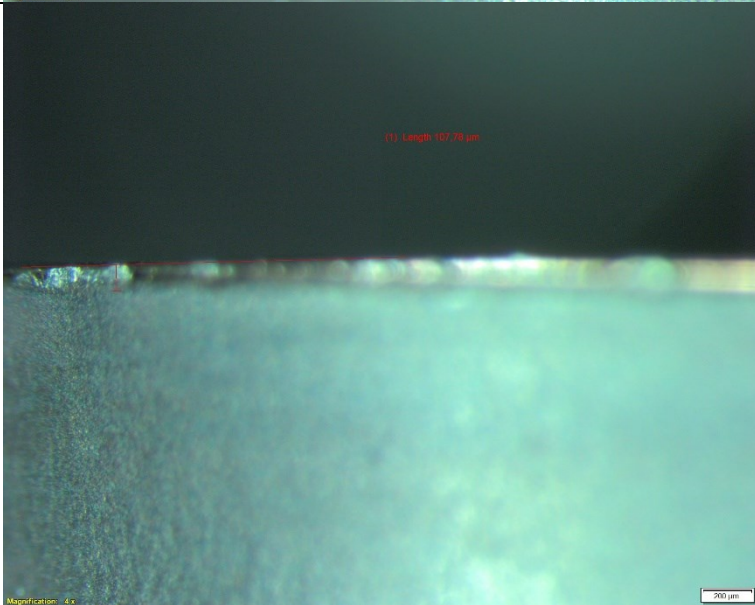
Point Layer	#1	#2	#3	#4	#5	#6	#7	#8	#9	#10	Average
1	6.11	5.01	5.07	4.69	4.75	4.29	4.89	4.17	4.50	5.25	4.87
2	4.17	4.55	5.31	4.47	4.75	4.44	6.08	4.18	4.74	5.26	4.8
3	4.60	4.71	4.81	4.47	4.01	4.28	4.43	4.30	4.34	4.92	4.49
4	9.78	4.10	4.15	4.57	6.35	3.43	4.14	6.41	4.09	4.55	5.16
5	4.84	5.05	4.23	4.33	4.98	4.21	4.23	5.43	4.52	4.17	4.6
6	4.36	3.89	6.36	3.92	4.64	4.02	4.06	7.91	7.22	3.75	5.01
7	3.39	3.97	3.93	3.96	3.91	3.88	3.50	4.19	3.46	6.51	4.07
8	1.94	3.95	4.27	4.45	3.70	3.33	3.76	4.03	4.37	1.17	3.5
9	0.98	2.35	3.25	1.82	2.68	3.00	3.76	3.36	1.64	1.74	2.46
10	3.34	1.35	3.57	4.14	1.91	0.77	4.31	4.21	3.58	3.99	3.12
11	2.67	0.84	4.13	1.42	2.26	2.26	2.20	2.74	1.71	3.69	2.39
12	0.70	1.49	4.17	2.10	3.85	1.69	1.30	2.37	2.25	1.65	2.16
13	3.14	2.62	3.11	1.86	2.00	3.08	1.74	1.83	0.81	0.83	2.1
14	1.94	0.89	0.94	0.40	0.69	0.76	0.95	1.21	0.72	0.67	0.92
15	0.93	1.08	0.88	1.06	1.24	0.84	1.00	0.99	0.69	0.96	0.97
16	0.72	0.80	0.60	1.15	0.78	0.84	0.59	0.64	0.77	0.61	0.75
17	0.78	0.59	0.70	0.63	0.90	0.72	0.60	0.78	0.29	0.66	0.67
18	0.83	0.75	0.62	0.77	0.98	0.30	0.96	0.58	0.51	0.63	0.7
19	0.63	0.69	1.20	0.47	0.45	0.69	0.65	0.39	0.85	0.66	0.67
20	0.55	0.62	0.45	0.36	0.50	0.57	0.29	0.61	0.65	0.76	0.54


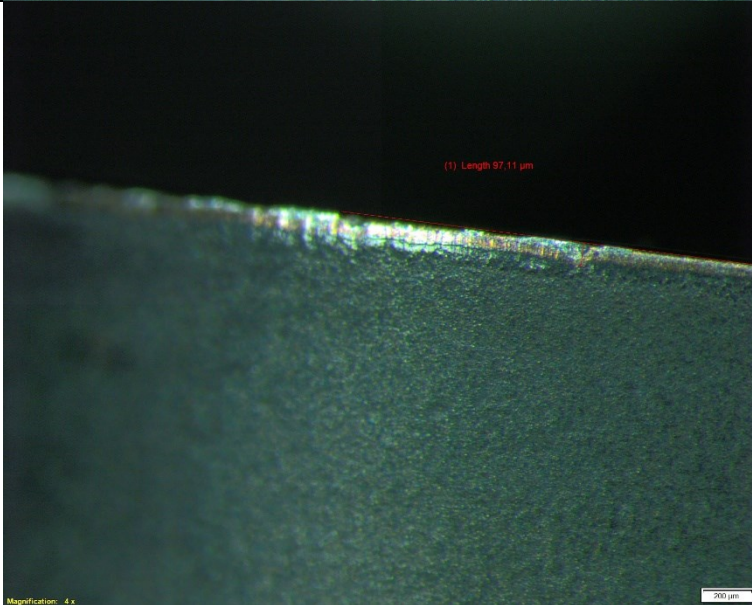
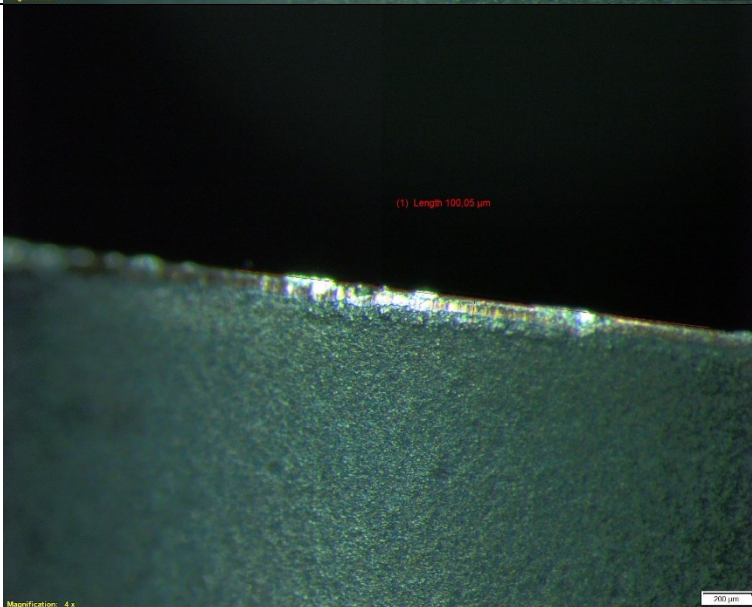
*: The Not-A-Number (NaN) result in Layer 4 – Point #4 of the CGI450 test was ignored while calculating the average value of that layer.

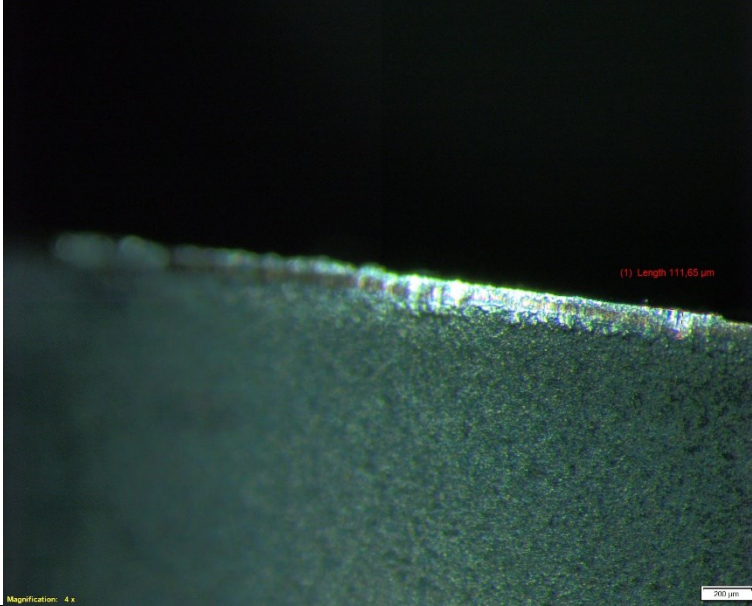
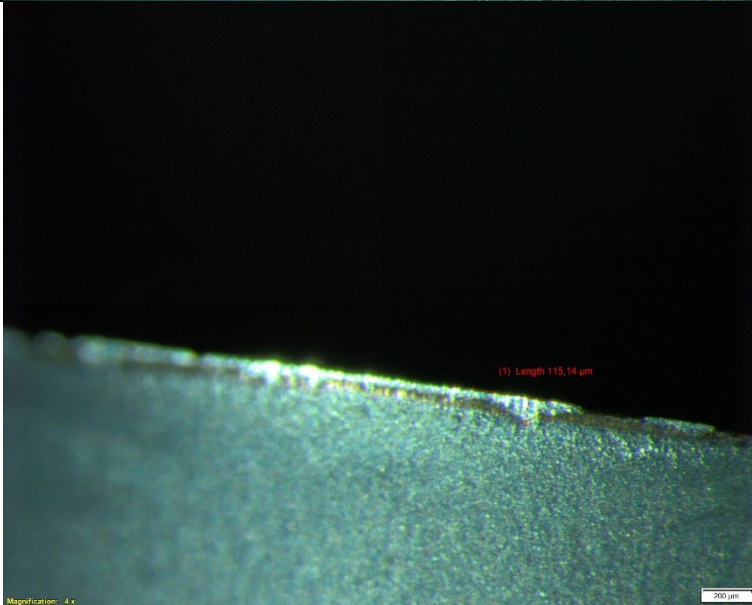
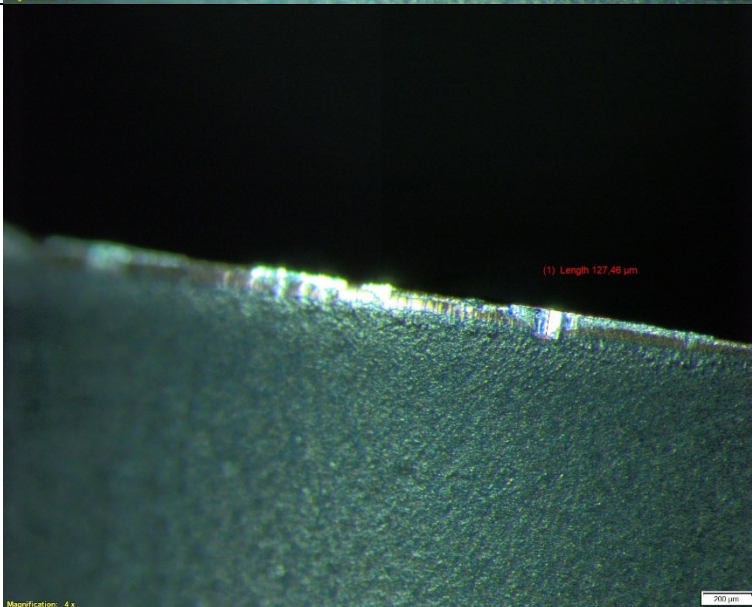
Appendix B: Microscopy

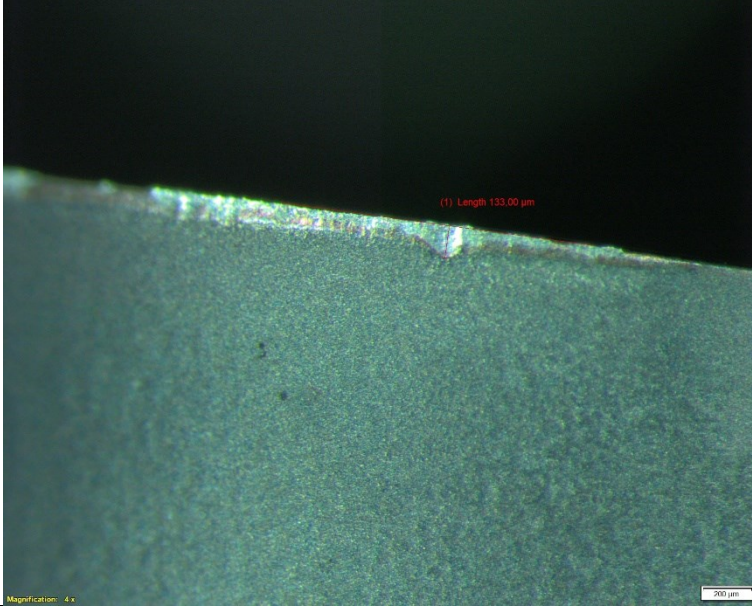
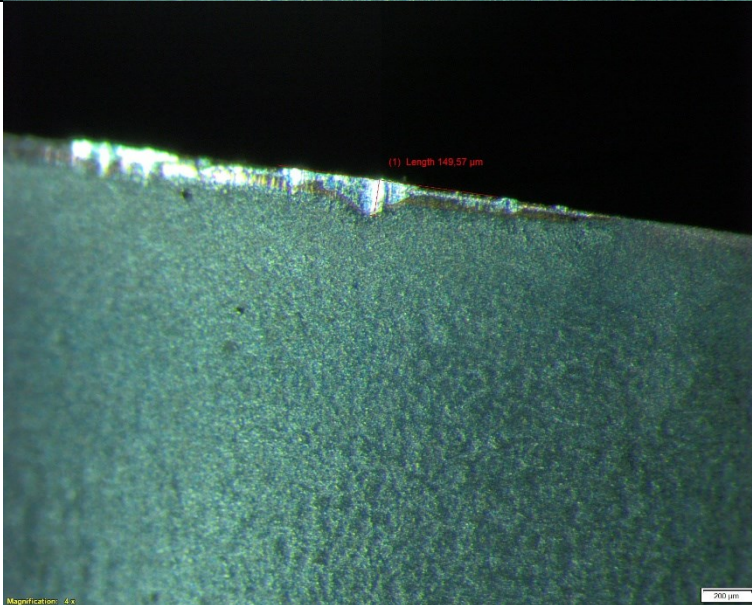
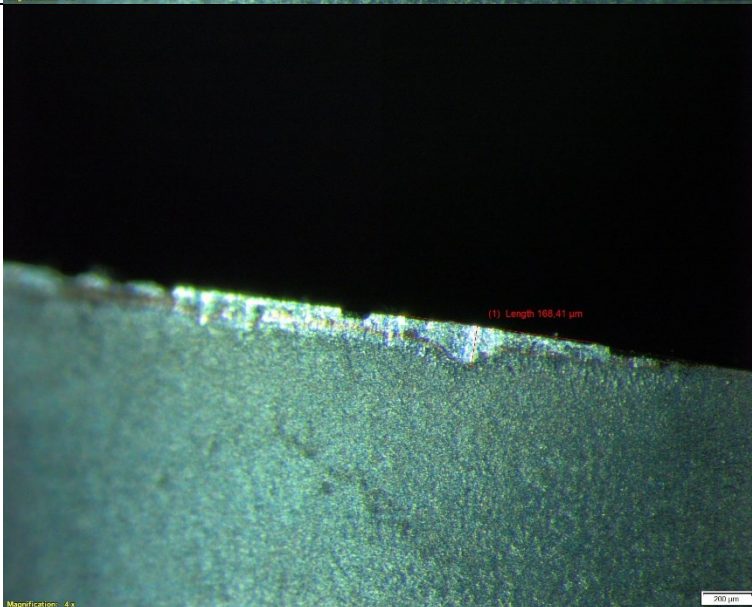
B.1 Images for Test 1:

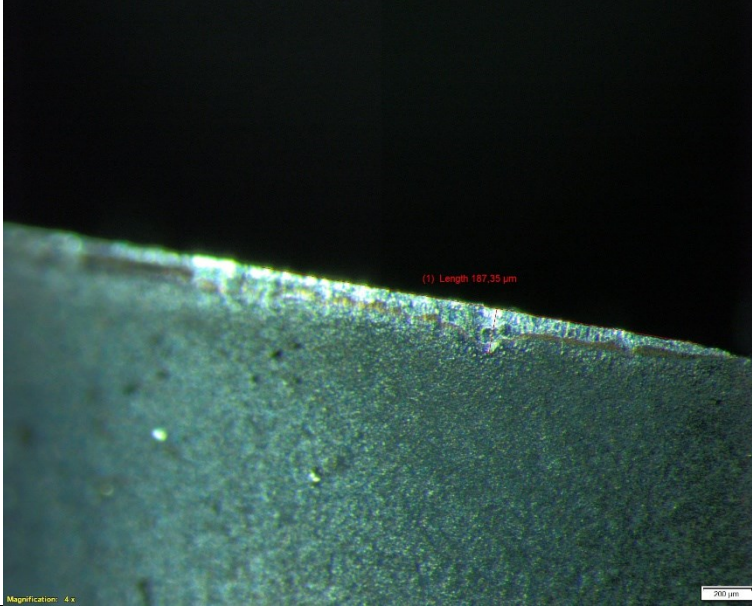
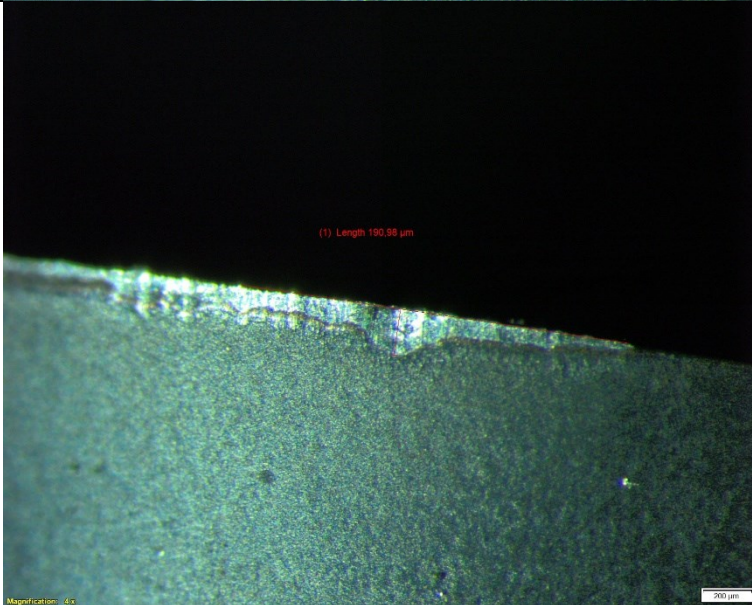
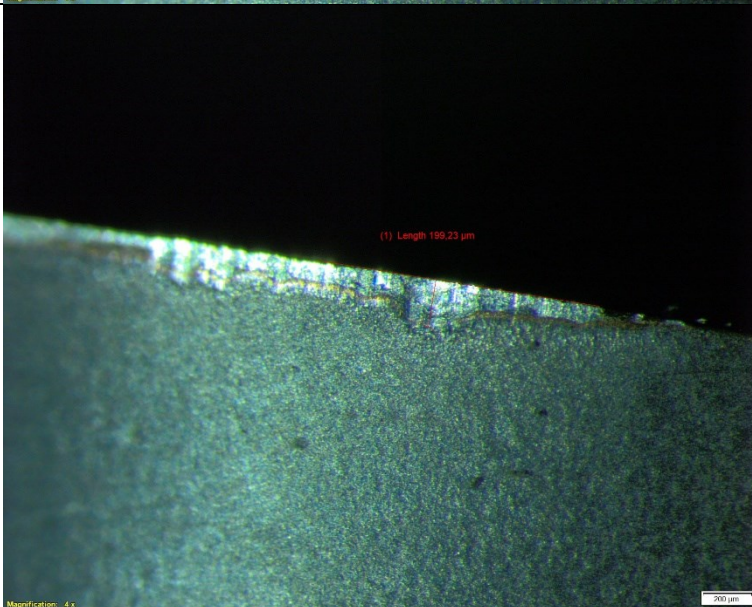
Pass #	Image
3	 <p data-bbox="852 680 943 696">(1) Length: 10.81 μm</p> <p data-bbox="480 981 555 992">Magnification: 26x</p> <p data-bbox="1171 974 1225 985">500 μm</p>
4	 <p data-bbox="852 1234 943 1249">(1) Length: 10.08 μm</p> <p data-bbox="480 1585 555 1597">Magnification: 26x</p> <p data-bbox="1171 1579 1225 1590">500 μm</p>

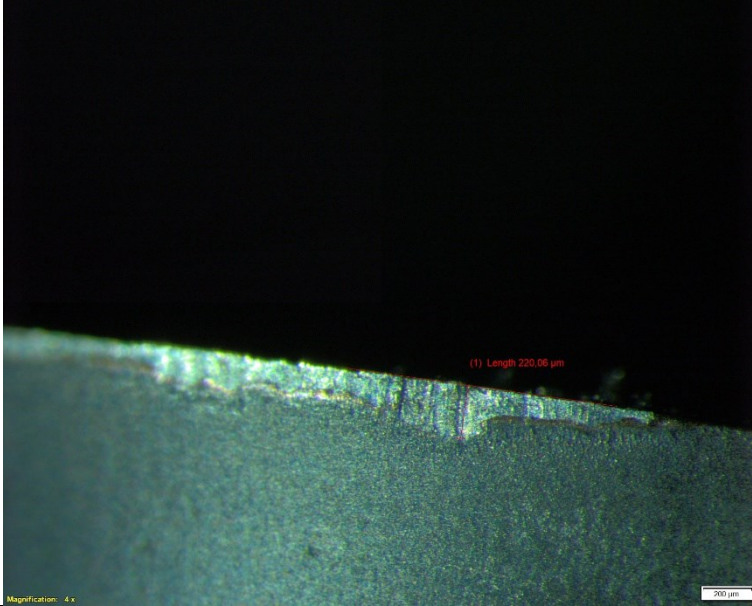
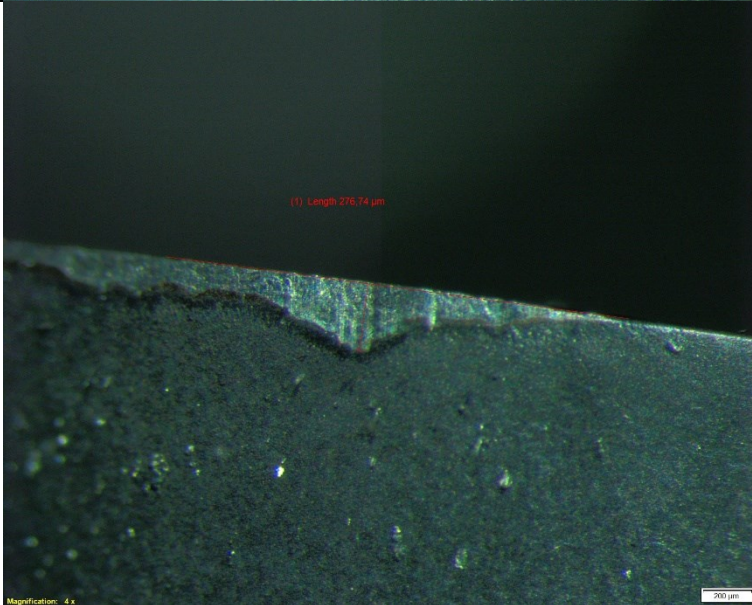
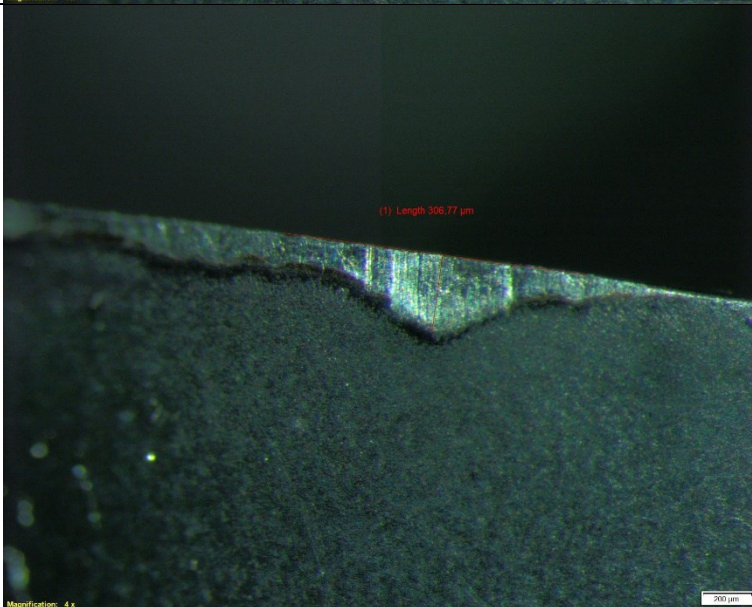
5	 <p>(1) Length: 23.38 μm</p> <p>Magnification: 2.6x</p> <p>500 μm</p>
6	 <p>(1) Length: 25.94 μm</p> <p>Magnification: 2.6x</p> <p>500 μm</p>
21	 <p>(1) Length: 107.78 μm</p> <p>Magnification: 4x</p> <p>200 μm</p>

27	 <p>(1) Length 72.25 μm</p> <p>Magnification: 4 x</p> <p>200 μm</p>
30	 <p>(1) Length 97.11 μm</p> <p>Magnification: 4 x</p> <p>200 μm</p>
33	 <p>(1) Length 100.05 μm</p> <p>Magnification: 4 x</p> <p>200 μm</p>

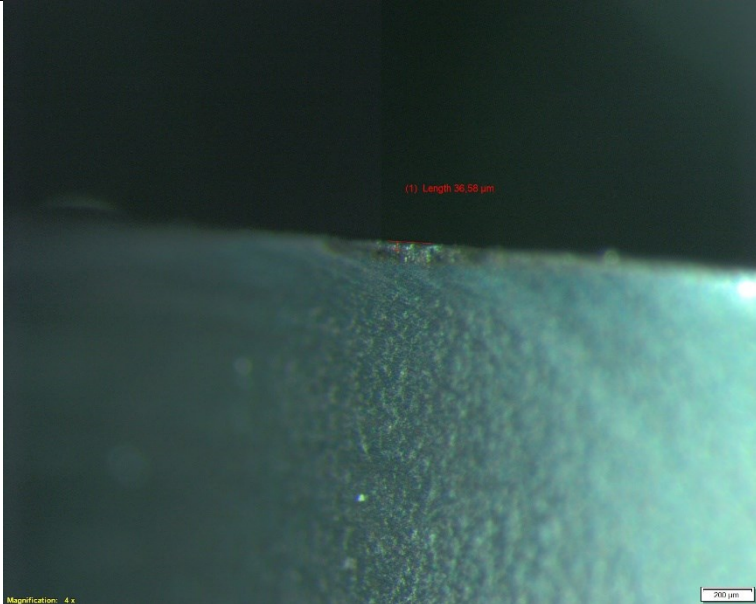
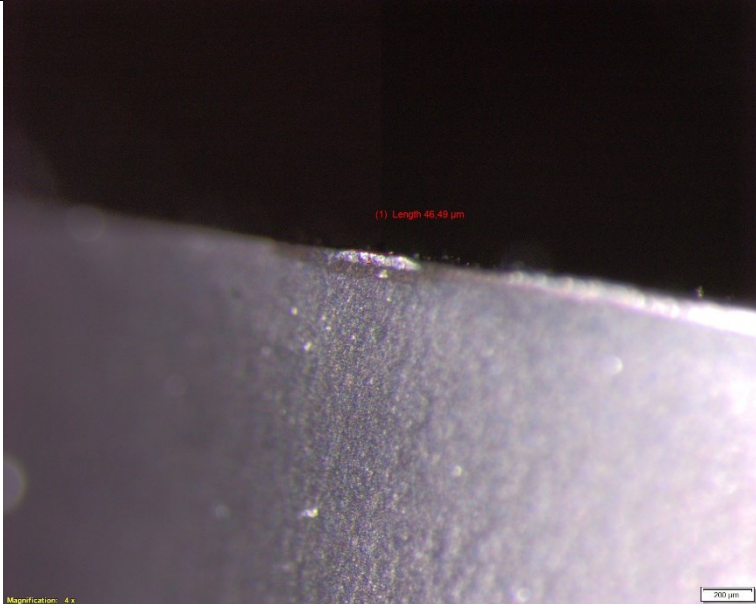
36	 <p>(1) Length 111.65 μm</p> <p>Magnification: 4 x</p> <p>200 μm</p>
39	 <p>(1) Length 113.14 μm</p> <p>Magnification: 4 x</p> <p>200 μm</p>
42	 <p>(1) Length 127.46 μm</p> <p>Magnification: 4 x</p> <p>200 μm</p>

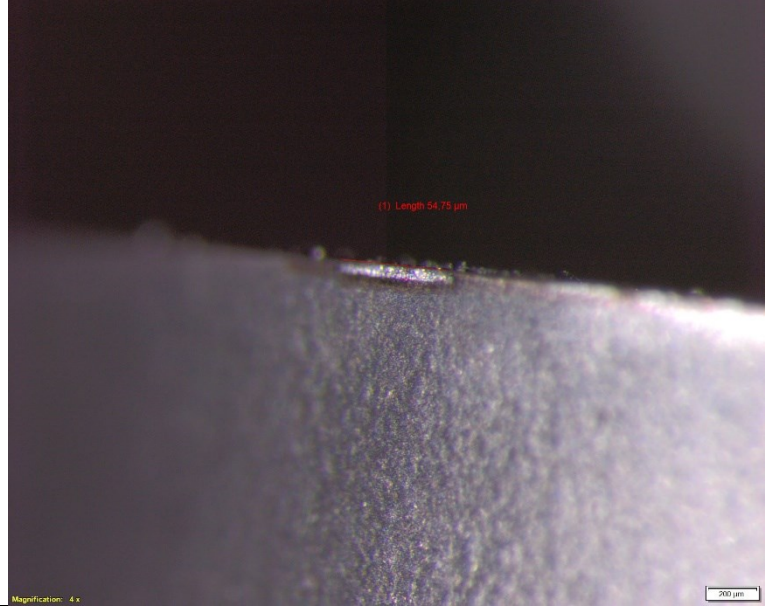
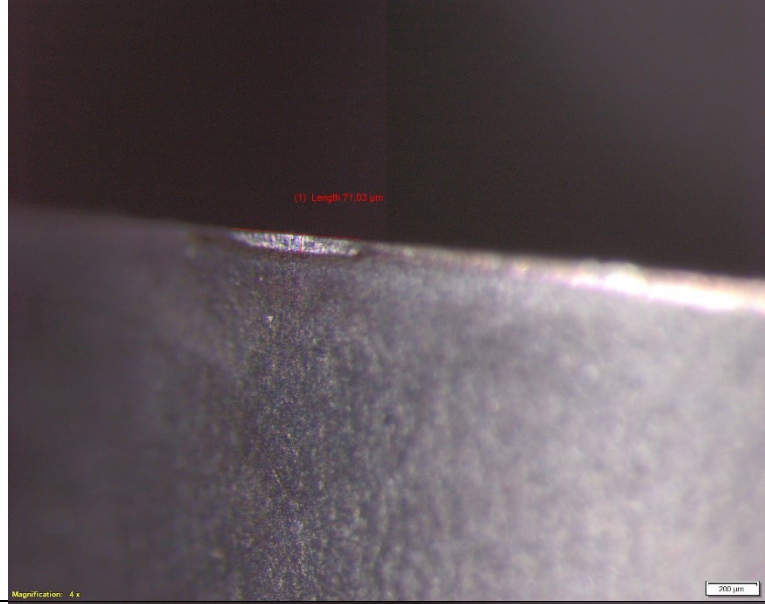
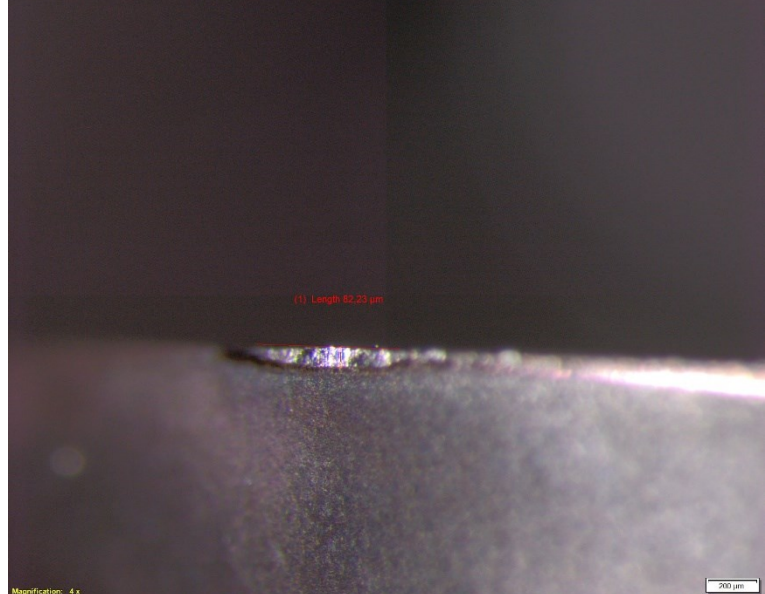
45	 <p>(1) Length 133.00 μm</p> <p>Magnification: 4x</p> <p>200 μm</p>
48	 <p>(1) Length 149.57 μm</p> <p>Magnification: 4x</p> <p>200 μm</p>
51	 <p>(1) Length 168.41 μm</p> <p>Magnification: 4x</p> <p>200 μm</p>

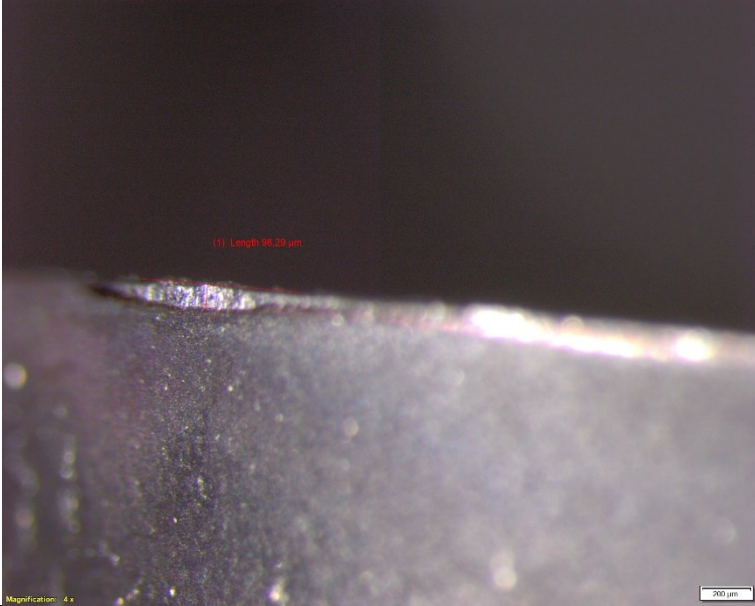
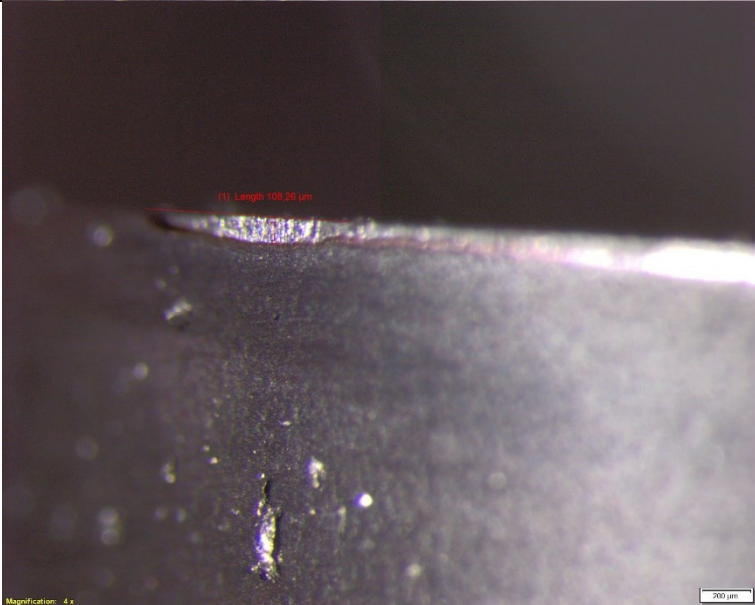
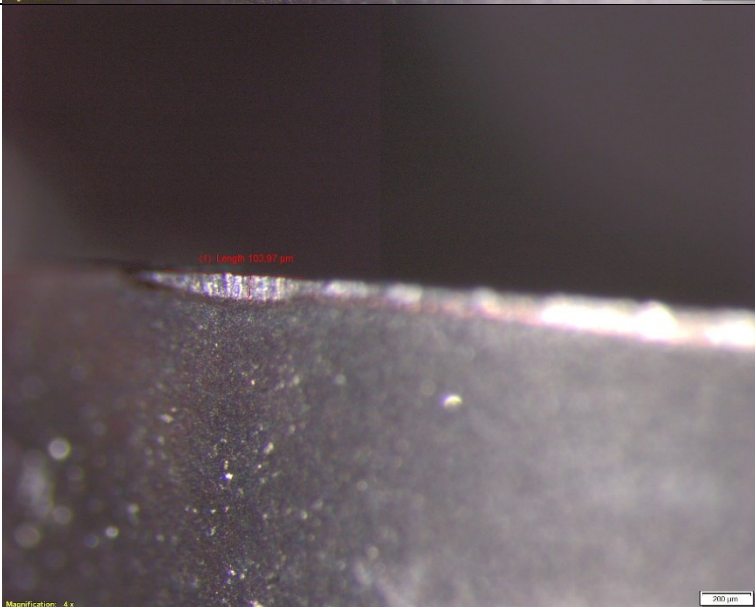
54	 <p>(1) Length 187.35 μm</p> <p>Magnification: 4x</p> <p>200 μm</p>
57	 <p>(1) Length 190.98 μm</p> <p>Magnification: 4x</p> <p>200 μm</p>
60	 <p>(1) Length 199.23 μm</p> <p>Magnification: 4x</p> <p>200 μm</p>

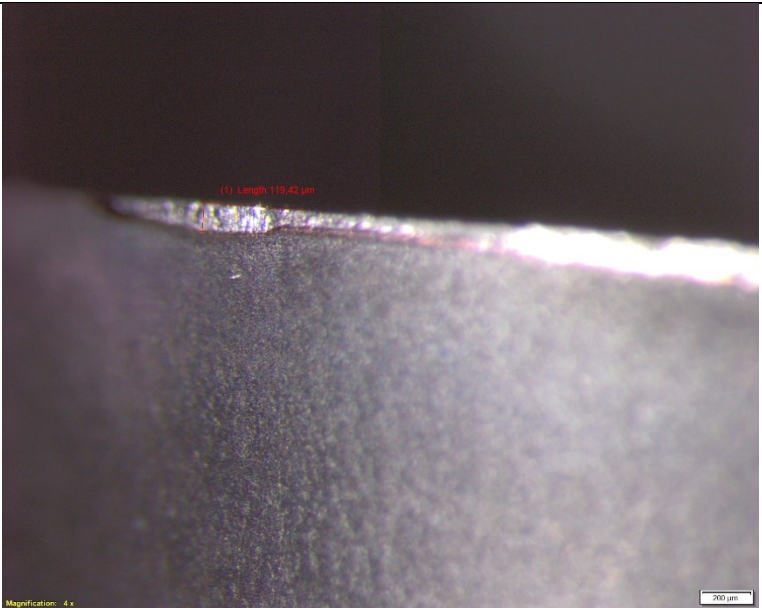
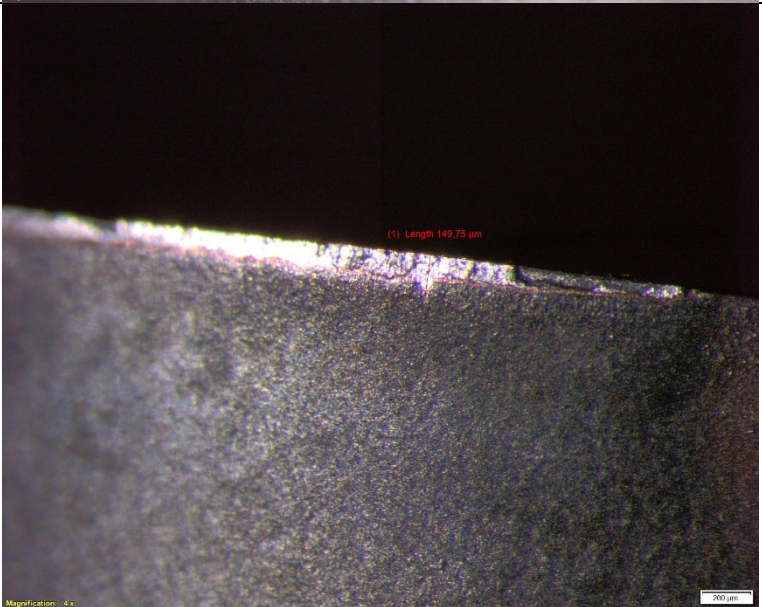
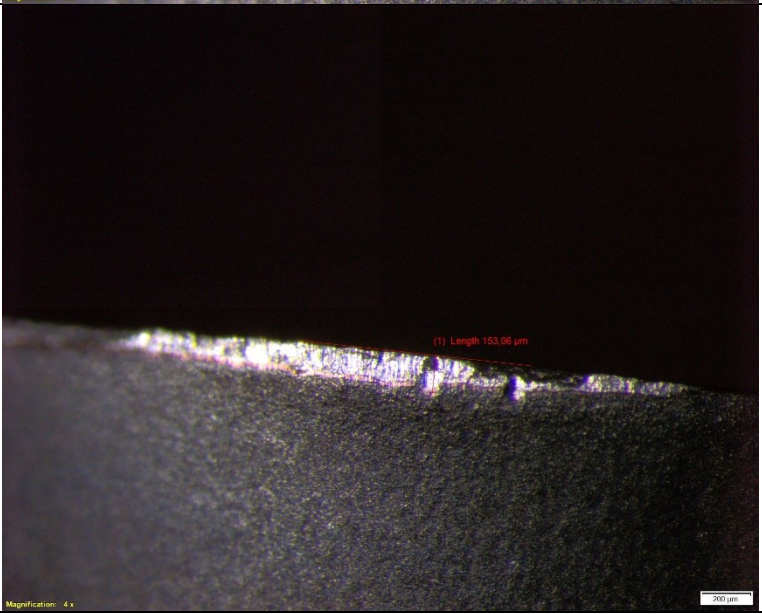
63	 <p>(1) Length 220.06 μm</p> <p>Magnification: 4x</p> <p>200 μm</p>
66	 <p>(1) Length 276.74 μm</p> <p>Magnification: 4x</p> <p>200 μm</p>
68	 <p>(1) Length 306.77 μm</p> <p>Magnification: 4x</p> <p>200 μm</p>

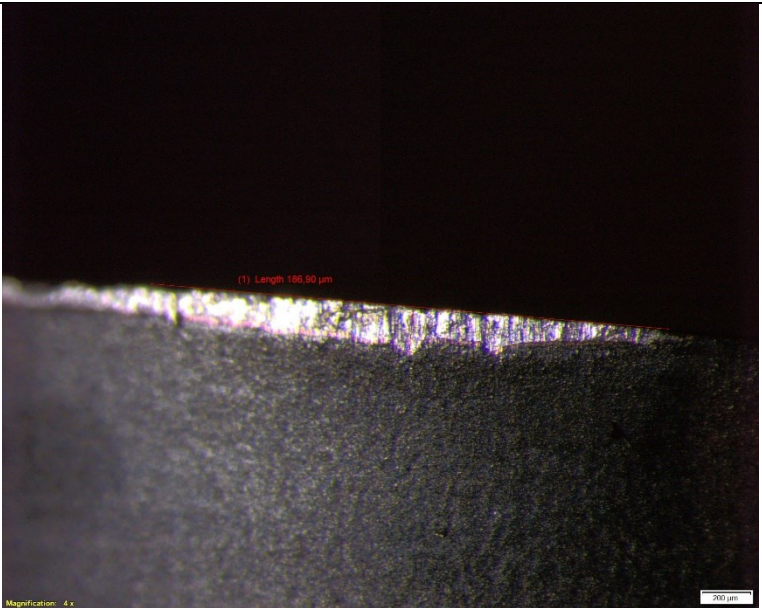
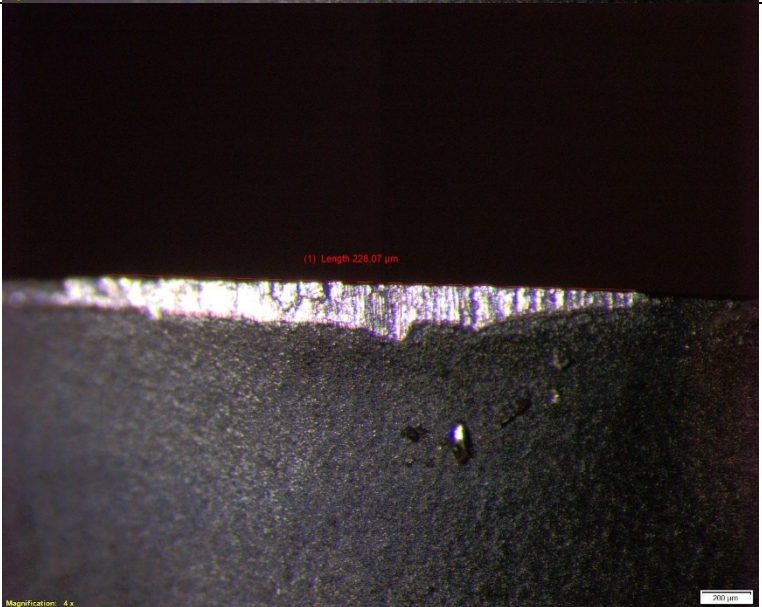
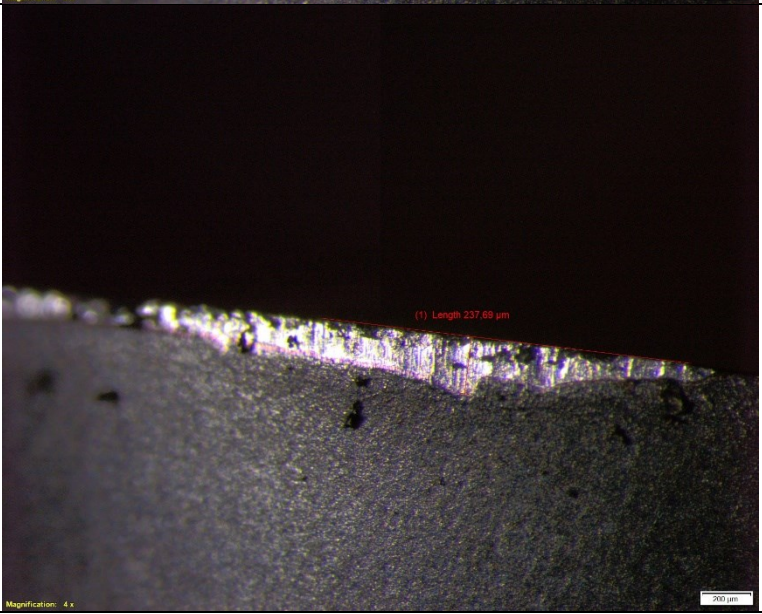
B.2 Images for Test 2

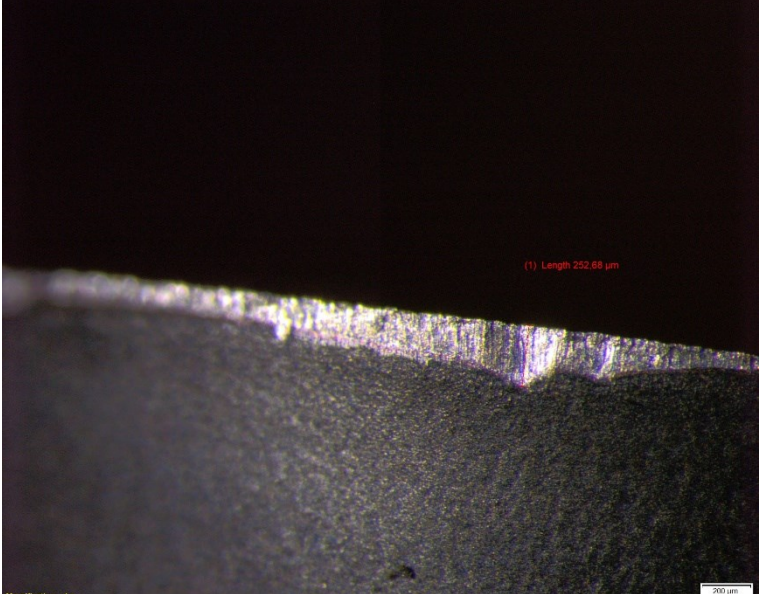
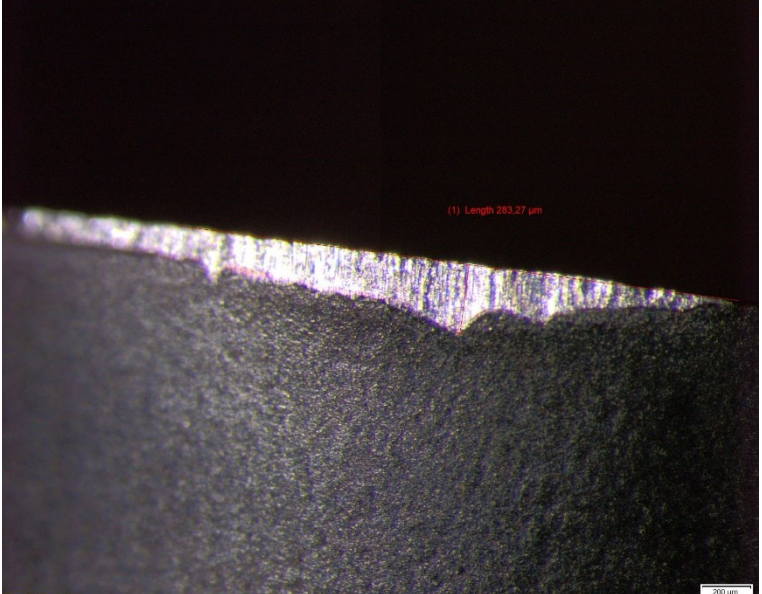
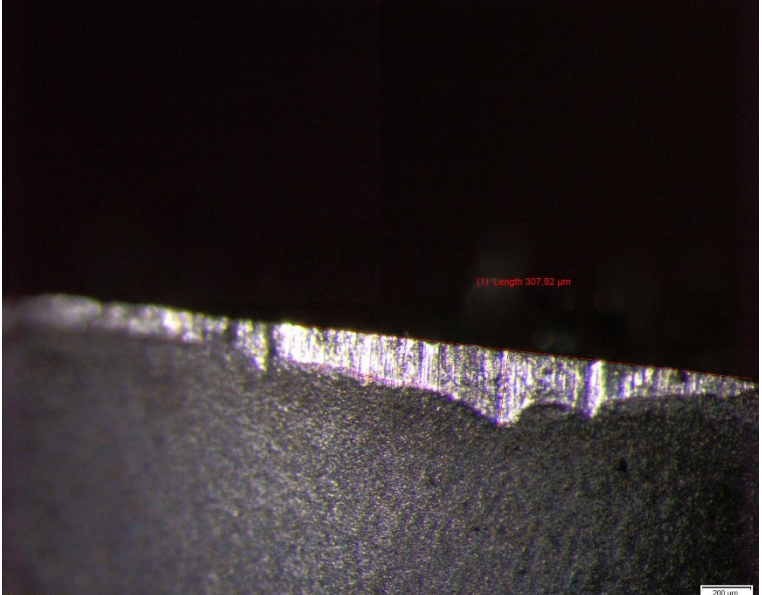
Pass #	Image
4	 <p data-bbox="874 477 963 495">(1) Length 96.56 μm</p> <p data-bbox="475 887 544 902">Magnification: 4 x</p> <p data-bbox="1171 882 1225 898">200 μm</p> <p>This micrograph shows a surface with a fine, granular texture. A red line is drawn across the surface, indicating a length of 96.56 μm. The surface appears to be a thin layer on a substrate. The magnification is 4x, and a 200 μm scale bar is present in the bottom right corner.</p>
10	 <p data-bbox="842 1104 932 1122">(1) Length 46.48 μm</p> <p data-bbox="475 1491 544 1507">Magnification: 4 x</p> <p data-bbox="1171 1487 1225 1503">200 μm</p> <p>This micrograph shows a surface with a fine, granular texture, similar to the one at Pass 4. A red line is drawn across the surface, indicating a length of 46.48 μm. The surface appears to be a thin layer on a substrate. The magnification is 4x, and a 200 μm scale bar is present in the bottom right corner.</p>

16	 <p>(1) Length 54.75 μm</p> <p>Magnification: 4x</p> <p>200 μm</p>
34	 <p>(1) Length 71.03 μm</p> <p>Magnification: 4x</p> <p>200 μm</p>
52	 <p>(1) Length 82.23 μm</p> <p>Magnification: 4x</p> <p>200 μm</p>

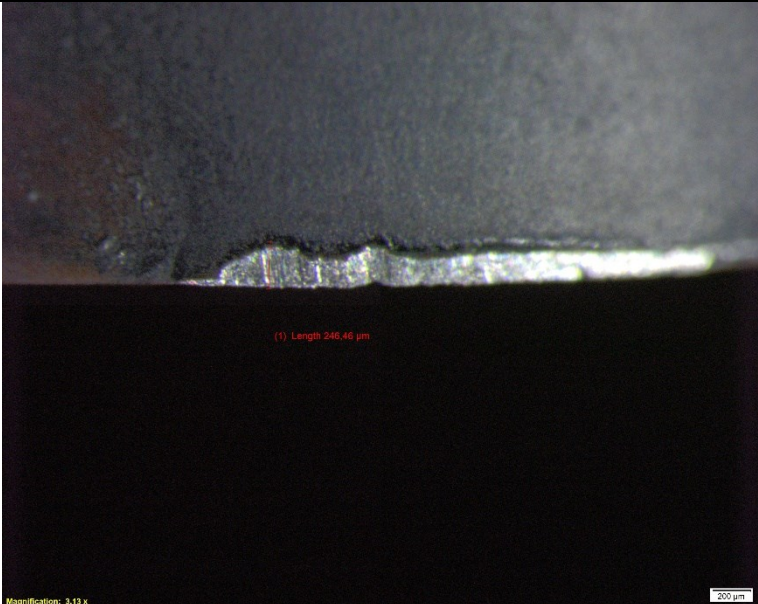
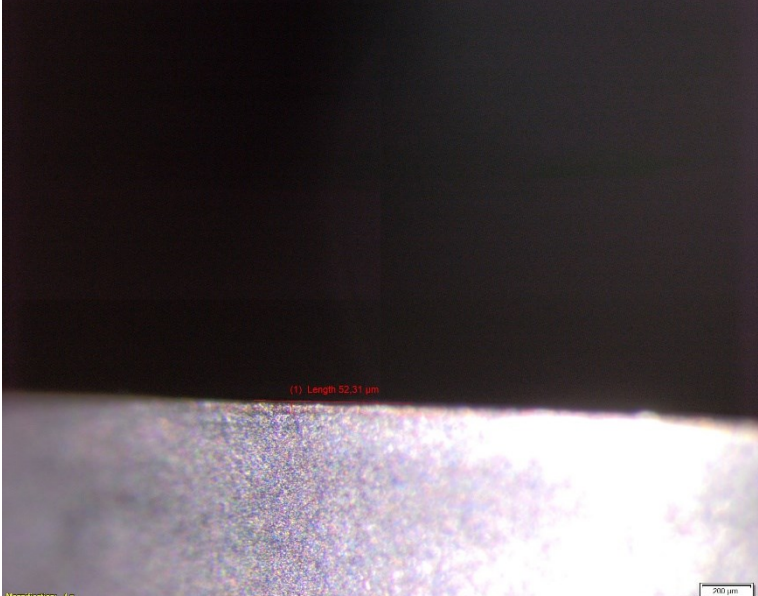
70	 <p>(1) Length 96.29 μm</p> <p>Magnification: 4x</p> <p>200 μm</p>
88	 <p>(1) Length 100.25 μm</p> <p>Magnification: 4x</p> <p>200 μm</p>
106	 <p>(1) Length 102.97 μm</p> <p>Magnification: 4x</p> <p>200 μm</p>



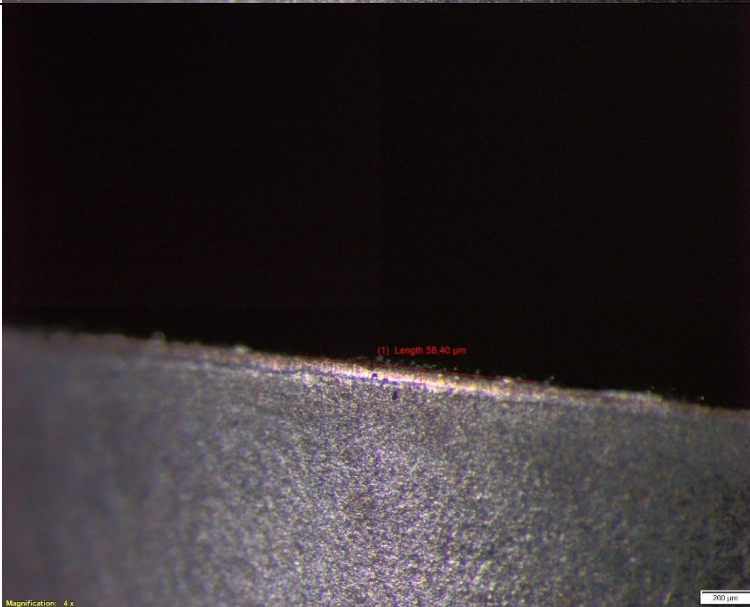
124	 <p>(1) Length 119.42 μm</p> <p>Magnification: 4 x</p> <p>200 μm</p>
142	 <p>(1) Length 149.75 μm</p> <p>Magnification: 4 x</p> <p>200 μm</p>
160	 <p>(1) Length 153.06 μm</p> <p>Magnification: 4 x</p> <p>200 μm</p>



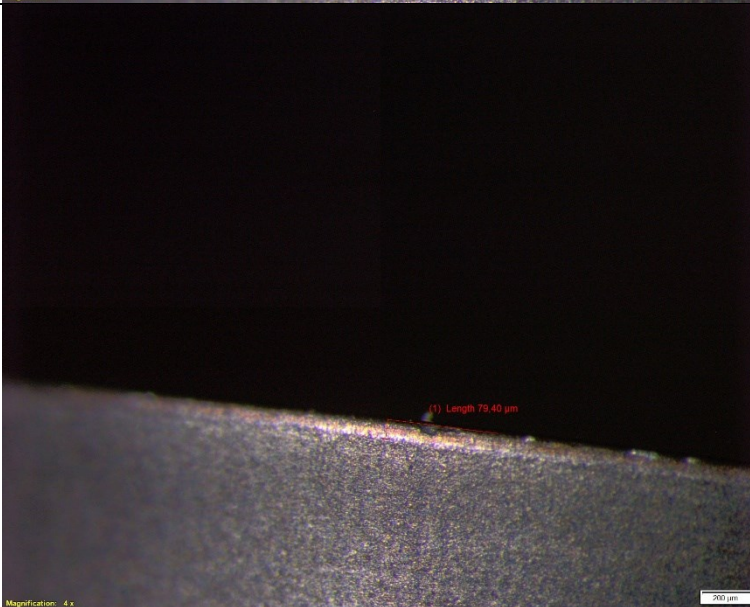
178	 <p>(1) Length 186.90 μm</p> <p>Magnification: 4x</p> <p>200 μm</p>
196	 <p>(1) Length 228.07 μm</p> <p>Magnification: 4x</p> <p>200 μm</p>
202	 <p>(1) Length 237.89 μm</p> <p>Magnification: 4x</p> <p>200 μm</p>

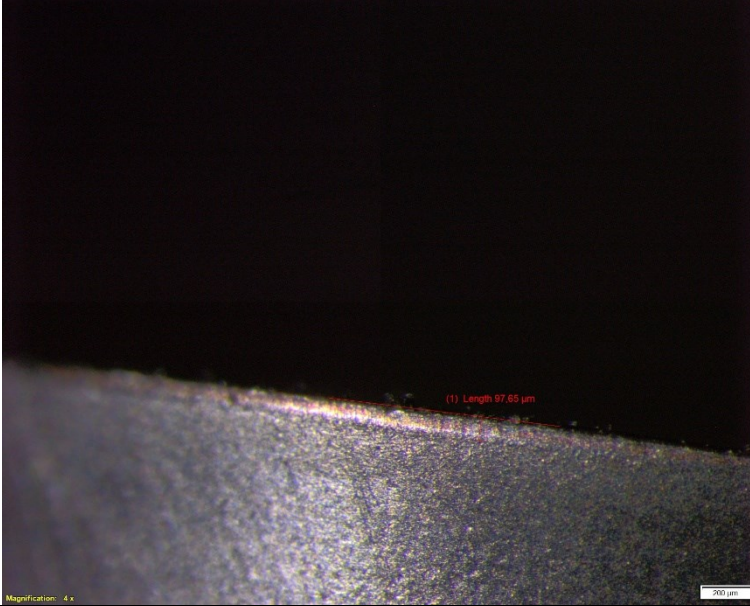
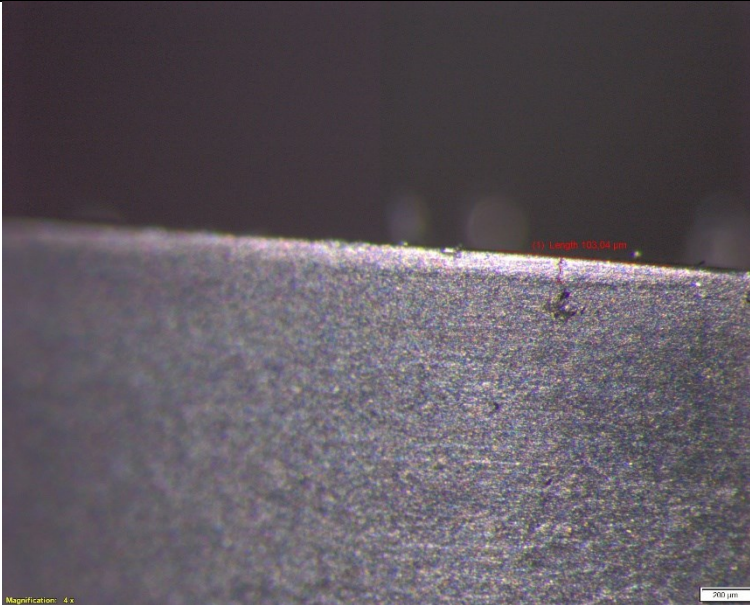
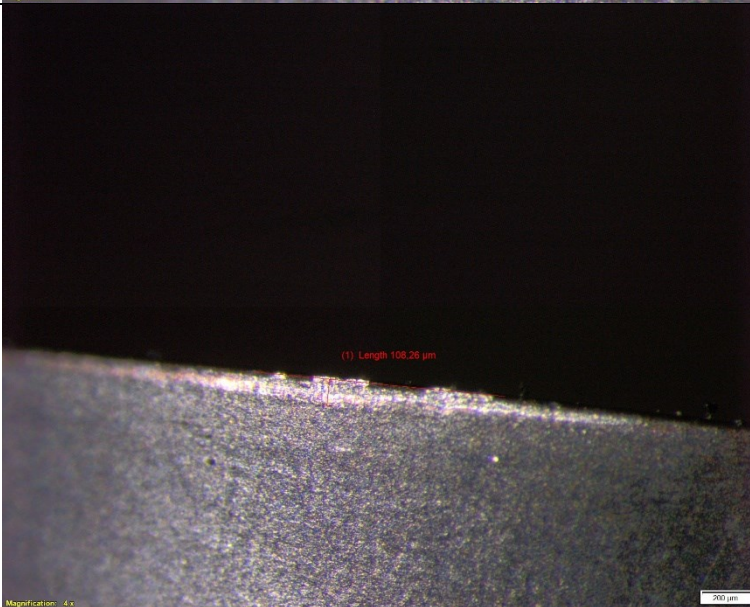
208	 <p>(1) Length 252.68 μm</p> <p>Magnification: 4 x</p> <p>200 μm</p>
214	 <p>(1) Length 293.27 μm</p> <p>Magnification: 4 x</p> <p>200 μm</p>
220	 <p>(1) Length 307.92 μm</p> <p>Magnification: 4 x</p> <p>200 μm</p>

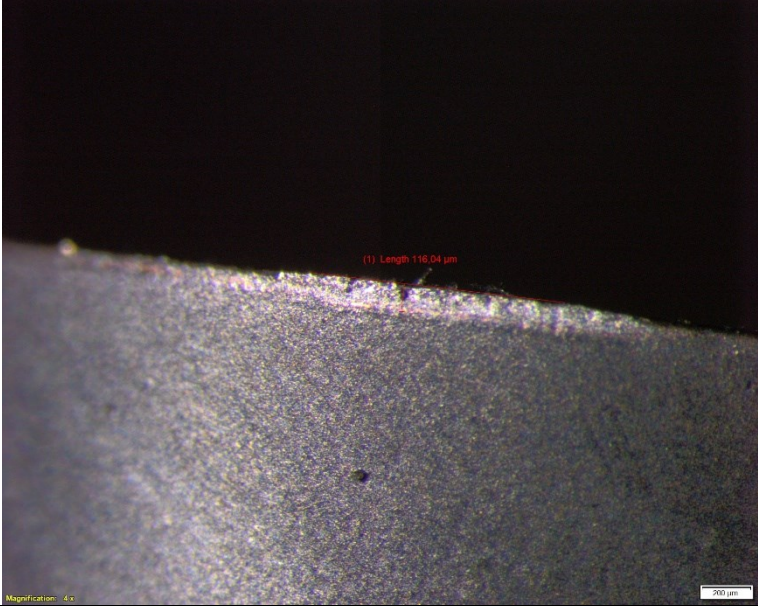
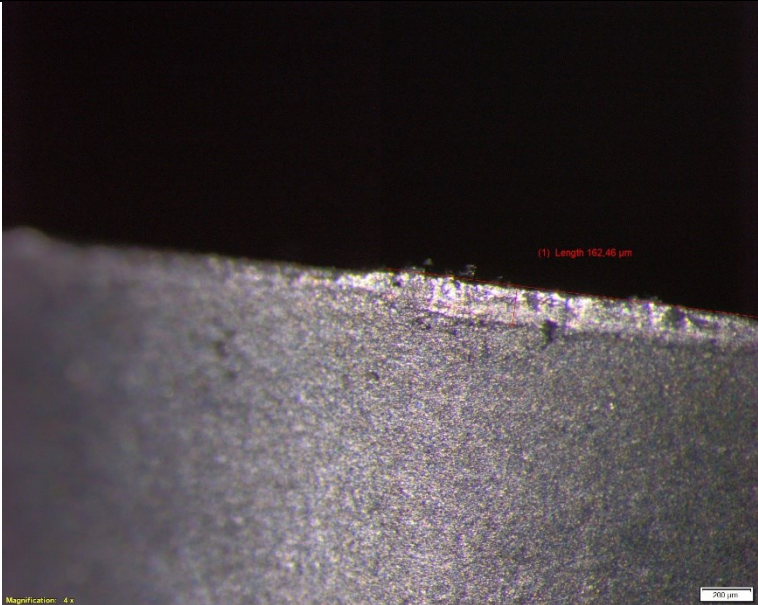
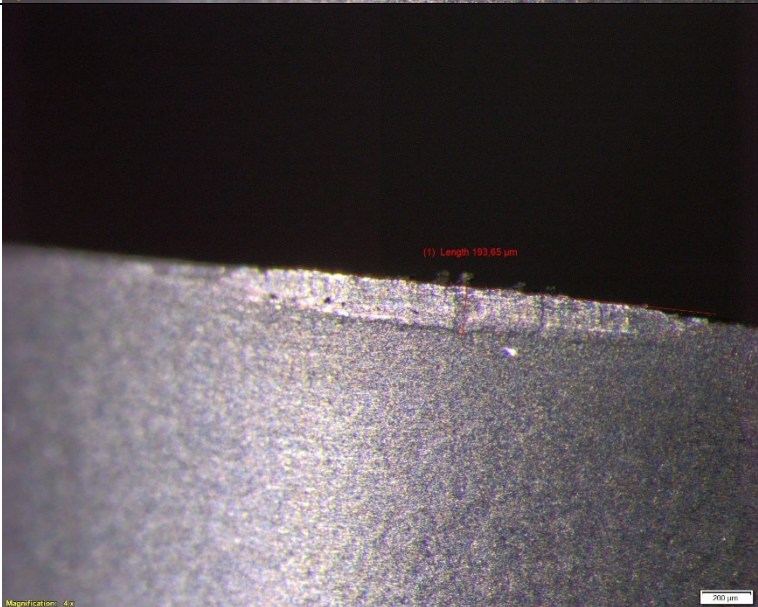
B.3 Images for Test 3

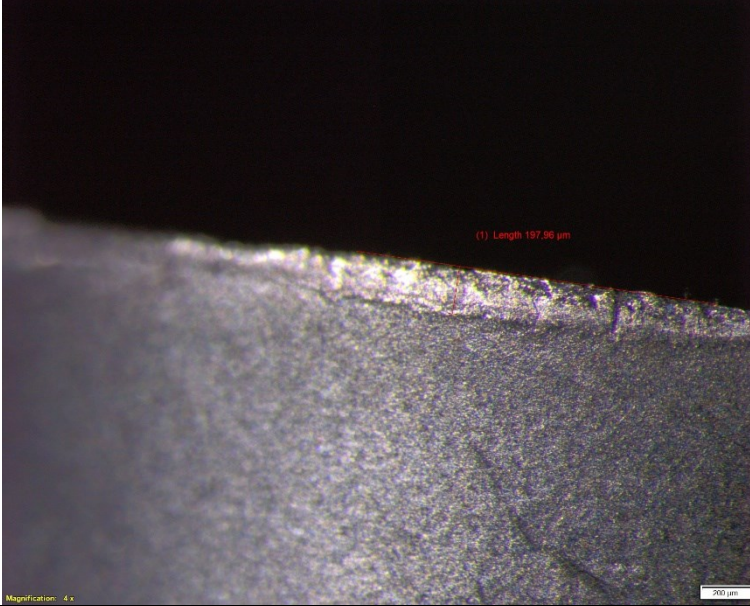
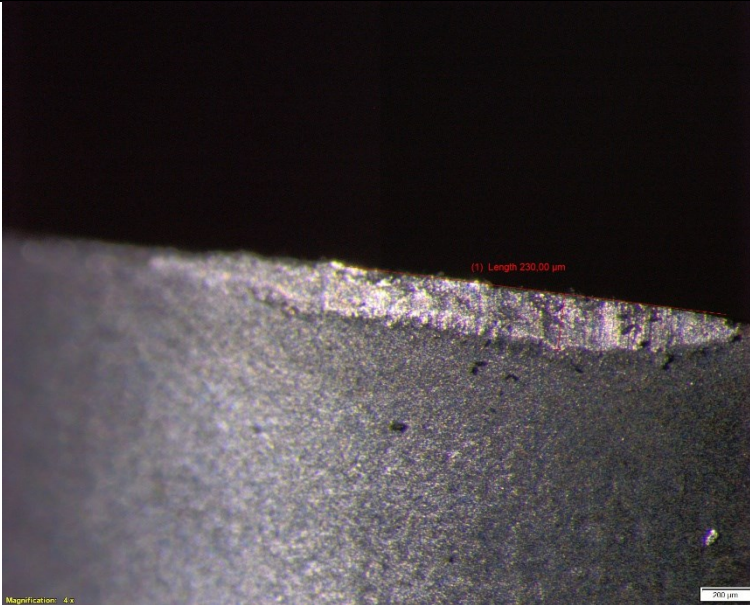
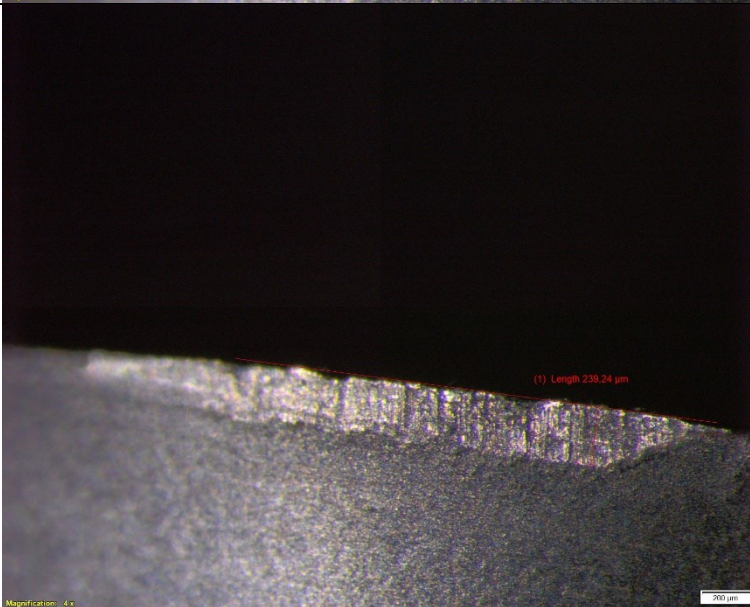
Pass #	Image
1	 <p>(1) Length: 246.46 μm</p> <p>Magnification: 3.13 x</p> <p>200 μm</p> <p>This micrograph shows a dark, textured surface with a prominent, irregular, light-colored defect or crack running horizontally across the middle. The defect has a jagged, irregular shape. A red line is drawn across the defect, with the text '(1) Length: 246.46 μm' in red. The background is dark and grainy. A scale bar in the bottom right corner indicates 200 μm. The magnification is 3.13 x.</p>
2	 <p>(1) Length: 52.31 μm</p> <p>Magnification: 4 x</p> <p>200 μm</p> <p>This micrograph shows a dark, textured surface with a prominent, irregular, light-colored defect or crack running horizontally across the middle. The defect has a jagged, irregular shape. A red line is drawn across the defect, with the text '(1) Length: 52.31 μm' in red. The background is dark and grainy. A scale bar in the bottom right corner indicates 200 μm. The magnification is 4 x.</p>

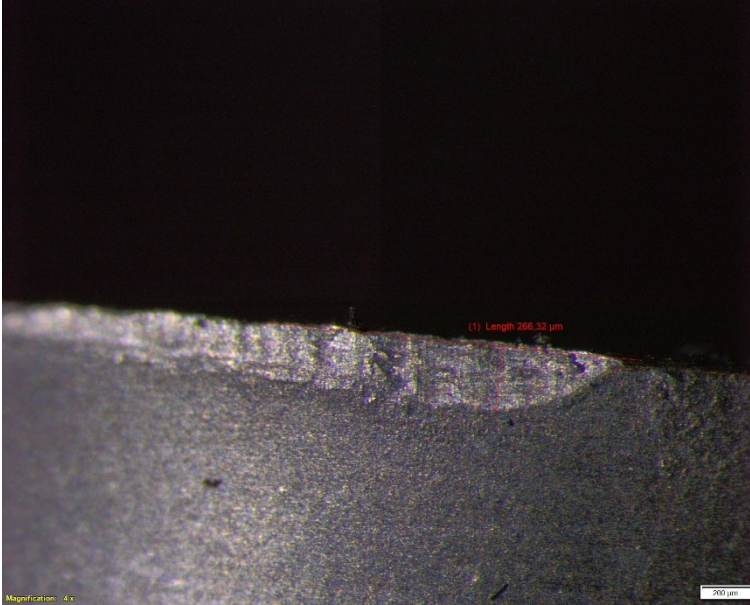
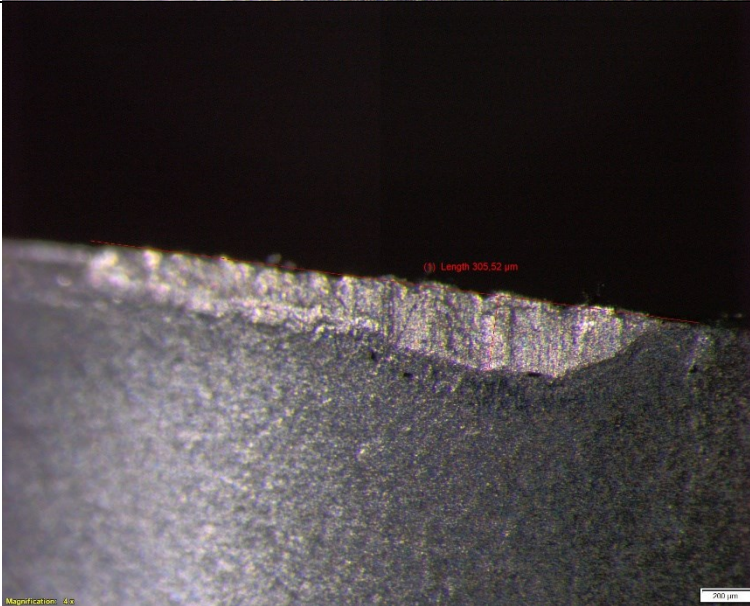
3	 <p>(1) Length 56.28 μm</p> <p>Magnification: 4x</p> <p>200 μm</p>
4	 <p>(1) Length 59.31 μm</p> <p>Magnification: 4x</p> <p>200 μm</p>
5	 <p>(1) Length 56.40 μm</p> <p>Magnification: 4x</p> <p>200 μm</p>

6	 <p>(1) Length 71.90 μm</p> <p>Magnification: 4x</p> <p>200 μm</p>
7	 <p>(1) Length 74.48 μm</p> <p>Magnification: 4x</p> <p>200 μm</p>
8	 <p>(1) Length 79.40 μm</p> <p>Magnification: 4x</p> <p>200 μm</p>

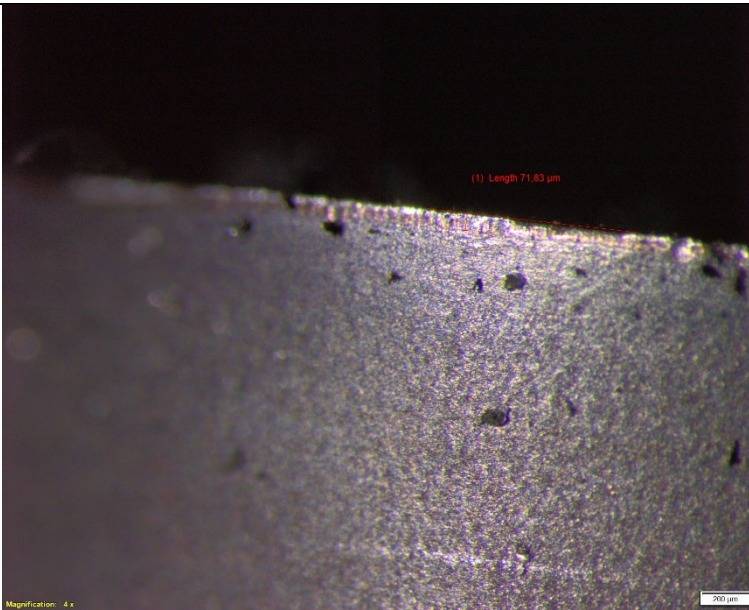
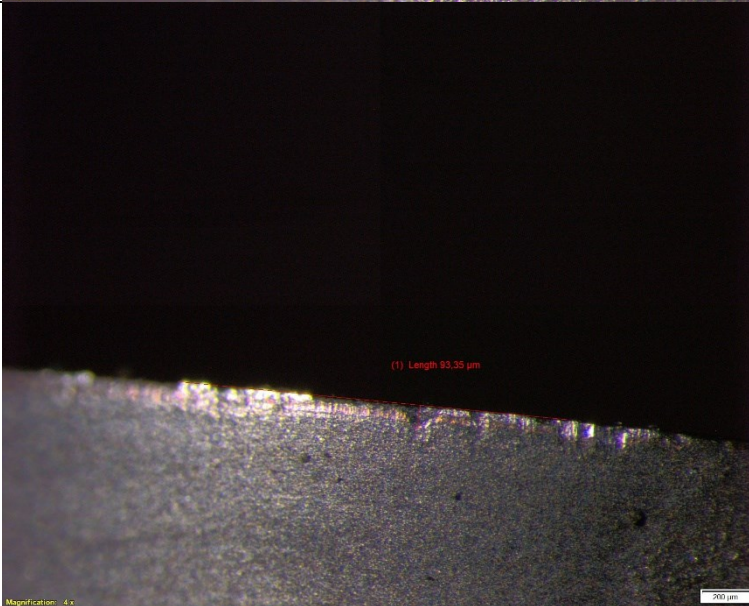
9	 <p>(1) Length 97.85 μm</p> <p>Magnification: 4x</p> <p>200 μm</p>
10	 <p>(1) Length 100.94 μm</p> <p>Magnification: 4x</p> <p>200 μm</p>
12	 <p>(1) Length 108.26 μm</p> <p>Magnification: 4x</p> <p>200 μm</p>

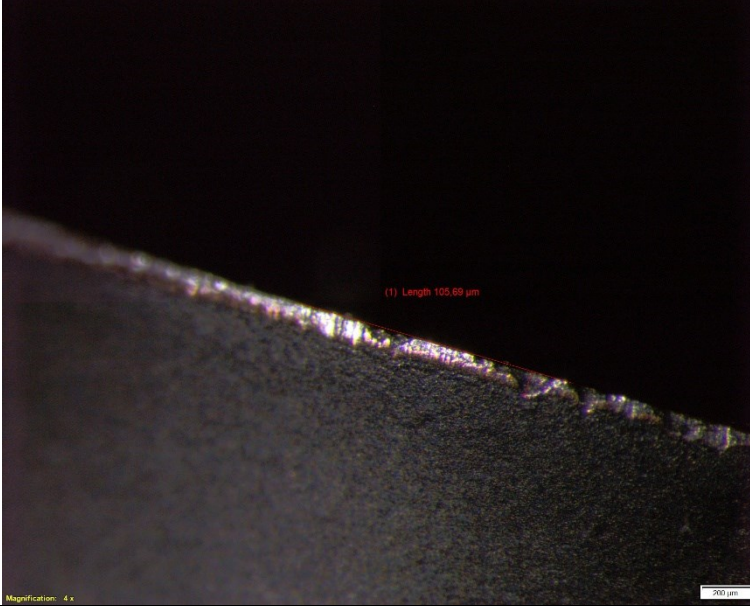
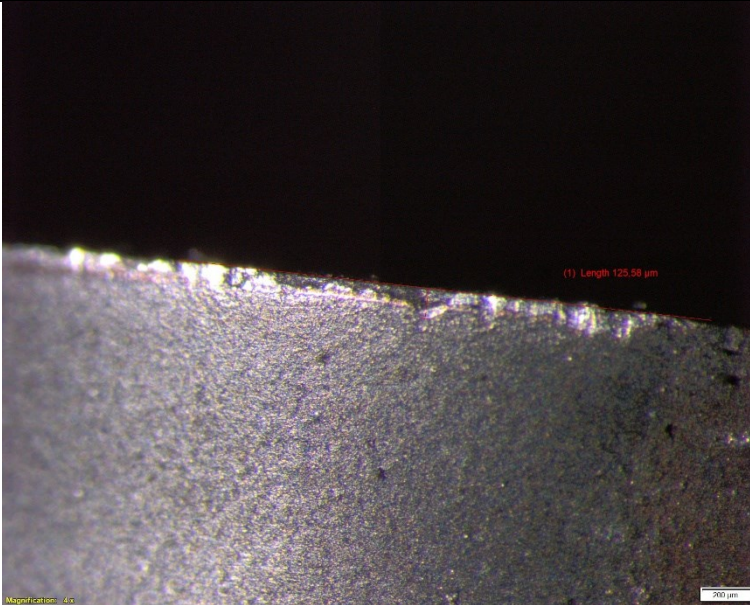
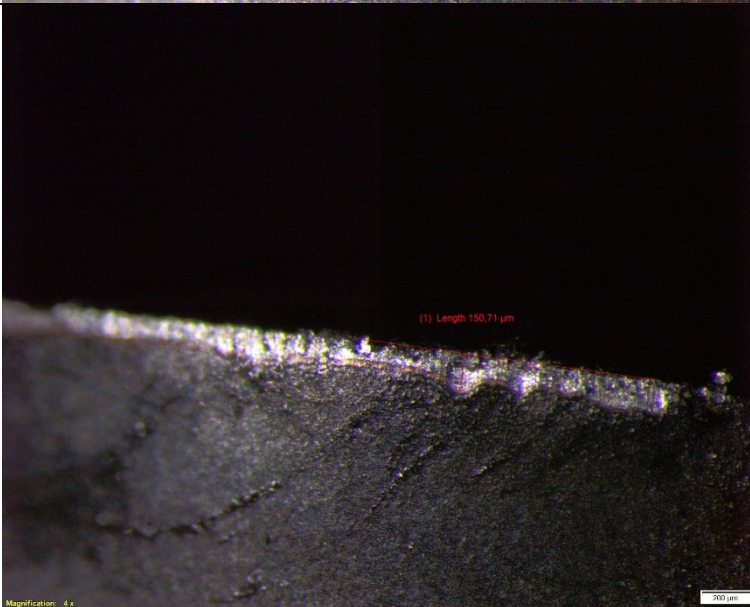
14	 <p>(1) Length 118.04 μm</p> <p>Magnification: 4x</p> <p>200 μm</p>
16	 <p>(1) Length 162.46 μm</p> <p>Magnification: 4x</p> <p>200 μm</p>
18	 <p>(1) Length 193.65 μm</p> <p>Magnification: 4x</p> <p>200 μm</p>

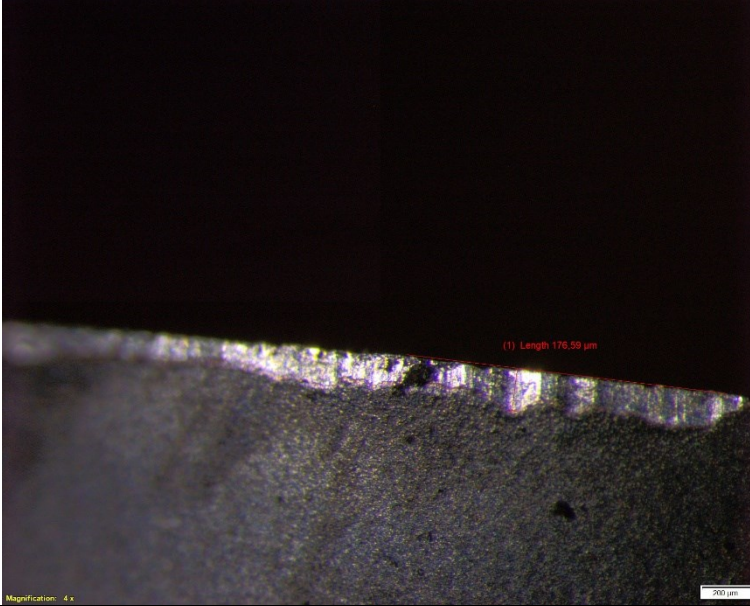
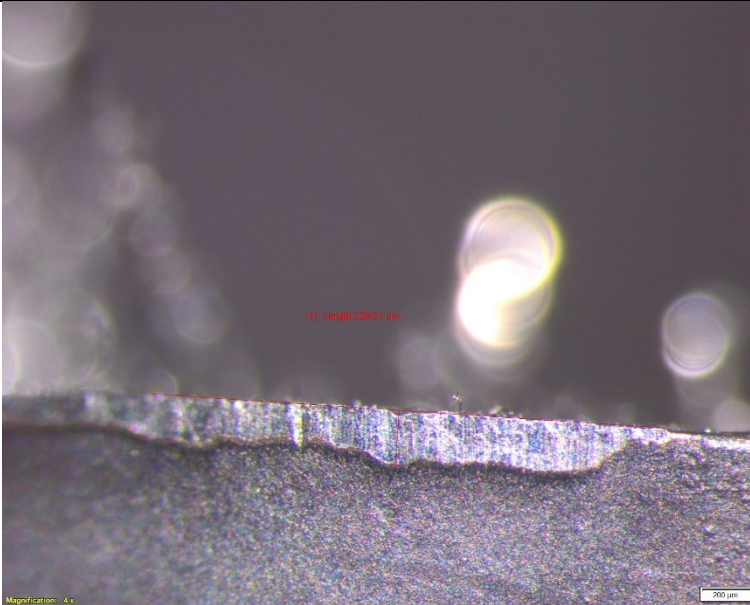
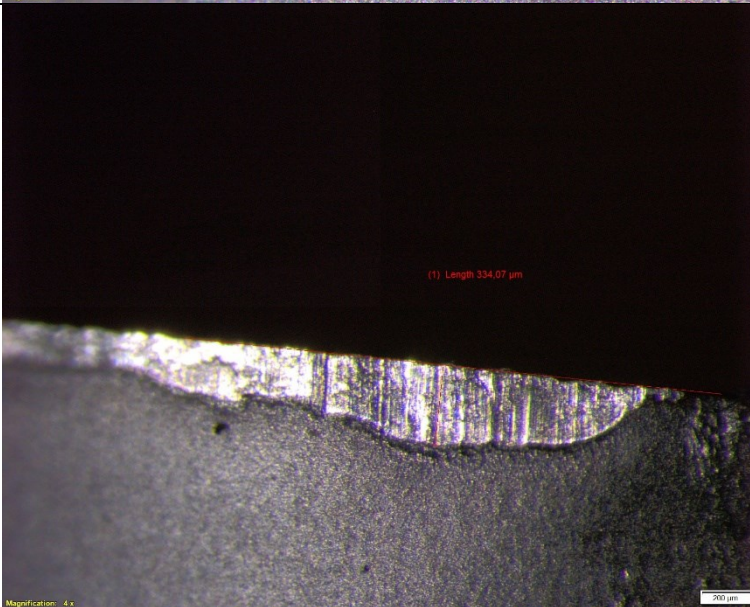
20	 <p>(1) Length 197.96 μm</p> <p>Magnification: 4x</p> <p>200 μm</p>
22	 <p>(1) Length 230.00 μm</p> <p>Magnification: 4x</p> <p>200 μm</p>
24	 <p>(1) Length 239.24 μm</p> <p>Magnification: 4x</p> <p>200 μm</p>

26	 <p>(1) Length 266.32 μm</p> <p>Magnification: 4x</p> <p>100 μm</p>
28	 <p>(3) Length 305.52 μm</p> <p>Magnification: 4x</p> <p>100 μm</p>

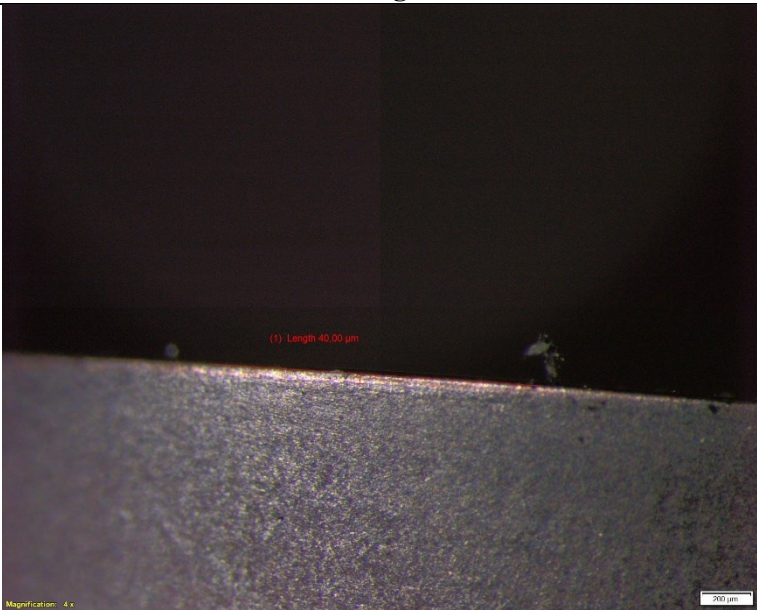
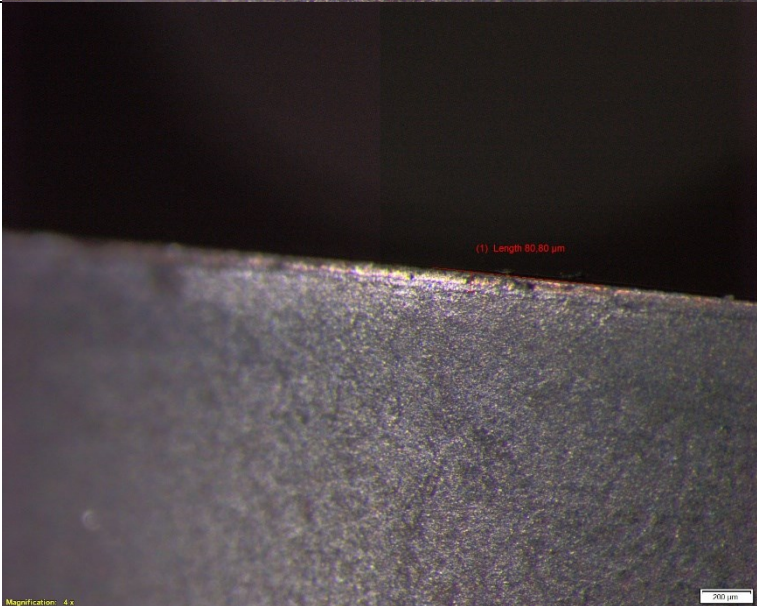
B.4 Images for Test 4

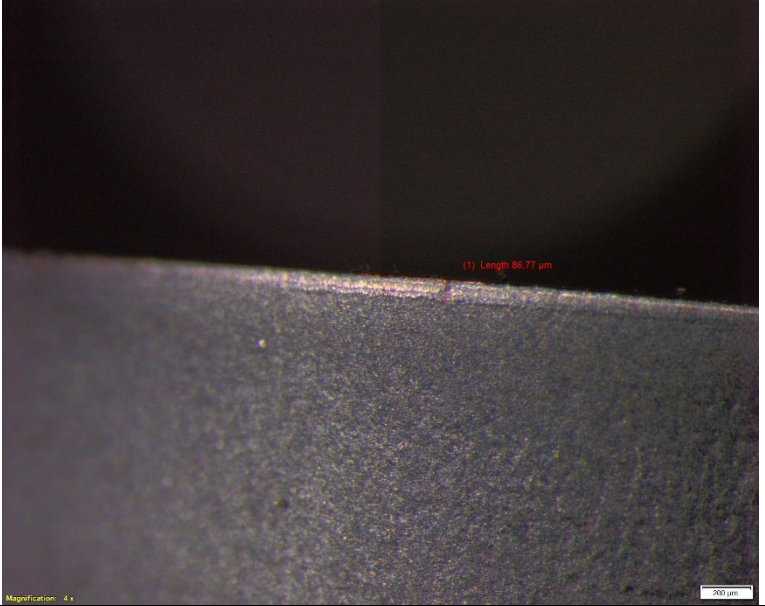
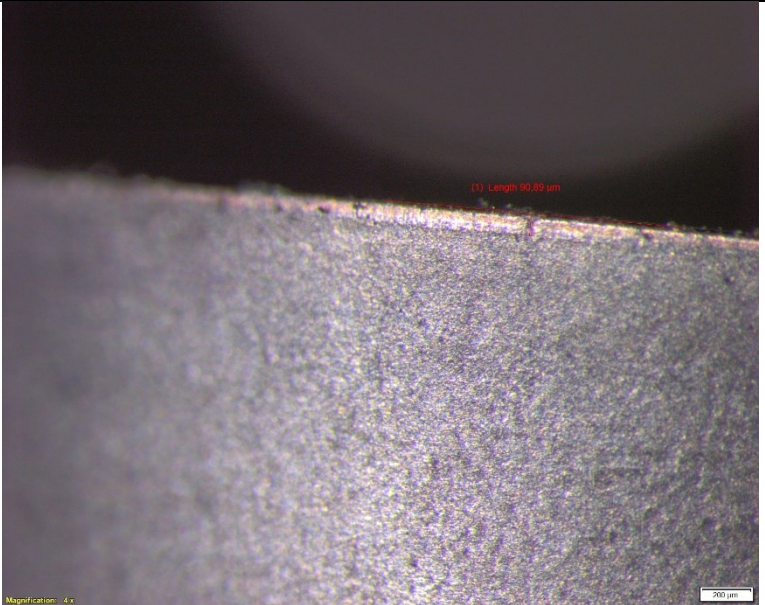
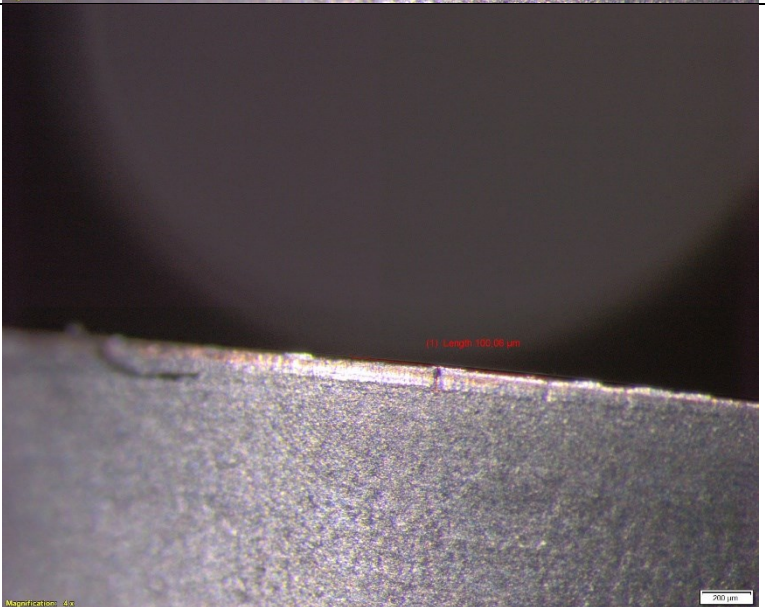
Pass #	Image
18	 <p>(1) Length 71.83 μm</p> <p>Magnification: 4x</p> <p>200 μm</p> <p>This micrograph shows a surface with a fine, granular texture. A red line is drawn across the surface, and a measurement of 71.83 μm is indicated. The surface appears to have some small, dark spots or inclusions. The magnification is 4x, and a 200 μm scale bar is present in the bottom right corner.</p>
36	 <p>(1) Length 83.35 μm</p> <p>Magnification: 4x</p> <p>200 μm</p> <p>This micrograph shows a surface with a fine, granular texture, similar to the one at Pass 18. A red line is drawn across the surface, and a measurement of 83.35 μm is indicated. The surface appears to have some small, dark spots or inclusions. The magnification is 4x, and a 200 μm scale bar is present in the bottom right corner.</p>

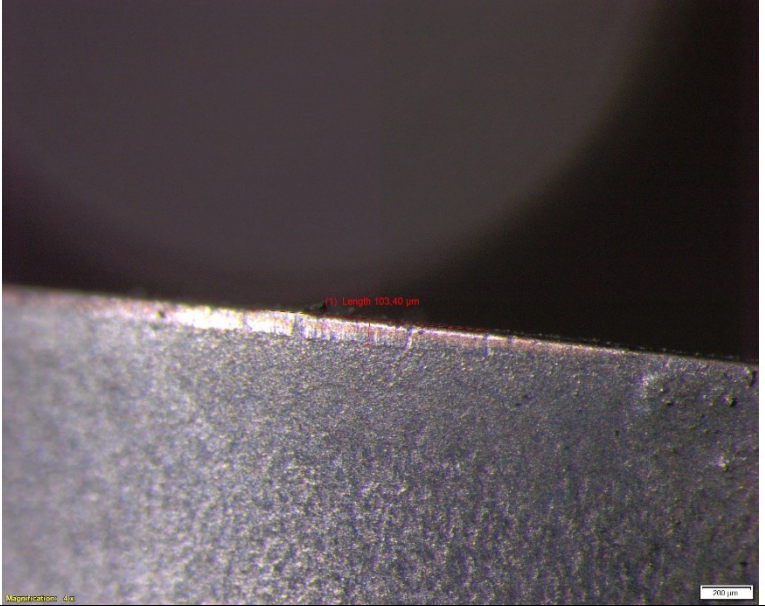
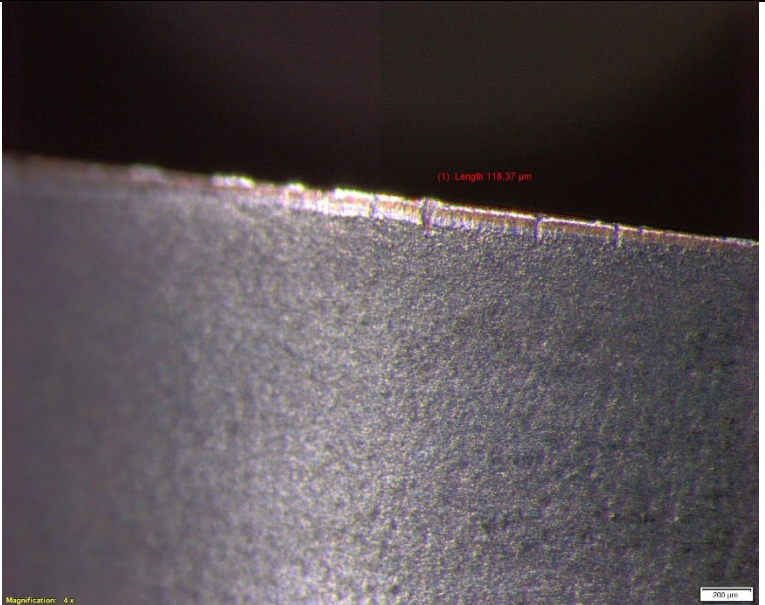
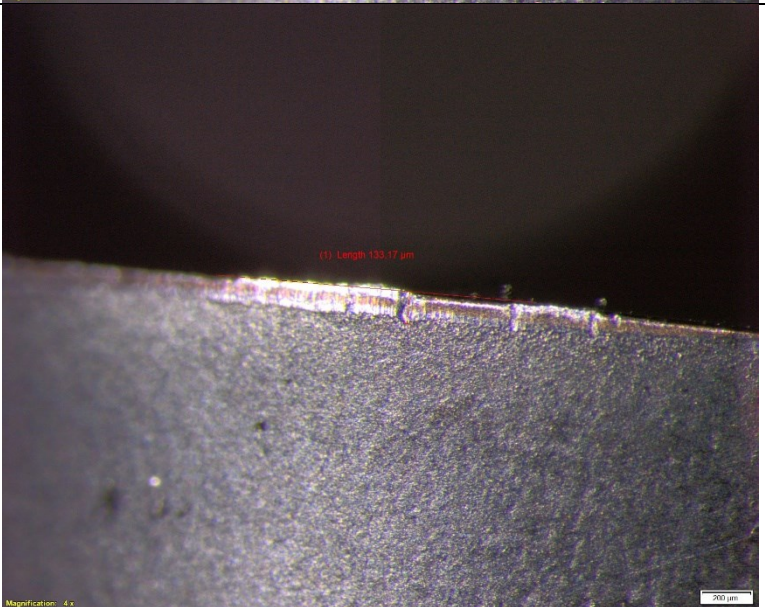
54	 <p>(1) Length 105.69 μm</p> <p>Magnification: 4x</p> <p>200 μm</p>
72	 <p>(1) Length 125.58 μm</p> <p>Magnification: 4x</p> <p>200 μm</p>
90	 <p>(1) Length 150.71 μm</p> <p>Magnification: 4x</p> <p>200 μm</p>

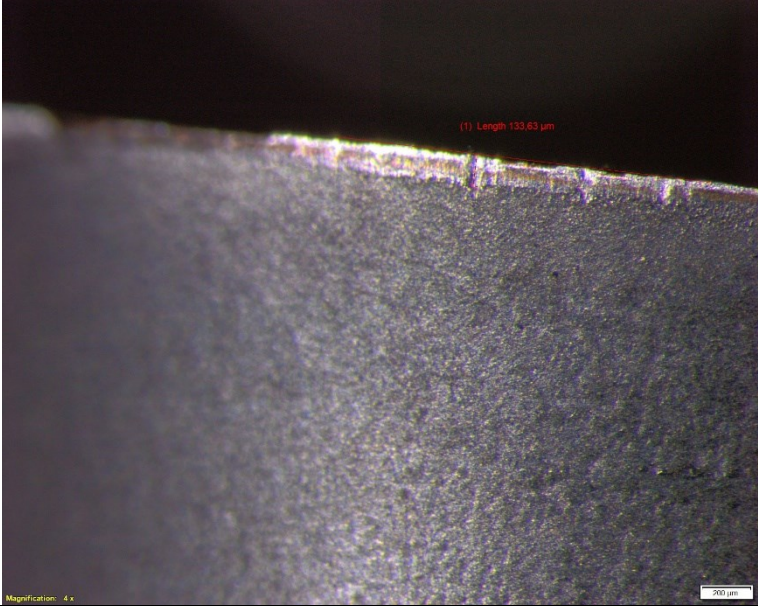
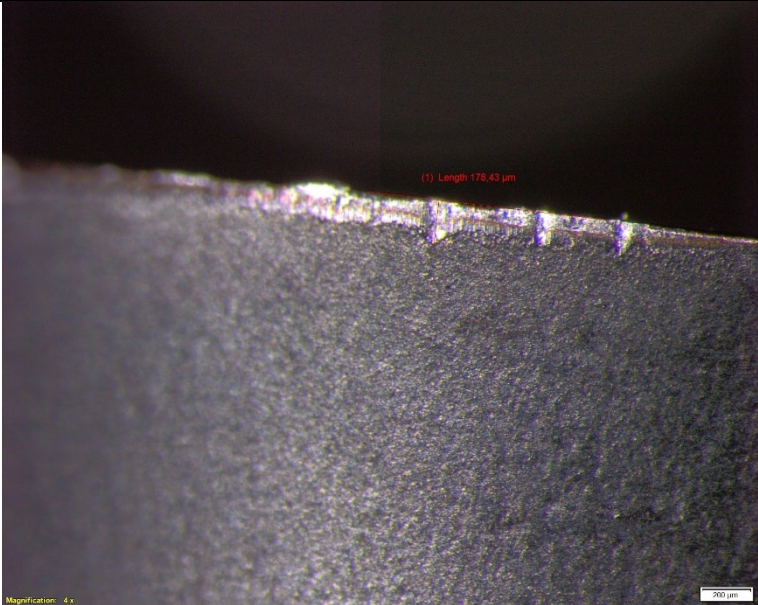
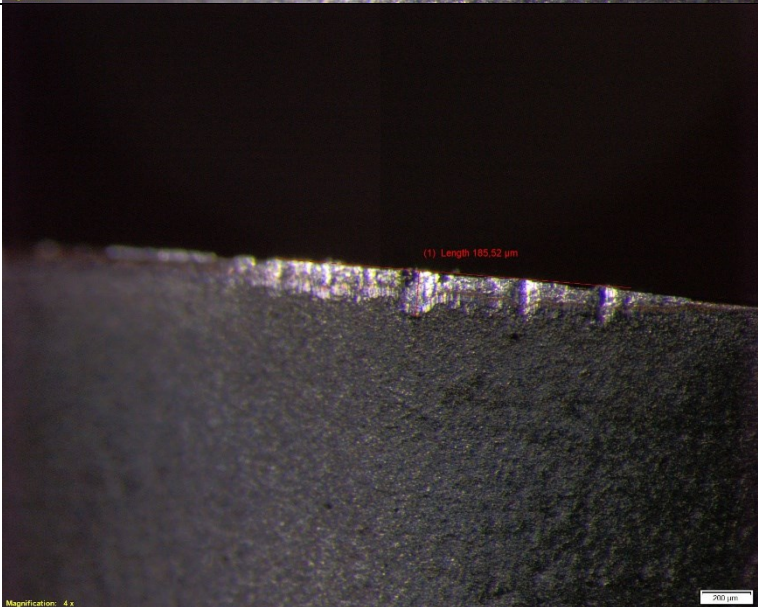
108	 <p>(1) Length 176.59 μm</p> <p>Magnification: 4x</p> <p>200 μm</p>
126	 <p>(1) Length 226.21 μm</p> <p>Magnification: 4x</p> <p>200 μm</p>
144	 <p>(1) Length 334.07 μm</p> <p>Magnification: 4x</p> <p>200 μm</p>

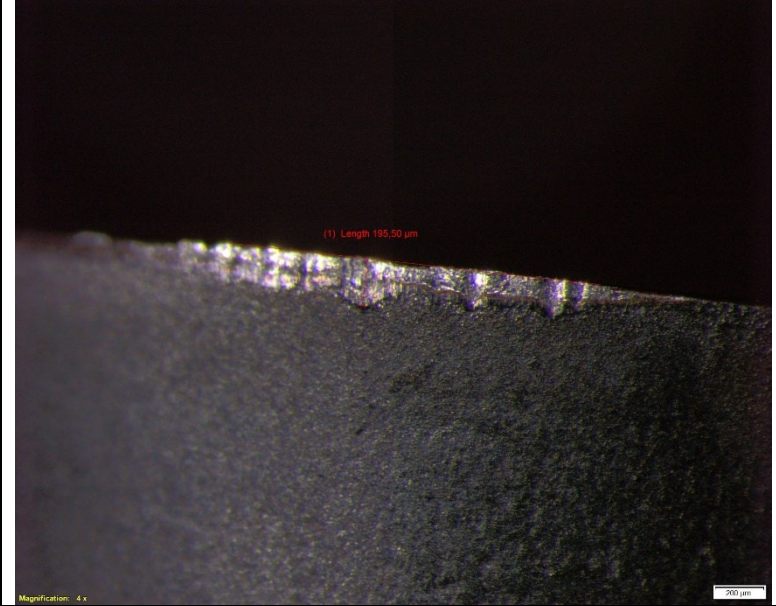
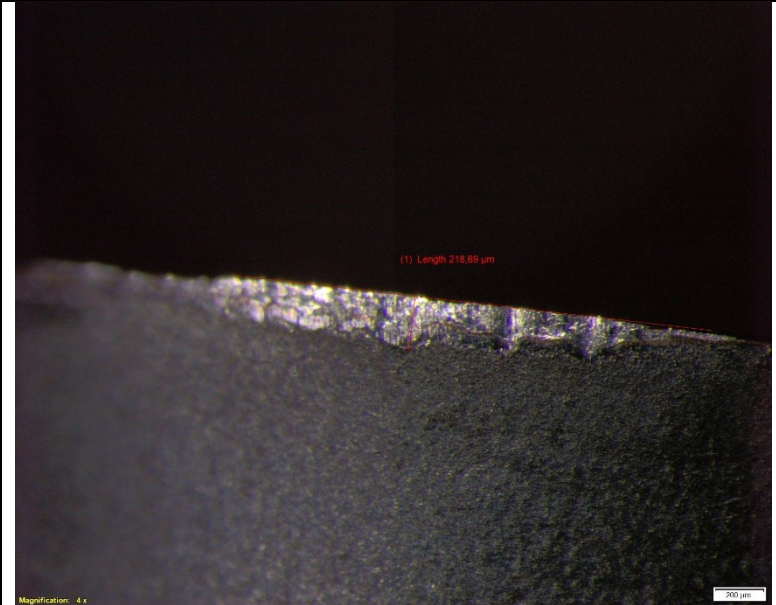
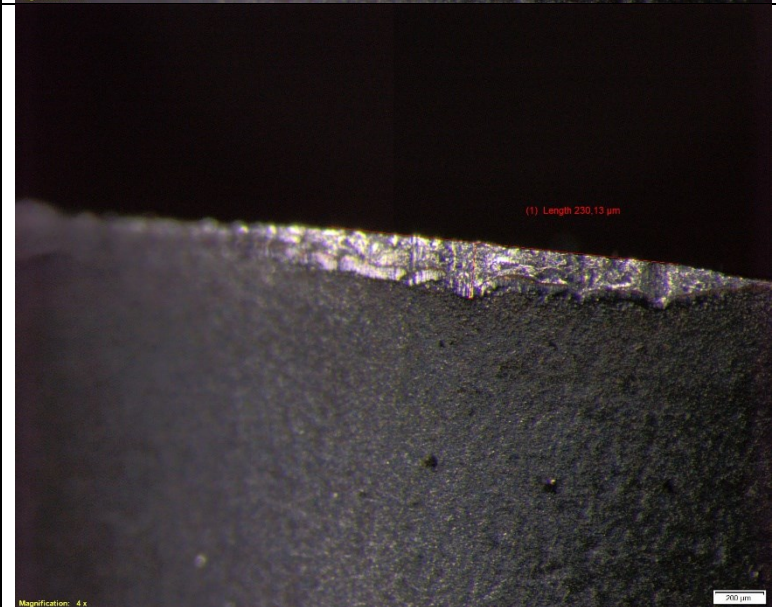
B.5 Images for Test 5

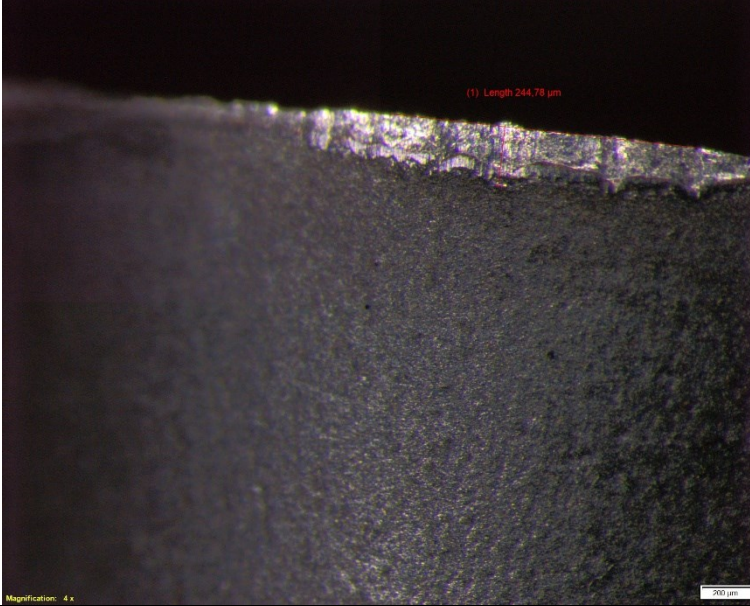
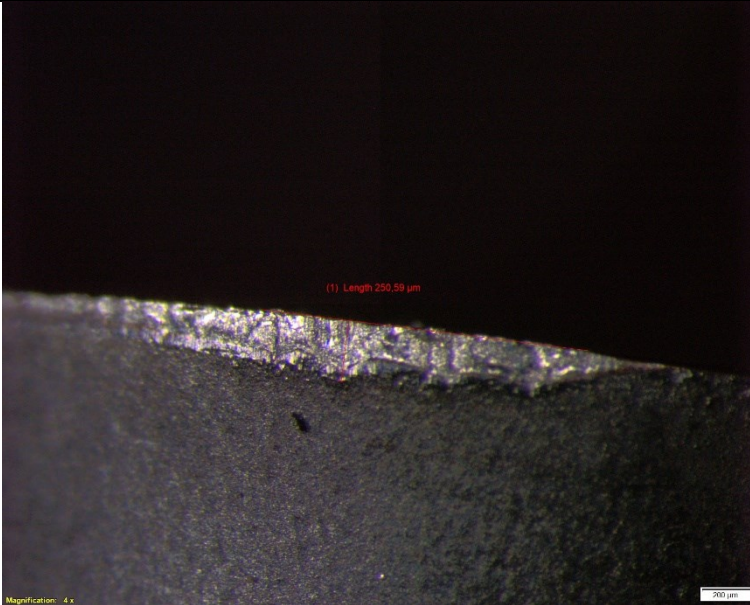
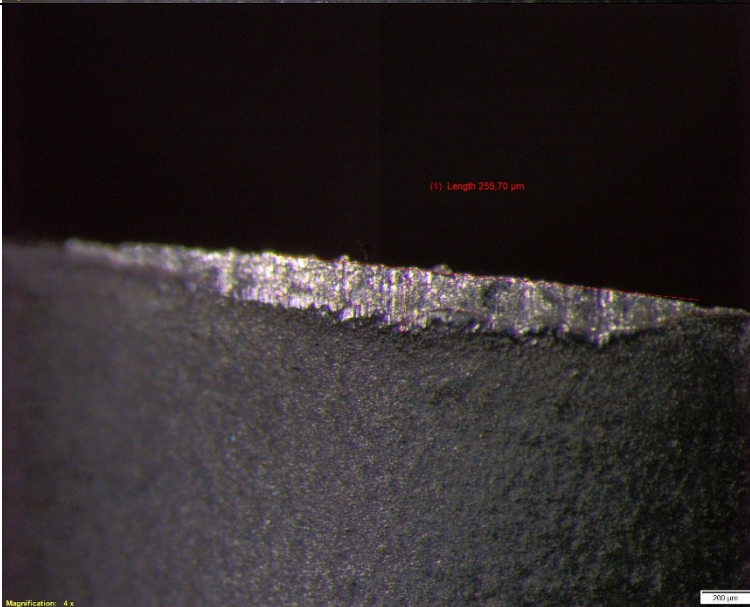
Pass #	Image
5	 <p data-bbox="746 622 842 645">(1) Length 40.00 µm</p> <p data-bbox="480 891 555 904">Magnification: 4x</p> <p data-bbox="1182 887 1230 900">200 µm</p>
10	 <p data-bbox="954 1144 1050 1167">(1) Length 80.00 µm</p> <p data-bbox="480 1496 555 1509">Magnification: 4x</p> <p data-bbox="1182 1491 1230 1505">200 µm</p>

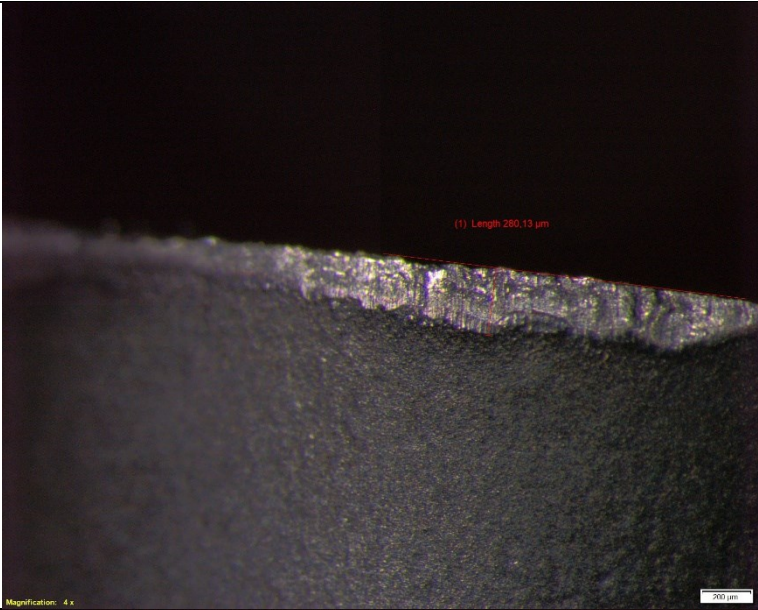
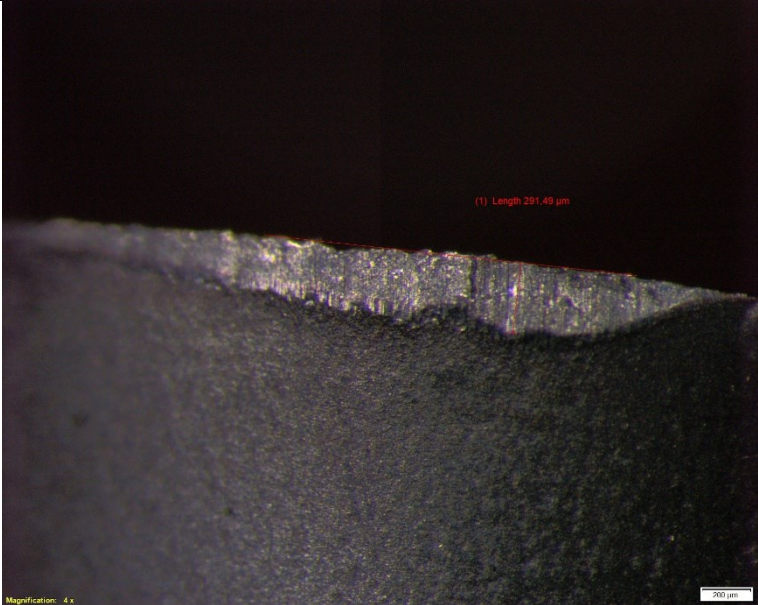
<p>11</p>	 <p>(1) Length 86.77 μm</p> <p>Magnification: 4x</p> <p>200 μm</p>
<p>14</p>	 <p>(1) Length 90.89 μm</p> <p>Magnification: 4x</p> <p>200 μm</p>
<p>17</p>	 <p>(1) Length 102.06 μm</p> <p>Magnification: 4x</p> <p>200 μm</p>

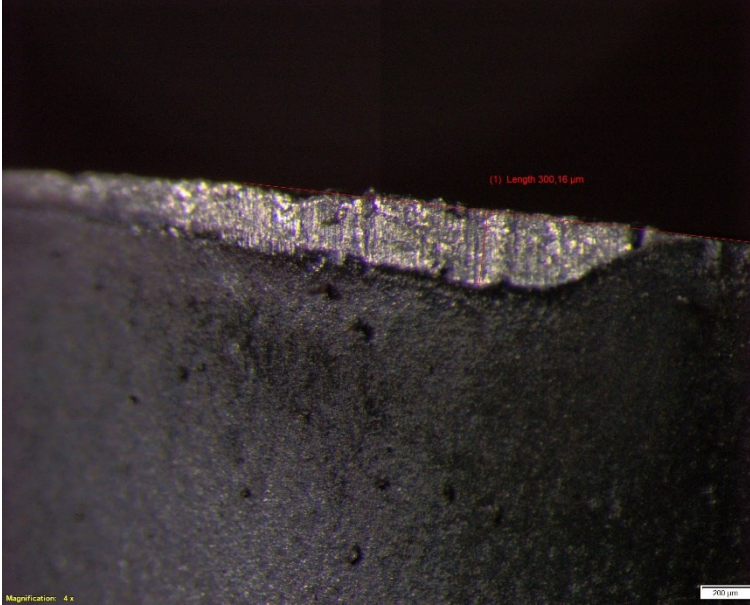
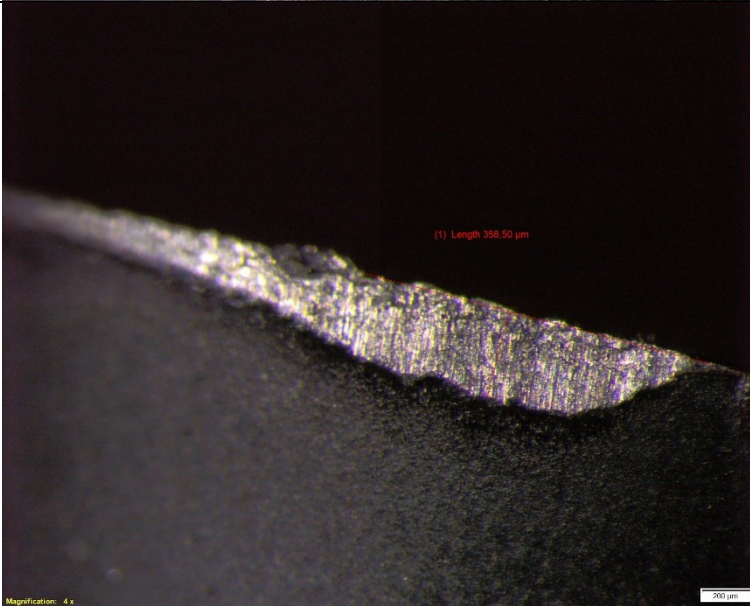
20	 <p>(1) Length 103.40 μm</p> <p>Magnification: 4x</p> <p>200 μm</p>
23	 <p>(1) Length 118.37 μm</p> <p>Magnification: 4x</p> <p>200 μm</p>
26	 <p>(1) Length 133.17 μm</p> <p>Magnification: 4x</p> <p>200 μm</p>

29	 <p>(1) Length 133.63 μm</p> <p>Magnification: 4 x</p> <p>200 μm</p>
32	 <p>(1) Length 176.43 μm</p> <p>Magnification: 4 x</p> <p>200 μm</p>
35	 <p>(1) Length 185.02 μm</p> <p>Magnification: 4 x</p> <p>200 μm</p>

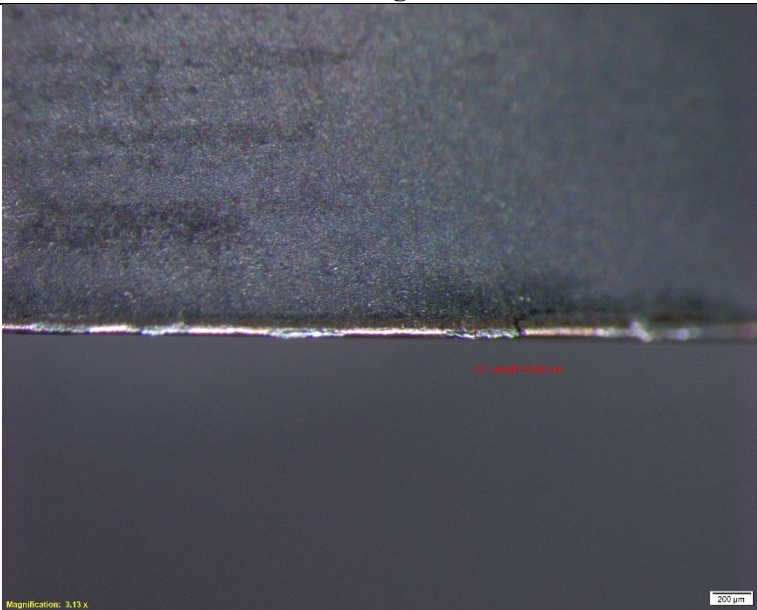
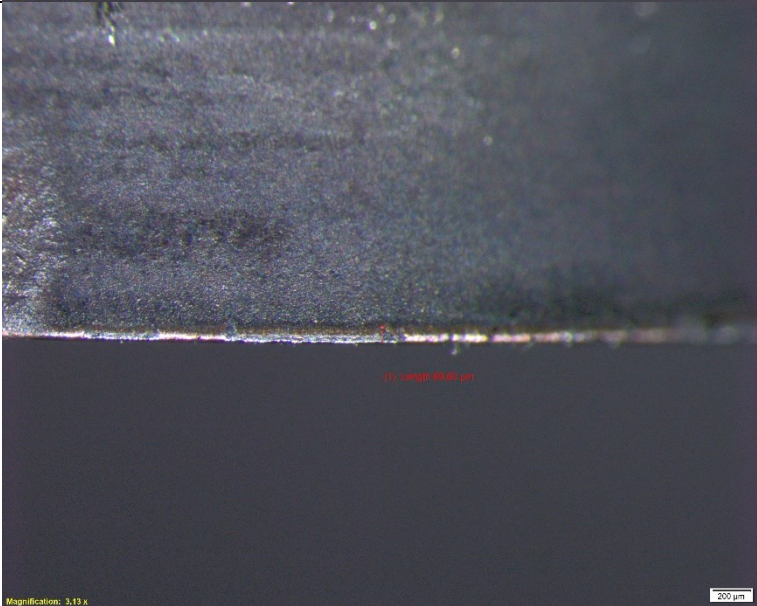
38	
41	
44	

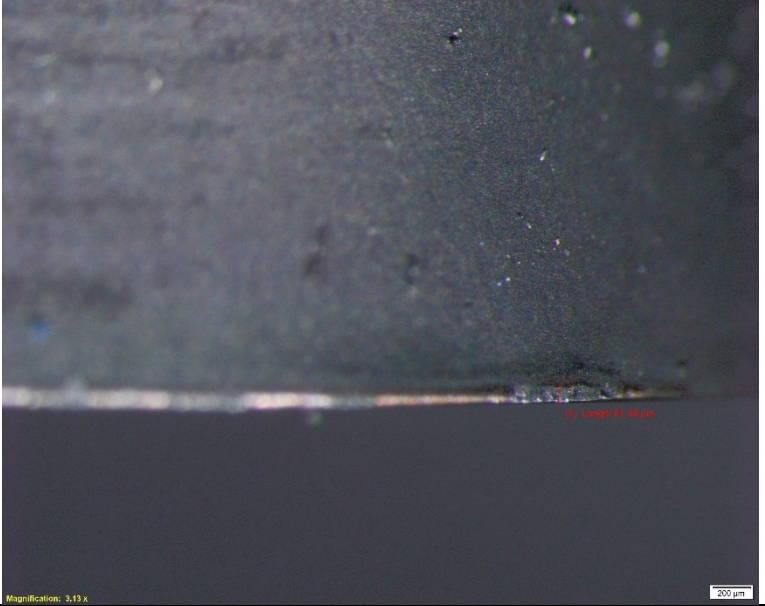
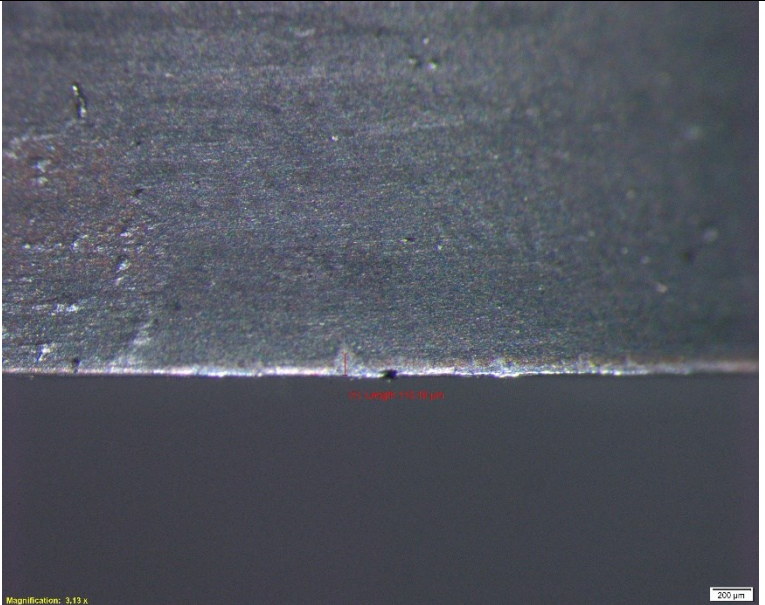
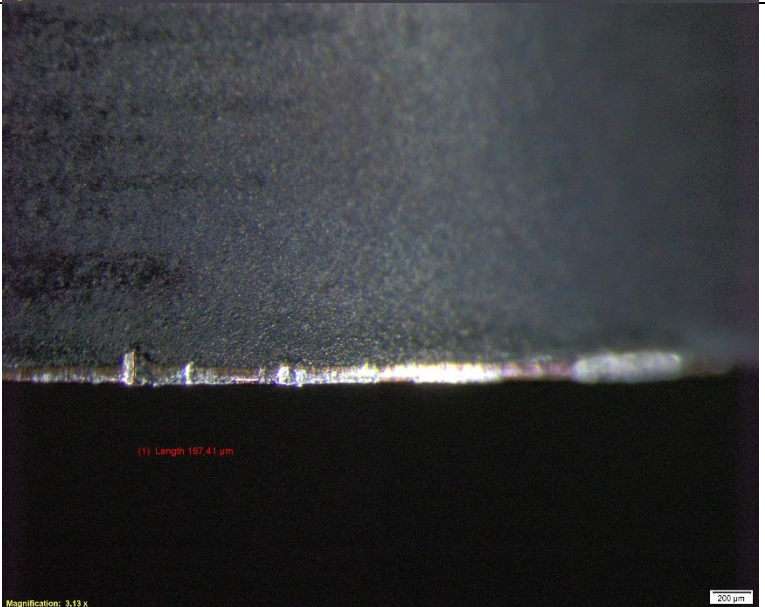
47	 <p>(1) Length 244.78 μm</p> <p>Magnification: 4 x</p> <p>200 μm</p>
50	 <p>(1) Length 250.58 μm</p> <p>Magnification: 4 x</p> <p>200 μm</p>
53	 <p>(1) Length 255.70 μm</p> <p>Magnification: 4 x</p> <p>200 μm</p>

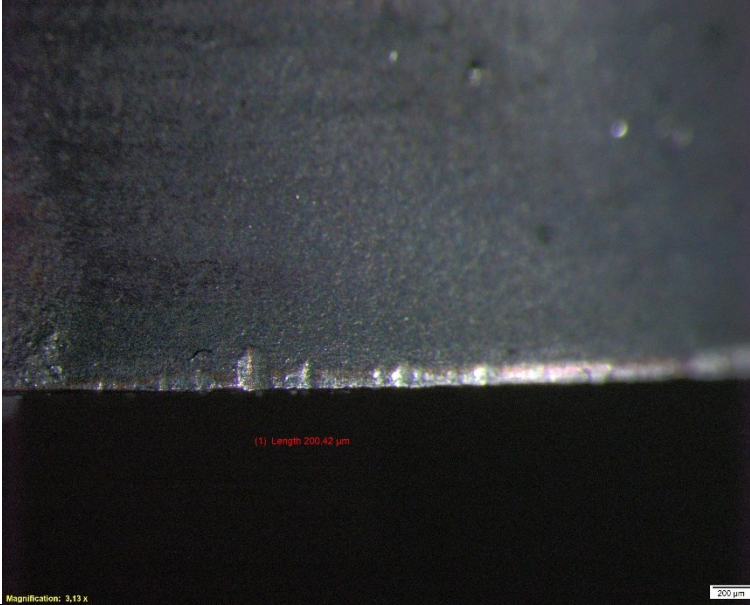
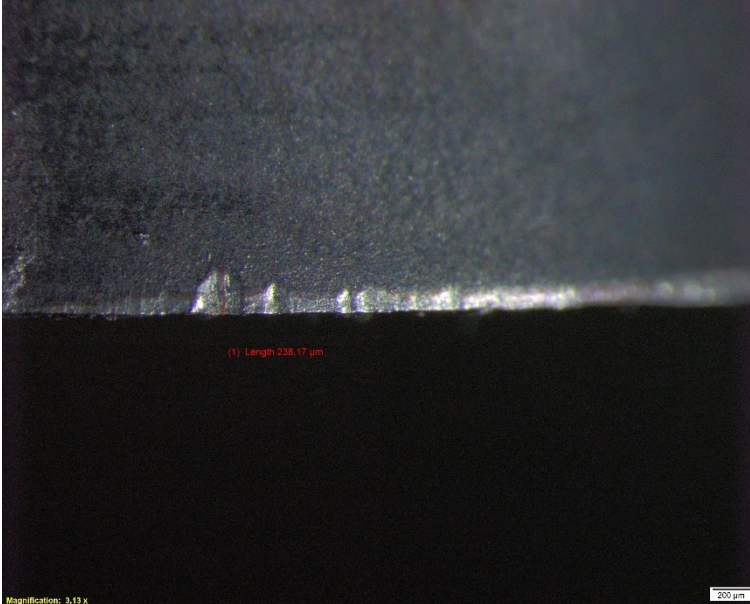
56	 <p>(1) Length 280.13 μm</p> <p>Magnification: 4x</p> <p>200 μm</p>
59	 <p>(1) Length 291.49 μm</p> <p>Magnification: 4x</p> <p>200 μm</p>

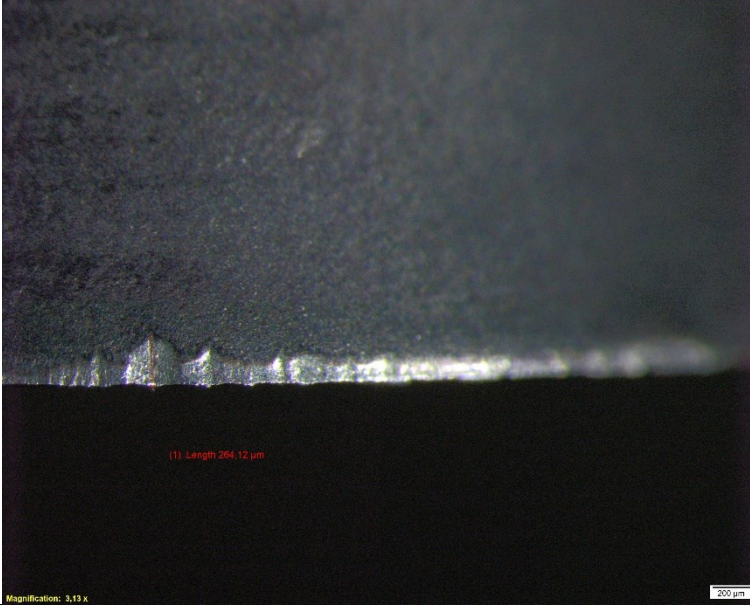
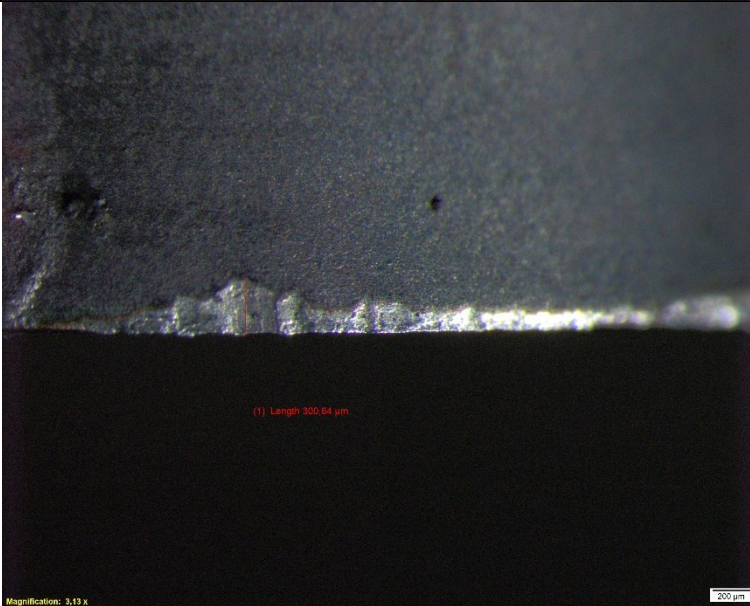
62	 <p>(1) Length 300.16 μm</p> <p>Magnification: 4x</p> <p>200 μm</p>
65	 <p>(1) Length 358.50 μm</p> <p>Magnification: 4x</p> <p>200 μm</p>

B.6 Images for Test 6

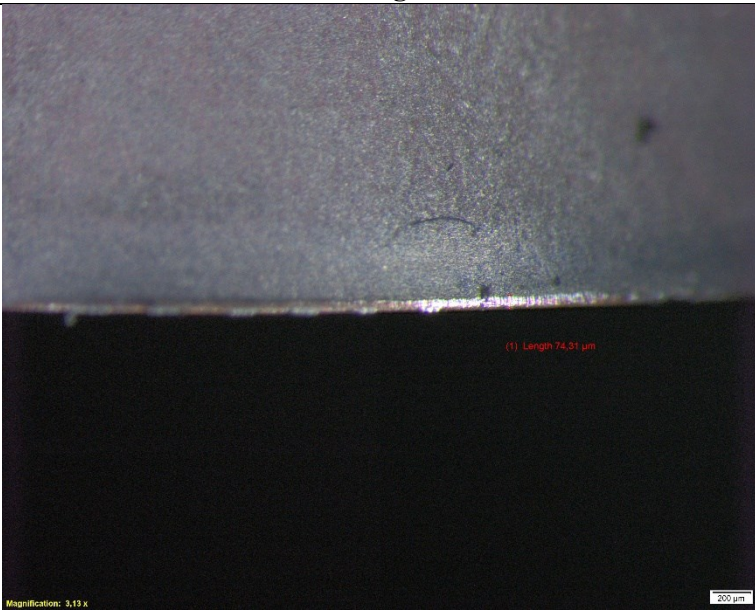
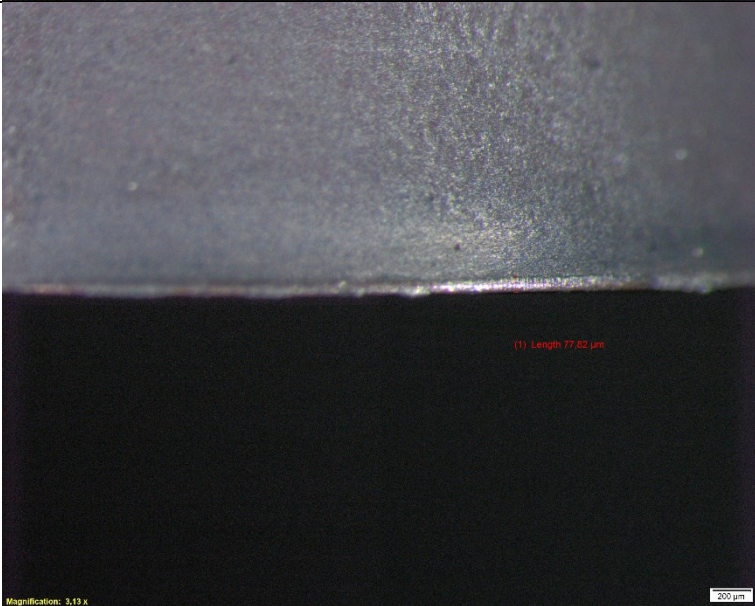
Pass #	Image
24	 <p data-bbox="480 297 1240 904">Micrograph showing a dark, textured surface with a horizontal boundary line. A red label in the center reads "(1) Length: 63.00 µm". A yellow label at the bottom left reads "Magnification: 3.13 x". A white scale bar at the bottom right indicates "200 µm".</p>
30	 <p data-bbox="480 904 1240 1507">Micrograph showing a dark, textured surface with a horizontal boundary line. A red label in the center reads "(1) Length: 63.00 µm". A yellow label at the bottom left reads "Magnification: 3.13 x". A white scale bar at the bottom right indicates "200 µm".</p>

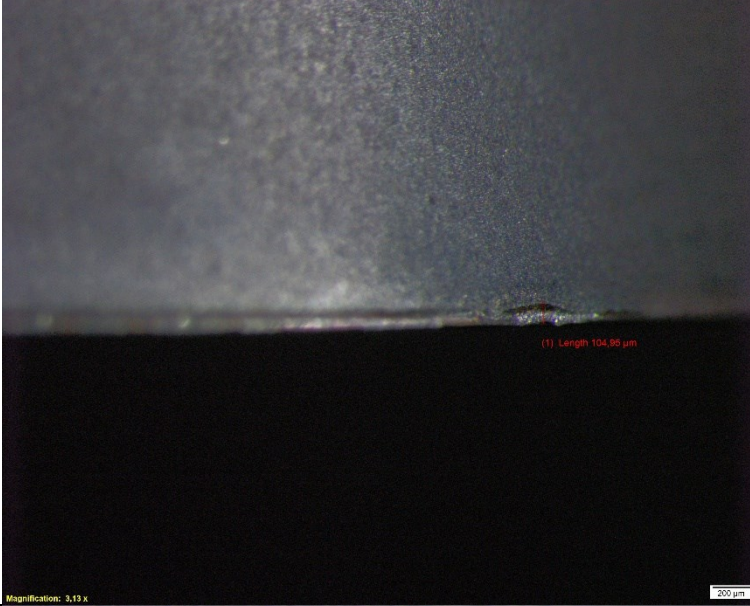
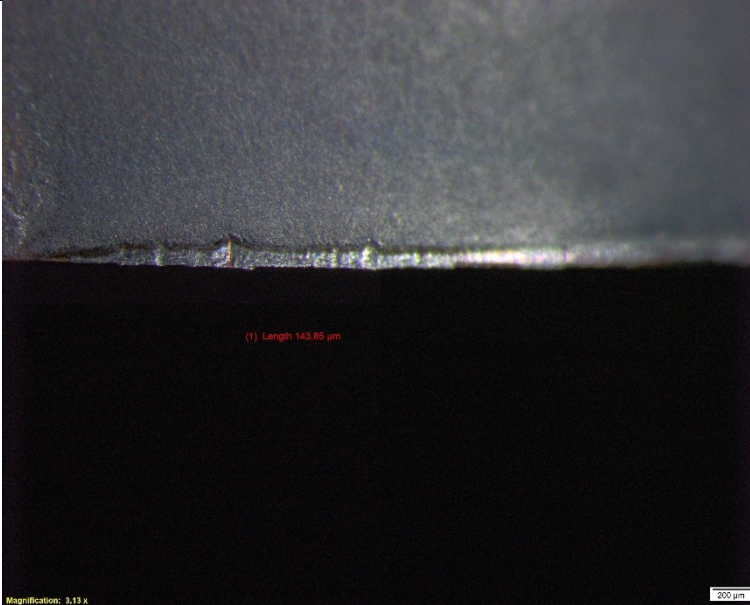
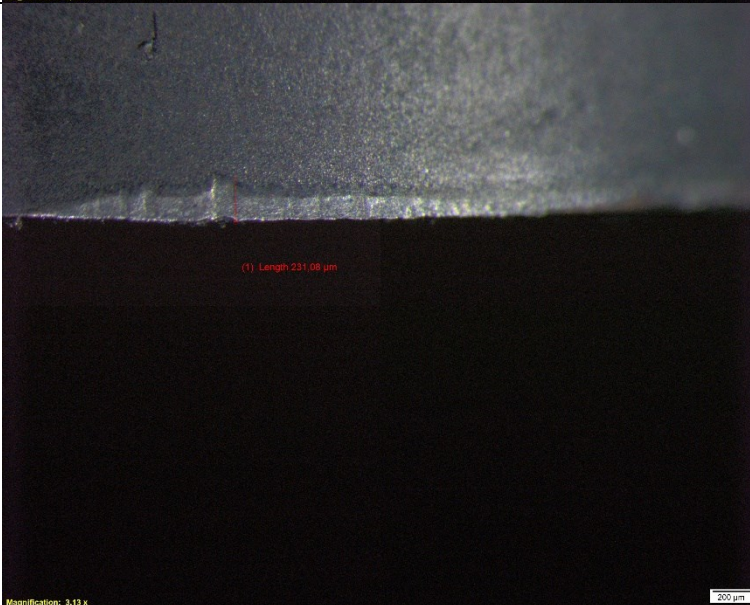
36	 <p>(1) Length 61.28 μm</p> <p>Magnification: 3.19 x</p> <p>200 μm</p>
42	 <p>(1) Length 143.16 μm</p> <p>Magnification: 3.19 x</p> <p>200 μm</p>
48	 <p>(1) Length 167.41 μm</p> <p>Magnification: 3.19 x</p> <p>200 μm</p>

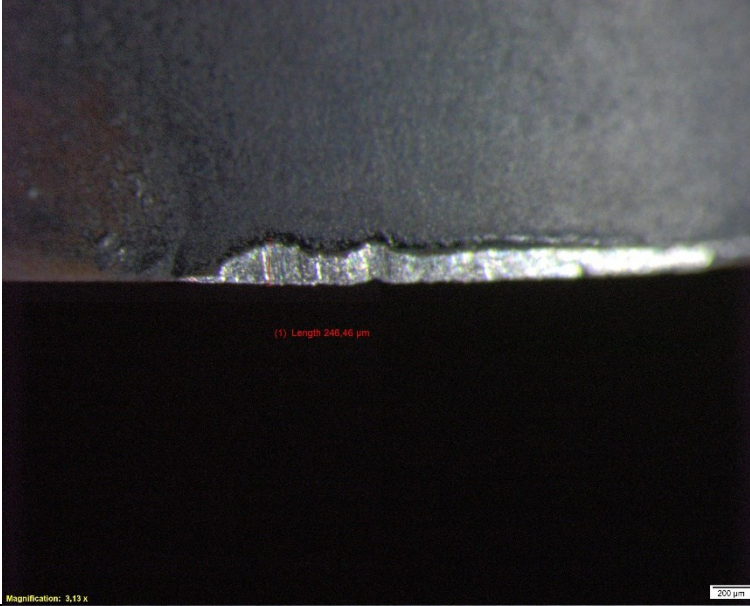
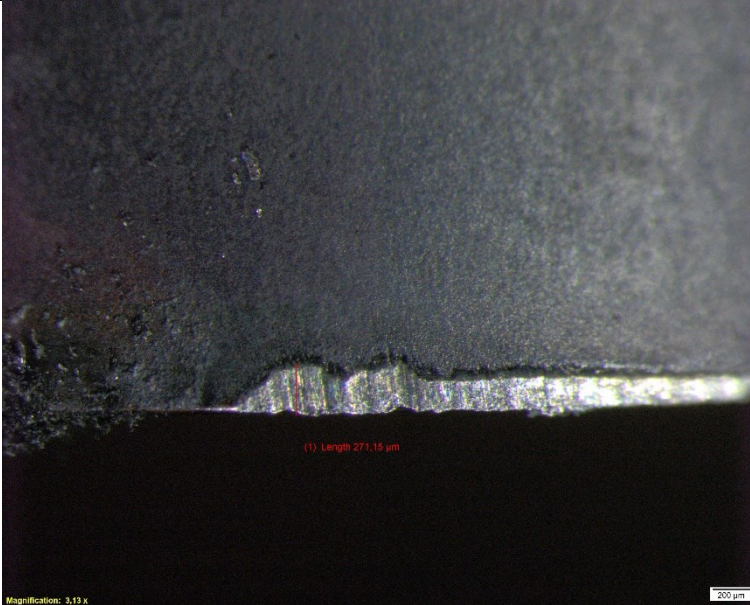
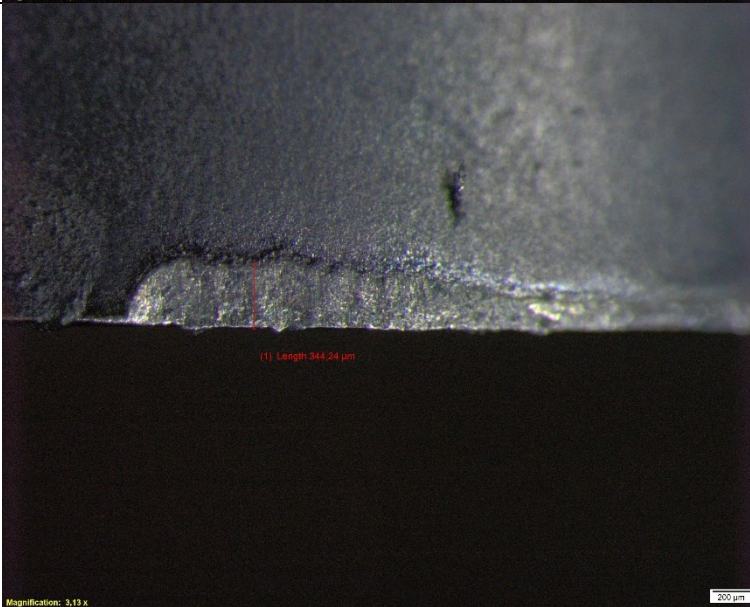
54	 <p>(1) Length 200.42 μm</p> <p>Magnification: 3.19 x</p> <p>200 μm</p>
60	<p style="text-align: center;">101</p>  <p>(1) Length 238.17 μm</p> <p>Magnification: 3.19 x</p> <p>200 μm</p>

66	 <p>(1) Length 264.12 μm</p> <p>Magnification: 3.19 x</p> <p>200 μm</p>
72	 <p>(1) Length 300.64 μm</p> <p>Magnification: 3.19 x</p> <p>200 μm</p>


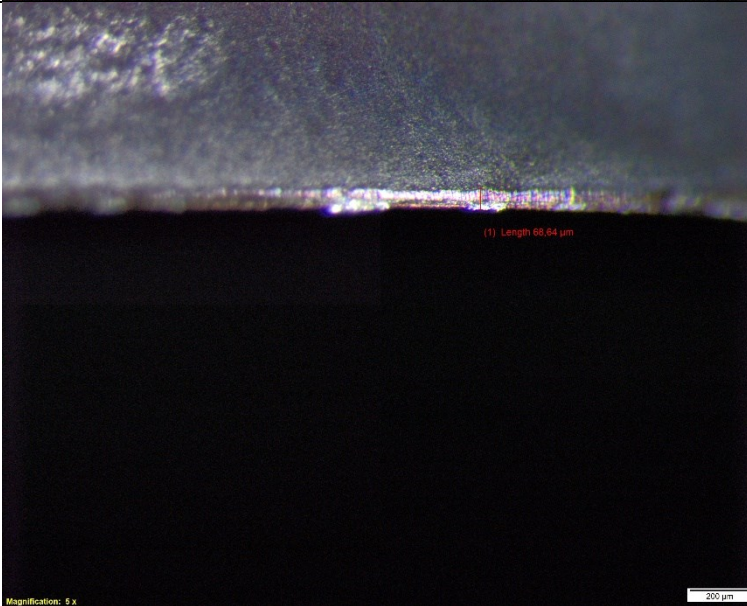
B.7 Images for Test 7

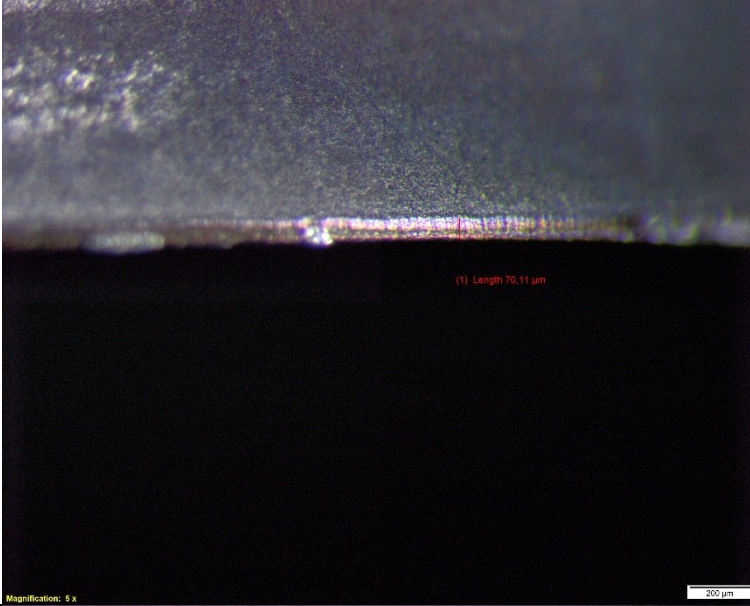
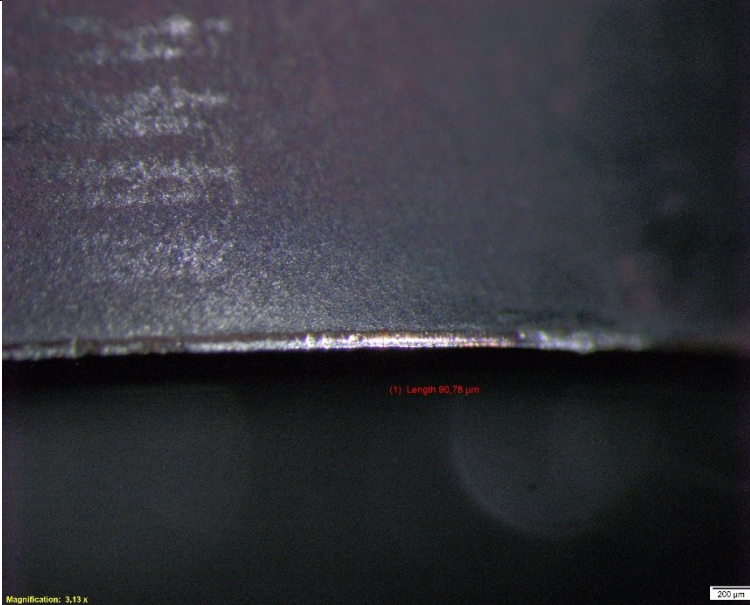
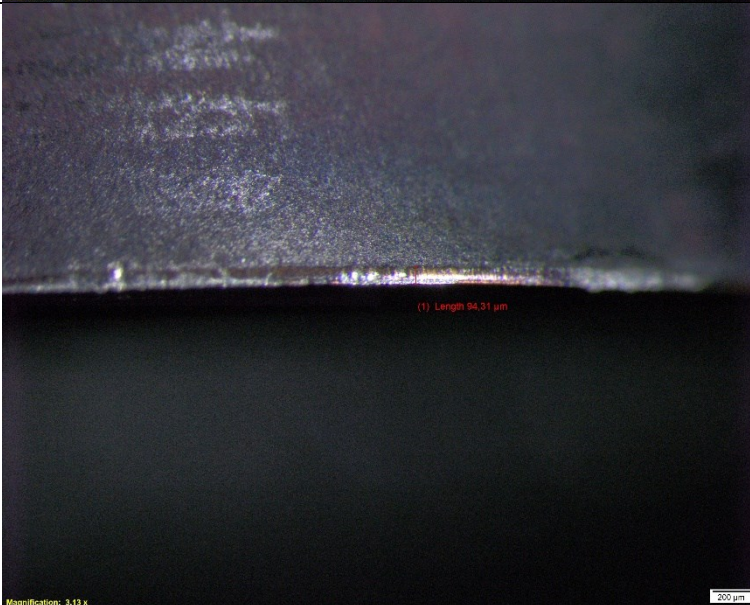
Pass #	Image
6	 <p data-bbox="986 633 1078 651">(1) Length 74.51 μm</p> <p data-bbox="480 891 568 904">Magnification: 3.13 x</p> <p data-bbox="1193 887 1238 900">200 μm</p> <p>This micrograph shows a dark, granular surface with a horizontal line of bright, multi-colored interference fringes. A red dimension line is drawn across the fringes, indicating a length of 74.51 μm. The magnification is 3.13 x, and a 200 μm scale bar is present in the bottom right corner.</p>
9	 <p data-bbox="994 1238 1082 1256">(1) Length 77.82 μm</p> <p data-bbox="480 1496 568 1509">Magnification: 3.13 x</p> <p data-bbox="1193 1491 1238 1505">200 μm</p> <p>This micrograph shows a similar dark, granular surface with a horizontal line of bright, multi-colored interference fringes. A red dimension line is drawn across the fringes, indicating a length of 77.82 μm. The magnification is 3.13 x, and a 200 μm scale bar is present in the bottom right corner.</p>

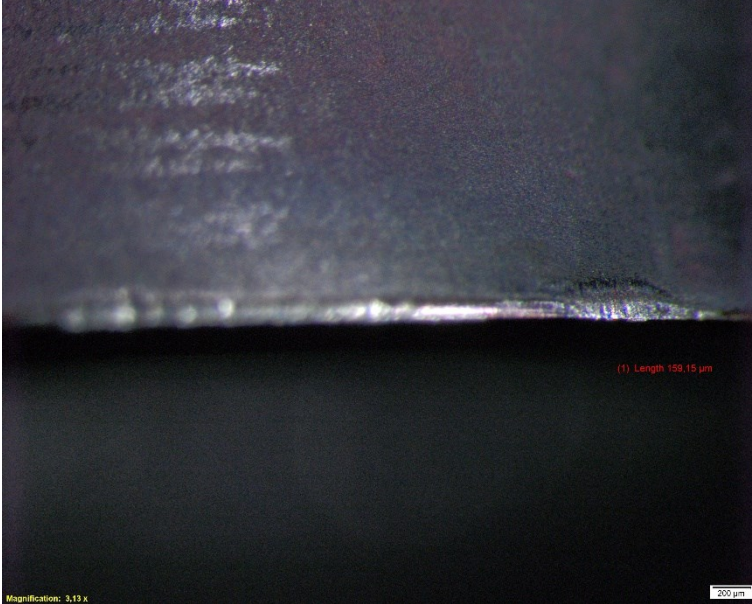
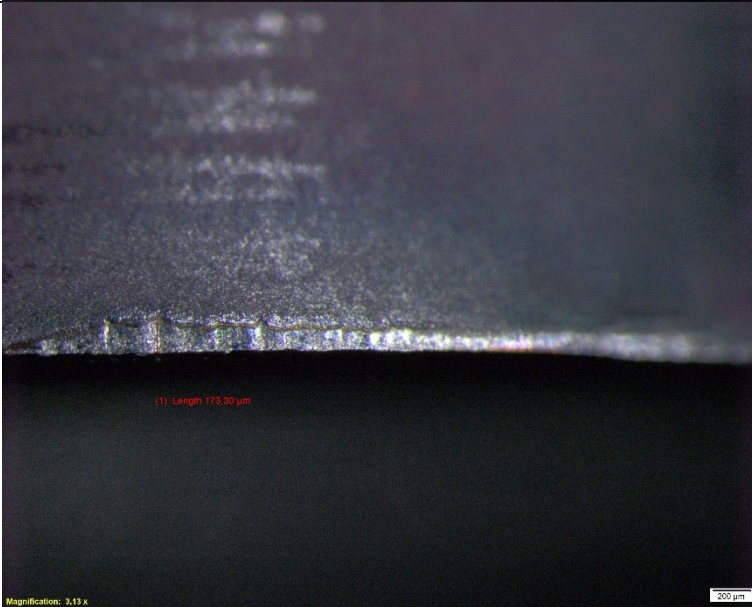
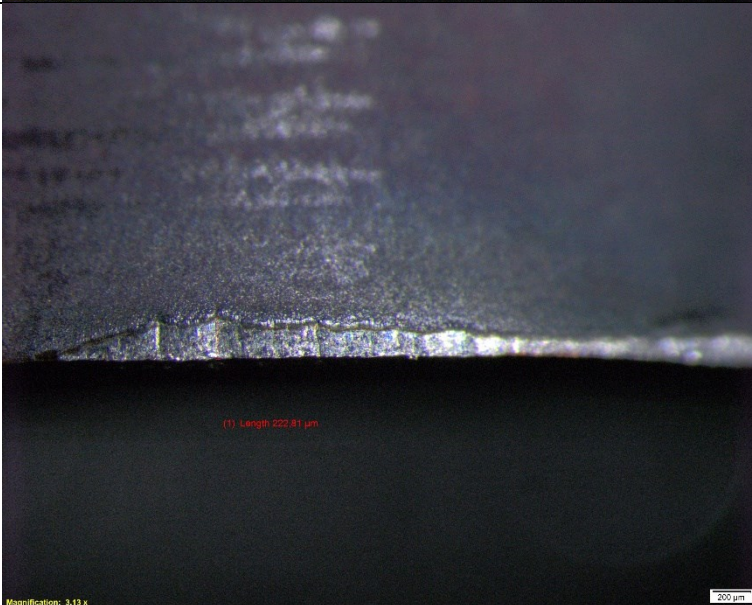
12	
18	
24	

27	 <p>(1) Length: 246.46 μm</p> <p>Magnification: 3.13 x</p> <p>200 μm</p>
30	 <p>(1) Length: 271.15 μm</p> <p>Magnification: 3.13 x</p> <p>200 μm</p>
33	 <p>(1) Length: 344.24 μm</p> <p>Magnification: 3.13 x</p> <p>200 μm</p>

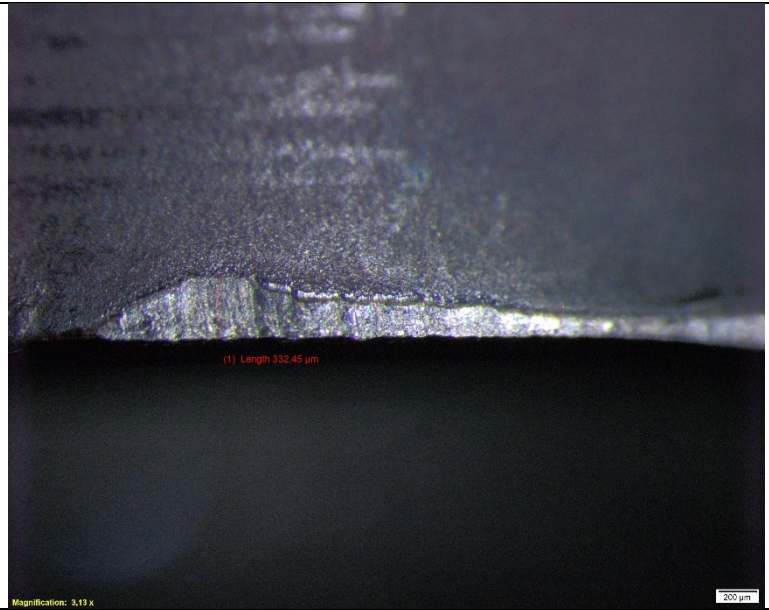
B.8 Images for Test 8

Pass #	Image
3	 <p>(1) Length 60.12 μm</p> <p>Magnification: 2.13 x</p> <p>200 μm</p> <p>This micrograph shows a surface with a dense, granular texture. A horizontal line is drawn across the middle of the image, and a red dimension line indicates a length of 60.12 μm. The magnification is 2.13 x, and a 200 μm scale bar is located in the bottom right corner.</p>
9	 <p>(1) Length 68.64 μm</p> <p>Magnification: 5 x</p> <p>200 μm</p> <p>This micrograph shows a surface with a dense, granular texture, similar to the one in Pass # 3. A horizontal line is drawn across the middle of the image, and a red dimension line indicates a length of 68.64 μm. The magnification is 5 x, and a 200 μm scale bar is located in the bottom right corner.</p>

15	
21	
27	

33	 <p>(1) Length 158.15 μm</p> <p>Magnification: 3.13 x</p> <p>200 μm</p>
39	 <p>(1) Length 173.30 μm</p> <p>Magnification: 3.13 x</p> <p>200 μm</p>
45	 <p>(1) Length 222.81 μm</p> <p>Magnification: 3.13 x</p> <p>200 μm</p>

51



Appendix C: Subset Colding Graphs

Lines represent tool lives of: $T= 5$ (black), 10 (green), 15 (blue), and 20 minutes (red) respectively.

C.1 Inner Subset

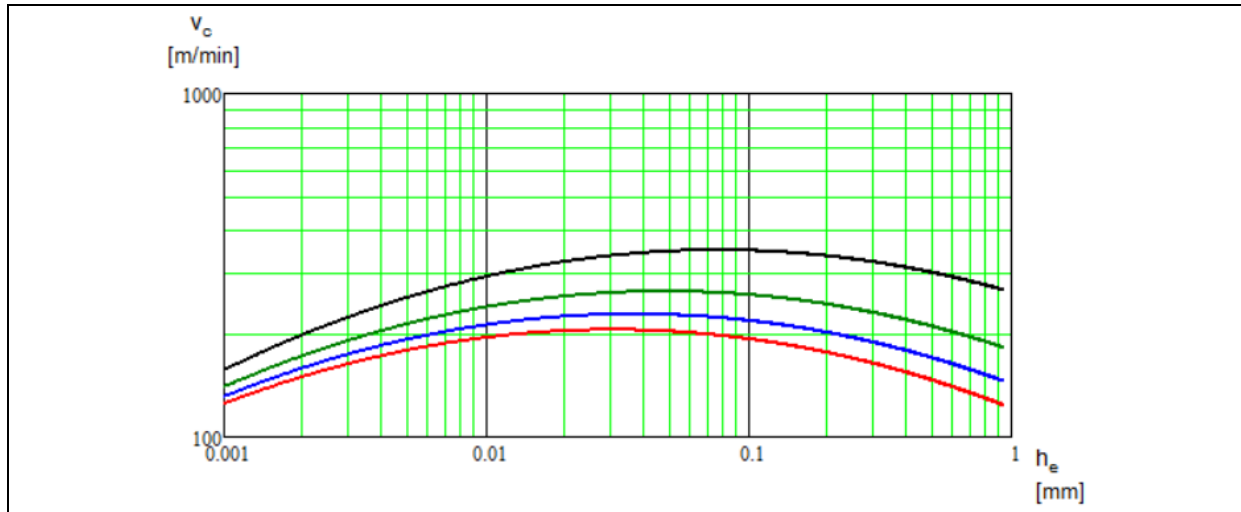


Fig 1. Colding planes for Inner Subset Test.

C.2 Outer Subset

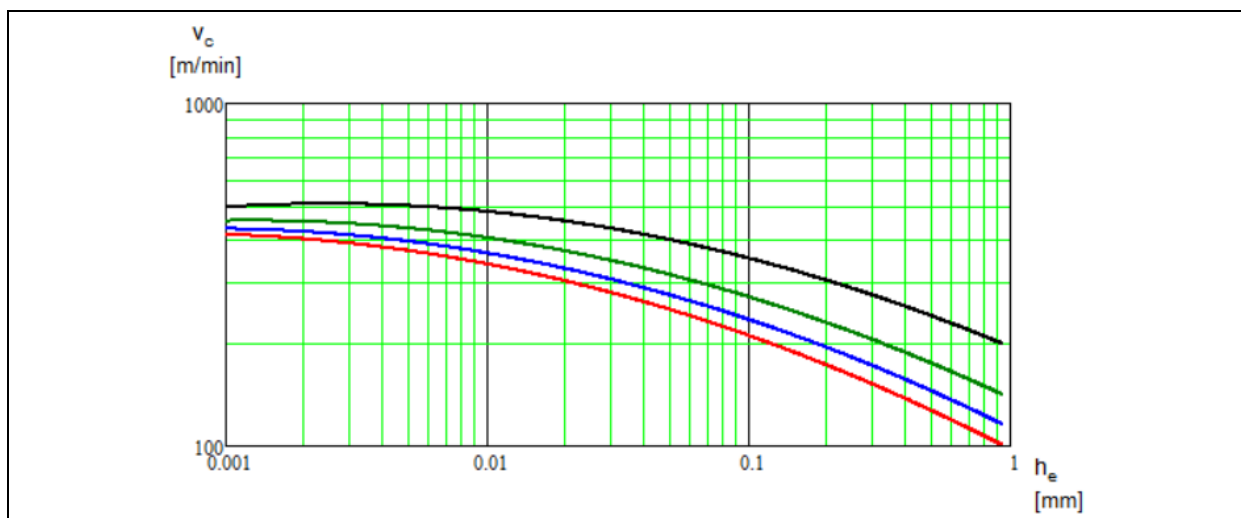


Fig 2. Colding planes for Outer Subset Test.